NONLINEAR OPTICS TECHNOLOGY
AREA I: FWM TECHNOLOGY

J. Brock, G. Holleman, F. Patterson,
J. Fukumoto, L. Frantz, M. Valley

PHASE I FINAL REPORT
June 1985 - June 1986

DTIC
ELECTE
S NOV 1 9 1986
D
A

TRW
Applied Technology Division
One Space Park
Redondo Beach, CA 90278

86 11 18 070

AD A174 112

REPORT DOCUMENTATION PAGE

1a. REPORT SECURITY CLASSIFICATION	1b. RESTRICTIVE MARKINGS
Unclassified	

2a. SECURITY CLASSIFICATION AUTHORITY	3. DISTRIBUTION/AVAILABILITY OF REPORT
	Unclassified/Unlimited
2b. DECLASSIFICATION/DOWNGRADING SCHEDULE	

4. PERFORMING ORGANIZATION REPORT NUMBER(S)	5. MONITORING ORGANIZATION REPORT NUMBER(S)

6a. NAME OF PERFORMING ORGANIZATION	6b. OFFICE SYMBOL (If applicable)	7a. NAME OF MONITORING ORGANIZATION
TRW Space and Technology Group		Office of Naval Research

6c. ADDRESS (City, State and ZIP Code)	7b. ADDRESS (City, State and ZIP Code)
One Space Park Redondo Beach, CA 90278	Arlington, VA 22217-5000

8a. NAME OF FUNDING/SPONSORING ORGANIZATION	8b. OFFICE SYMBOL (If applicable)	9. PROCUREMENT INSTRUMENT IDENTIFICATION NUMBER
DARPA		N00014-85-C-0257

8c. ADDRESS (City, State and ZIP Code)	10. SOURCE OF FUNDING NOS.			
Arlington, VA 2209-2308	PROGRAM ELEMENT NO.	PROJECT NO.	TASK NO.	WORK UNIT NO.

11. TITLE (Include Security Classification)
Nonlinear Optics Technology, Area I: FWM Technology

12. PERSONAL AUTHOR(S)
J. Brock, G. Holleman, F. Patterson, J. Fukumoto, L. Frantz, M. Valley

13a. TYPE OF REPORT	13b. TIME COVERED	14. DATE OF REPORT (Yr., Mo., Day)	15. PAGE COUNT
Phase I Final	FROM June '85 TO June '86	1986 September 22	143

16. SUPPLEMENTARY NOTATION

17.	COSATI CODES		18. SUBJECT TERMS (Continue on reverse if necessary and identify by block number)
FIELD	GROUP	SUB. GR.	Four-wave Mixing, Na Vapor, Phase Conjugation, Reflectivity
			Imaging Fidelity, Noise Crosstalk
			≥ or =

19. ABSTRACT (Continue on reverse if necessary and identify by block number)

Four wave mixing (FWM) performance in Na vapor was evaluated in the strong pumping regime ($I \gg I_{sat}$) required for typical applications related to point-to-point optical links. Gain (= reflectivity), imaging fidelity, and noise crosstalk were measured and analyzed under several conditions to obtain an engineering data base for potential tactical applications such as communications, surveillance, and guidance systems.

Results include ≥230% reflectivity and 15 lines pair/mm imaging resolution, both the highest reported to date with cw pumping in low density Na vapor. The observed resolution was limited by the pixel spacing of our video camera. Ten 1p/mm resolution was obtained after passing the input image through a 65 λ aberrator. Noise crosstalk was observable only when the combined signal/noise powers were large enough to saturate the phase conjugate return signal via pump depletion. Under these conditions, a degenerate, coherent noise beam 3x stronger than the signal beam produced only a 21% reduction in the intensity of the phase conjugate signal, and this degree of crosstalk decreased rapidly as the pump/noise angle increased.

20. DISTRIBUTION/AVAILABILITY OF ABSTRACT	21. ABSTRACT SECURITY CLASSIFICATION
UNCLASSIFIED/UNLIMITED ☒ SAME AS RPT. ☐ DTIC USERS ☐	Unclassified

22a. NAME OF RESPONSIBLE INDIVIDUAL	22b. TELEPHONE NUMBER (Include Area Code)	22c. OFFICE SYMBOL
R. E. Behringer	818.795.5971	ONR - Pasadena

lambda

DD FORM 1473, 83 APR EDITION OF 1 JAN 73 IS OBSOLETE.

i

The experiments were performed with pump and probe beams that were derived from a single, 800 mW, CW ring dye laser (Coherent 699-21) operating narrowband (1MHz) or broadband (2GHz) near the 589 nm D_2 resonance line in Na. Pump intensities ranged from 60-130 w/cm^2; focused beam diameters of 0.2-1mm $1/e^2$ produced intensities of 10^3-10^4 I_{sat} which power broadened the Na linewidths to 30-100x of their collision-free width of 62.5 MHz. An on-line Lamb Dip diagnostic monitored laser frequency relative to the resonance line with 50 MHz accuracy. Vapor densities in the 10^{12}-10^{13}/cm^3 range were tested in quartz and pyrex cells with pathlengths varying from 1 mm to 10 cm. Highest reflectivity was obtained with no buffer gas; He buffer pressures up to 50 torr were used.

Existing FWM models for homogeneously broadened systems were adapted to the high-intensity, high reflectivity regime. 1-D analytical and numerical models were implemented to survey FWM situations involving nonresonant and resonant nonlinearities, and a 2-D numerical model was prepared to address wave optic considerations such as conjugation fidelity. A physical picture was developed to interpret experimental results and provide the basis for future development of a quantitative model for strongly pumped, inhomogeneously broadened media. Intensity crosstalk due to a combination of nonlinearity saturation and pump depletion can be predicted quantitatively for arbitrary noise/probe beam intensity ratios.

PREFACE

This Final Report describes the Area I: Four-wave Mixing Technology effort funded by DARPA Order 5369, Amendment #1, and monitored under Office of Naval Research Contract No. N00014-85-C-0257. The work was performed by the TRW Space and Technology Group, Redondo Beach, CA 90278; G. Holleman was the program manager. J. Brock served as the Area I technical manager with the support of J. Fukumoto, M. Valley, and D. Bowler who managed experimental and analytical work units. Other personnel who made vital contributions to the technical success of this program were L. Frantz, F. Patterson, M. Caponi, and P. Fairchild. The laboratory assistance of W. Carrion, F. Alvarez, and A. Edmon was also essential; C.C. Shih and G. Hughes provided important modeling support. The technical and managerial guidance of L. Marabella is also gratefully acknowledged along with the fine secretarial support obtained from J.C. Miller and P. Bessenbacher. Project administration functioned smoothly through the efforts of L. Meisenholder, Contracts, and L. Garman and P. Weber, Project Control.

The work performed on this contract was administered by S. Shey of the DARPA Directed Energy Office, and R.E. Behringer, Office of Naval Research. Their support and assistance contributed greatly to the program success.

Accession For

NTIS GRA&I ☑
DTIC TAB ☐
Unannounced ☐
Justification____

By____
Distribution/
Availability Codes

Dist	Avail and/or Special
A1	

TABLE OF CONTENTS

TABLE OF CONTENTS (Continued)

LIST OF FIGURES

viii

1.0 EXECUTIVE SUMMARY

Four wave mixing (FWM) performance in Na vapor was evaluated in the strong pumping regime ($I \gg I_{sat}$) required for typical applications related to point-to-point optical links. Gain (= reflectivity), imaging fidelity, and noise crosstalk were measured and analyzed under several conditions to obtain an engineering data base for potential tactical applications such as communications, surveillance, and guidance systems.

Results include $\geq 230\%$ reflectivity and 15 line pair/mm imaging resolution, both the highest reported to date with cw pumping in low density Na vapor. The observed resolution was limited by the pixel spacing of our video camera. Ten lp/mm resolution was obtained after passing the input image through a 65 λ aberrator. Noise crosstalk was observable only when the combined signal/noise powers were large enough to saturate the phase conjugate return signal via pump depletion. Under these conditions, a degenerate, coherent noise beam 3x stronger than the signal beam produced only a 21% reduction in the intensity of the phase conjugate signal, and this degree of crosstalk decreased rapidly as the pump/noise angle increased.

The experiments were performed with pump and probe beams that were derived from a single, 800 mW, CW ring dye laser (Coherent 699-21) operating narrowband (~1 MHz) or broadband (2GHz) near the 589 nm D_2 resonance line in Na. Pump intensities ranged from 60-130 w/cm^2; focused beam diameters of 0.2-1 mm 1/e^2 produced intensities of 10^3-10^4 I_{sat} which power broadened the Na linewidths to 30-100x of their collision-free width of 62.5 MHz. An on-line Lamb Dip diagnostic monitored laser frequency relative to the resonance line with 50 MHz accuracy. Vapor densities in the 10^{12}-10^{13}/cm^3 range were tested in quartz and pyrex cells with pathlengths varying from 1 mm to 10 cm. Highest reflectivity was obtained with no buffer gas; He buffer pressures up to 50 torr were used.

The reflectivity of DFWM in Na vapor was measured versus frequency offset from resonance, pump intensity, pump/probe angle, and pump bandwidth. With a 300 mW, 1 MHz pump two reflectivity peaks were observed on the Na D_2 line, one on the low frequency side of the 2-3 hyperfine transition and one on the high frequency side of 1-0 transition. Their

1

FWHMs were ~2.2 GHz and 1.4 GHz respectively; the 2-3 reflectivity peak was about 20% of the 1-0 maximum. Little or no reflectivity was observed on the other four hyperfine transitions of the D_2 line because optical pumping depletes the ground state populations of these lines. The strong linear absorption of the medium ($\alpha_o L \approx 200$) eliminated a conjugate return in a 2.5 GHz frequency range that overlaps the line centers of the 2-3 and 1-0 lines which are separated by 1.7 GHz. An increase of pump power from 300 to 450 mW increased the 2-3 and 1-0 reflectivity maxima by 20% and 12% respectively, the corresponding bandwidths went up by 18% and 50% respectively, and the gap between the two peaks narrowed to 1.2 GHz. The latter result is due to increased saturation of the linear absorption in that region. A maximum reflectivity of 230% was obtained on the 1-0 hyperfine transition with the peak occurring 0.9 GHz on the high frequency side of the transition line center.

Self action effects were observed as increases in the divergences of both the transmitted pump beams and the phase conjugate return. Self focusing, which occurs on the high frequency side of a transition, increases the effective pump intensity on the 1-0 line and is the reason the reflectivity there is higher than on the 2-3 line. The low frequency side of the 2-3 line is subject to self defocusing, which reduces the effective pump intensity there. As expected, the 2-3 line, which has a larger oscillator strength and degeneracy factor, exhibits the higher reflectivity at lower pump intensities where self action effects are negligible.

The reflectivity FWHM versus pump/probe angle was measured to be ~2.2 mrad with $1/\sin^2 \theta$ dependence for angles greater than 13 mrad. This dependence, which is predicted for a homogeneously broadened system, is also shown to be expected for angles $\leq \Delta\omega_{pb}/\Delta\omega_D$, the ratio of the power-broadened homogeneous width to the inhomogeneous width (≈ 0.2 at our test conditions). With 2 GHz bandwidth pumps, reflectivities as high as 20% were measured and the FWHM vs pump/probe angle doubled to ~ 4.5 mrad. Simultaneous degenerate and nondegenerate FWM interactions are believed to contribute to the broadband response.

An active tracking demonstration showed automatic tracking over a 50 mrad field of view at angular scan rates in excess of 100 rad/s. Residual tracking error was less than our detection limit of 1 μrad.

Noise mechanisms intrinsic to the FWM process were studied by introducing a second probe (noise) beam into the phase conjugation region. Intensity crosstalk, which occurs when the presence of a noise beam changes the phase conjugate reflectivity of the signal beam, was observed and characterized. Saturation of the nonlinearity and/or pump depletion produce intensity crosstalk when high probe intensities are used ($I_{probe} \geq 0.1\ I_{pump}$). A maximum 21% reduction in the phase conjugate signal was observed at a noise/signal intensity ratio of 3:1 and noise/signal angular separation of 13 mrad. Variation of signal, noise, and pump polarizations had no affect on the degree of crosstalk. Reflected phase conjugate power saturates as the probe/pump intensity ratio is increased from 0.02 to 0.3; this saturation curve can be used to predict intensity crosstalk levels. Our analysis indicates there is no mechanism for phase crosstalk between a signal and noise beam, and none was oberved.

Spatial crosstalk is defined as the transfer of transverse intensity patterns from a noise beam to the phase conjugate signal wave. This was studied by imprinting a 2.8 line pair/mm, three bar image from an Air Force resolution target onto a 6 mW noise beam, and looking for that image pattern in the phase conjugate return of a 1 mW signal; none was observed. Intensity crosstalk reduced the contrast in the phase conjugate signal image, a three bar image orthogonal to that in the noise beam, by 46%, but there was no reduction in the sharpness of the edges and there was no evidence of an orthogonal pattern overlaid onto the original signal. The noise and signal inputs were focused into the Na cell so the intensity patterns in the conjugation region were the Fourier transforms of the orthogonal bar images. Only the central lobes of the signal and noise inputs, which contain the low spatial frequency components of the original images, were coincident. Thus the crosstalk led to contrast reduction with no loss of edge definition. Our image fidelity for these experiments was limited by the pixel resolution of our video camera to about 15 lp/mm; pump beam $1/e^2$ diameters were about 1100 μm. These measurements were made at pump intensities where self action effects were negligible and phase conjugate reflectivities were 10-25%.

The operating region of interest for field applications involves strong pumping to obtain high reflectivity of weak signals. In general the theory in this regime is not amenable to available analytical or

3

numerical treatments. Therefore an analytical framework for understanding FWM in a strongly pumped, Doppler-broadened, saturable absorber was established. This was supplemented with development of simple models for homogeneously broadened, nonresonant and resonant systems that can later be upgraded to incorporate inhomogeneous broadening and wave optics considerations. For high reflectivity cases where there is strong linear absorption and strong optical saturation we show that the laser frequency for maximum nonlinearity is shifted off resonance by an amount dependent on optical intensity and on the ratio of signal and pump beam intensities.

The frequency offset for maximum FWM reflectivity in a strongly pumped saturable absorber is explained as follows. The intensity contrast in the alternating spatial regions where the input pump and signal waves interfere produces spatial variations in the nonlinear susceptibility χ of the medium. Fringe contrast is high when beams of equal intensity interfere, but the dark regions remain strongly illuminated when beams of unequal intensity interfere. In a strongly saturated system with equal intensity beams, high fringe contrast produces large spatial variations in χ that are maximized near resonance. When weak signal beams are combined with a strong pump intensity that is $> I_{sat}$, fringe contrast is low and both the light and dark regions remain strongly saturated near resonance with a result that χ variations are also small. Then maximum nonlinearity is obtained by moving off resonance to a frequency where the effective $I/I_{sat} \approx 1$, because this is the regime where χ is most sensitive to small changes in illumination intensity.

Doppler broadened media can be understood by estimating the effects of experimental parameters on the population of the velocity group in which the interference grating is written. Key parameters are frequency offset, relative pump and signal angles, and optical intensities. A procedure for identifying the velocity group that is simultaneously resonant with the input optical waves has been outlined.

The optical field interacts resonantly only with absorbers that have velocity components that shift their (stationary) resonance frequency to that of the optical field. In the standard, degenerate FWM geometry with weak, counterpropagating pumps; maximum reflectivity occurs on resonance and only the v=0 velocity group can contribute to the nonlinearity. When strong pumping is used, the fringe contrast considerations mentioned above move the maximum nonlinearity to a nonresonant frequency. Now the various

4

input waves, which typically enter at different angles, optimally interact with velocity groups moving in different directions. One result is that maximum reflectivity can occur with nondegenerate rather than degenerate FWM in this case if the frequency of one of the counterpropagating pumps is shifted by an amount equal to $-\Delta\omega$ when the frequencies of the other pump and the signal are $+\Delta\omega$ from resonance.

In general, FWM performance tends to optimize when frequency offsets and angles are set so that the velocity group involved is near the thermal velocity. The situation becomes very complex, however, when the details of Na hyperfine spectroscopy, hyperfine optical pumping, power broadening, and fringe contrast considerations are included.

The Na hyperfine transitions are closely spaced relative to the Doppler line width, so each transition can be interacting resonantly through separate velocity groups. Under low intensity illumination the hyperfine separations are greater than the homogeneous linewidths, but in our strong pumping regime the homogeneous widths become greater than the hyperfine spacings. The increased homogeneous bandwidth increases the rate at which thermal washout of the interference grating occurs, because it permits interaction with more velocity groups that are moving perpendicular to the grating lines. In the pure Doppler limit only velocities parallel to the interference grating lines are permitted. Finally thermal diffusion conteracts the optical pumping that occurs in 4 out of 6 of the Na D_2 hyperfine transitions. The preceding phenomena have variable, opposing impacts on the net nonlinearity observed. Our physical picture, which provides an outline for qualitatively understanding these effects, can serve as the basis for further development of a comprehensive model.

The contract SOW called for experimental measurements that address technical issues relating to phase conjugated optical links. No analysis beyond that required to empirically relate results to possible application scenarios was specified. The required reflectivity, crosstalk, and fidelity experiments that were performed are presented in this report. During the program it was determined that analysis of FWM physics beyond that required by the contract was desireable. In particular, noise crosstalk mechanisms were investigated on TRW IR&D, and this theoretical description is included in Section 5 because it substantiates our conclusion that crosstalk will not seriously impact FWM applications.

5

2.0 INTRODUCTION

This final report describes results obtained during the first phase
of the Nonlinear Optics Technology program, a one year effort to invest-
igate phase conjugation by four wave mixing (FWM) for enhancing perform-
ance of electro-optical systems in tactical applications. There were two
primary tasks:

1. An experimental investigation of the characteristics of FWM in
   the high reflectivity regime required by many field applica-
   tions. Sodium vapor was chosen as the FWM medium. Studied were
   the spectral response of reflectivity for strong CW pumping
   conditions, field of view, noise crosstalk, image fidelity, and
   the impact of finite pump laser bandwidth.

2. An analytical modeling task to develop the understanding
   necessary for projecting potential mission performance based on
   laboratory measurements. Numerical one dimensional and two
   dimensional models, as well as a qualitative physical model,
   were developed to explain the observed behavior.

In addition to these tasks, some effort was directed to identifying
potential tactical missions that could benefit from the application of
phase-conjugation FWM technology. Mission factors that could be
substantially impacted by FWM were identified. These include optics
jitter, image quality, optical link tracking, laser power requirements,
and others. Several potential mission applications were identified, and
one of the most promising, tactical optical communications links, was
briefly evaluated.

This section of the report summarizes the overall program objectives
and guiding considerations and introduces the subject of nonlinear phase
conjugation via FWM interactions. Section 3 presents a general discussion
of FWM in sodium vapor, and the remaining sections describe specific
measurements and analyses that were performed.

2.1 PROGRAM APPROACH/GOALS

FWM in sodium vapor has been the subject of many investigations over
the last ten years. While quite elegant, most of this work has

concentrated on the basic spectroscopy of the FWM process and its development as a nonlinear tool under experimental conditions tractable for theoretical description. The focus of the work reported here has been to investigate FWM parameters that are critical for effective mission performance, under experimental conditions that are optimized for best mission-oriented performance rather than analytical convenience. Parameters that were studied included spectral response, field of view, crosstalk between different input beams to a FWM, and conjugation fidelity. An effort was made to acquire data on these parameters in the experimental regime of high FWM phase conjugate reflectivity, this regime being a particularly important one for practical implementation of this technology. It was a program goal to understand better the dependence of these mission-oriented performance characteristics on experimental conditions in the high reflectivity regime.

2.2 PRACTICAL CONSIDERATIONS/REQUIREMENTS

High reflectivity is usually achieved using intense peak pump powers available from pulsed laser sources. However, use of very short pulse pumps is not a pragmatic approach when viewed in light of many mission applications involving detection and conjugation of a return reflection from a remote target. Use of short pulse pumps requires a very accurate knowledge of range to target if the pump pulses are to coincide in time with the return pulse in the FWM. For this reason, practical application of FWM technology for remote sounding applications requires a FWM medium that can provide high conjugate reflectivity at the low to moderate pump powers available from long-pulse or CW pump sources. Such materials are also necessary to reduce the size and weight of phase conjugating electro-optical systems. Sodium vapor was employed as the FWM medium in our experiments because it has a strong nonlinearity that can lead to high reflectivity for modest pump intensities in the visible. This made it possible to perform the experiments with relatively low intensities available from CW narrowband dye laser sources.

2.3 OPTICAL PHASE CONJUGATION BY FWM

A number of different nonlinear optical techniques have been developed for optical phase conjugation, the process in which an optical

7

wave has its propagation direction and relative phase reversed so that it exactly retraces its path. Four wave mixing is one approach particularly well-suited for missions where the return or input signal is weak because the process has no threshold. Reference 2-1 provides an extensive review of phase conjugation, including discussions of the FWM process.

2.3.1 General Principles of FWM

Phase conjugation by FWM is typically performed in the backward, or counterpropagating pump geometry shown in Figure 2-1. Three input waves incident on a material with a nonlinear response are mixed to form a fourth wave that is radiated from the medium with a frequency and direction determined by the frequencies and propagation directions of the three input waves. The nonlinear polarization that gives rise to this fourth wave is

$$P_{NL}^{(3)} = \chi^{(3)} E_T^3 \qquad \qquad 2\text{-}1$$

where E_T is the total electric field present in the nonlinear medium and $\chi^{(3)}$ is the third-order nonlinear susceptibility of the medium. Given input waves of the form

$$E_i = 1/2 \ E_i \ \exp[i(\omega_i t - k_i z)] + \text{complex conjugate} \qquad 2\text{-}2$$

there are many terms in the third-order nonlinear polarization, several of which have the form

$$P_{NL}^{(3)} = 1/2 \ \chi^{(3)} E_1 E_2 E_s^* \ \exp\{i[(\omega_1 + \omega_2 - \omega_s)t - (k_1 + k_2 - k_s) \cdot r]\} + c.c \qquad (2\text{-}3)$$

If E_1 and E_2 are phase conjugates of one another, as they are for the two counterpropagating plane wave pumps in Figure 2-1, then this polarization gives rise to a field propagating in the $-k_s$ direction that is the phase conjugate of the input field defined by Equation 2-2. The interaction can be degenerate, i.e. all fields have the same frequency ω, or nondegenerate, with the frequency of the fourth field being the sum of the two pump fields minus the input signal field as shown in the first term of the exponential in Equation 2-3. The dominant four wave mixing process out of all of the terms in the third-order nonlinear

8

Figure 2-1. Counterpropagating pump ($E_f E_b$) geometry for phase conjugating an input probe beam (E_p) using FWM.

polarization is determined by the wavevector of the generated wave defined by the second factor in the exponential. This wavevector of the generated fourth wave needs to meet the phase-matching condition that $k_4 = n\omega_4/c$ for efficient transfer of energy from the pump fields to the input signal wave and its conjugate.

2.3.2 Data Requirements

The technical data base on the performance of FWM phase conjugators under conditions pertinent to field applications was inadequate for even simple systems engineering projections. High power, high reflectivity data exists for nanosecond pulse lengths, and low power spectroscopic data is available, but little is known about long pulse or CW behavior of media with large nonlinear susceptibilities in the high reflectivity regime. This program collected data needed for further engineering of FWM phase-conjugated electro-optical systems.

2.4 REFERENCES

2-1 R. A. Fisher (ed), Optical Phase Conjugation, Academic Press, New York, 1983.

9

3.0 FWM IN SODIUM VAPOR

To establish an analytical framework for interpreting the experimental results of Sections 4, 5, and 6, this section presents a discussion of the physics of four-wave interactions in sodium vapor. Instead of a purely theoretical treatment with limited applicability to the strong saturation regime of our experiments, Section 3.1 concentrates on developing a physical model of the important processes occuring in Doppler-broadened media when exposed to a combination of weak and strong optical fields. Section 3.2 extends this discussion to the specific case of the sodium D_2 line. Section 3.3 outlines the approach taken for analyzing experimental results in light of the saturation regime in which the data was obtained.

3.1 GENERAL DESCRIPTION

Nonlinear optical interactions in inhomogeneously-broadened saturable absorbers are complex experiments involving only selected subgroups of the total available absorber number density and a variety of frequency dependent saturation effects. Current analytical solutions are valid only in the limit of low optical intensity. In this section, we develop a model for understanding FWM interactions in a strongly pumped, Doppler-broadened saturable absorber. For the case of high FWM reflectivity, where there is strong linear absorption and strong optical saturation, we show that the expected results are substantially different than those predicted by analytical models in either the homogeneous or low-power Doppler limits. In this general discussion, it is shown that:

1. the maximum nonlinearity is shifted away from the laser frequency with a shift that depends on the optical intensity and the ratio of power in the signal and pump beams.

2. much of FWM performance in Doppler-broadened media can be understood by estimating the effects of experimental parameters on the population of the velocity group in which the interference grating is written.

3. deleterious thermal motion effects, such as washout of the interference grating, can be aggravated as the homogeneous width

10

increases. Such increases are expected due to power broadening accompanying the strong saturation.

3.1.1 FWM in Saturable Absorbers

An important class of nonlinear optical materials are saturable absorbers. A strong optical nonlinear response is possible at low optical irradiance because the refractive index can be changed significantly near an optical transition due to saturation of the absorption.

A physical basis for understanding enhancement near optical transitions can be obtained by considering the behavior of the susceptibility, χ, near an optical transition. It is exactly this susceptibility that determines the polarization of the medium,

$$P = \chi E = \chi^{(1)} E + \chi^{(2)} E^2 + \ldots \tag{3-1}$$

where the nonlinear interaction is due to higher orders of χ and the E field, and the refractive index of the medium is proportional to χ. In general, the susceptibility has a real part, χ', giving rise to a polarization component in phase with E, and an imaginary component, χ'', which is out of phase. It is this out of phase component that is responsible for energy exchange between the fields and the medium, i.e., is the absorptive contribution to the total susceptibility and refractive index. The phase shift arises from the finite response time associated with the transition.

Both components of χ saturate in homogeneously broadened transitions. In the approximation of stationary atoms, the dispersive and absorptive components of χ saturate according to

$$\chi''(\Delta\omega) = \frac{\mu_{12}^2 \Delta N}{\hbar\Gamma} \left(\frac{1}{1 + (\Delta\omega/\Gamma)^2 + I/I_{sat}} \right)$$

$$\tag{3-2}$$

$$\chi'(\Delta\omega) = (\Delta\omega/\Gamma)\, \chi''(\Delta\omega)$$

where $\Delta\omega$ is the laser detuning from line center, Γ is the homogeneous line halfwidth, μ_{12} is the transition moment, ΔN is the population

difference between the two levels involved, and I_{sat} is the characteristic saturation intensity. Figure 3-1 shows these components near an optical resonance for three optical intensities (0, 1, and 100 times the saturation intensity, I_{sat}), illustrating that a substantial intensity dependence of the refractive index can be achieved for frequencies close to the optical resonance. Note that the vertical scale for I/I_{sat}=100 has been multiplied by 100, and that the absorptive component is essentially completely saturated for many homogeneous halfwidths, Γ. An important feature in understanding FWM in saturable absorbers is that the absorptive component, χ'', saturates more rapidly than the dispersive component. In fact, for media in the Doppler-broadened limit, where the power-broadened homogeneous width, $\Delta\omega_{pb}$, is much less than the Doppler width, $\Delta\omega_D$, only the absorptive χ'' saturates appreciably. The dispersive component (χ') is insensitive to field intensity because it consists of many overlapping tails of dispersion curves from the many homogeneous subcomponents of the line.

It is the field-dependent saturation characteristic of the susceptibility that gives rise to the optical nonlinearity. Equation 3-2 illustrates additional features of the nonlinear process when viewed in light of particular nonlinear experiments. In the case of four wave mixing, where the interference of the input waves generates a spatial variation of optical intensity, the nonlinearity depends on spatial differences of the susceptibility. From Equation 3-2 and Figure 3-1, it can be seen that the maximum difference in χ between two spatial regions will occur if one region is completely dark and the other is illuminated, a situation that will occur only if the interfering beams have the same intensity. In this case of equal pump and signal intensities, the maximum "contrast" or spatial variation in χ occurs close to the resonance transition frequency, changing from $\Delta\omega = 0$ at low optical intensity to $\Delta\omega = \Gamma$ when the intensity is high enough to strongly saturate χ''. This is because the susceptibility is saturated and close to zero for all frequencies in the light regions, but is nonzero close to the transition frequency in the dark regions. Thus for input beams with similar intensities, the maximum nonlinearity is within one homogeneous width of the transition frequency. This will also be true for input intensities
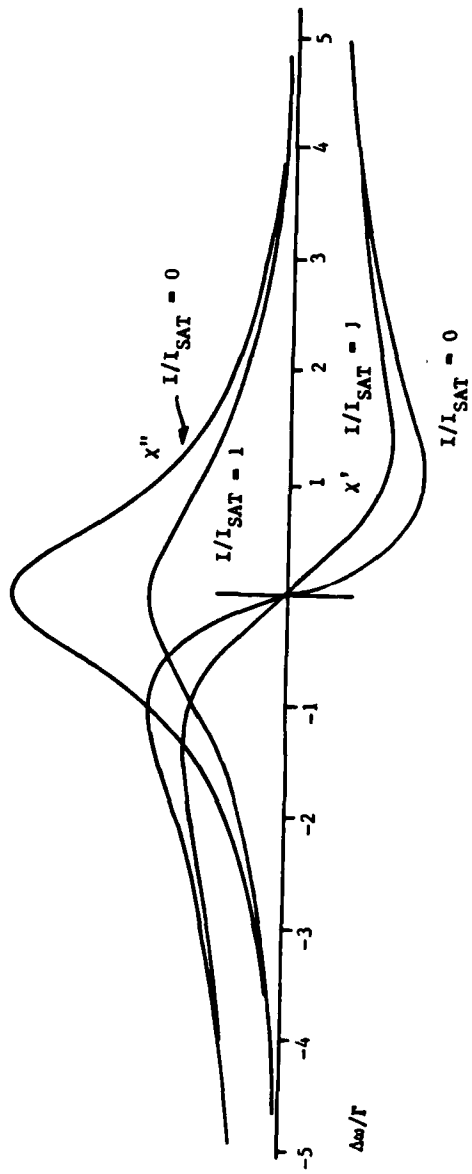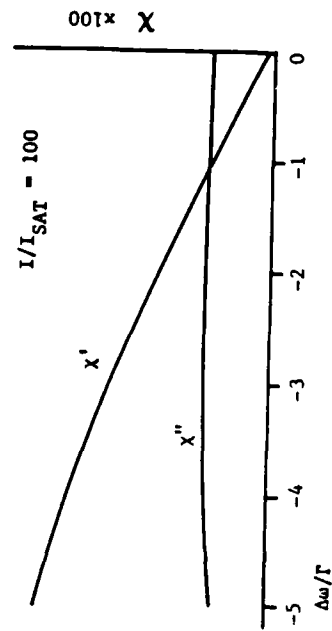
Figure 3-1. Saturating characteristics of the susceptibility, χ, for a homogeneously-broadened line. The vertical scale is expanded ($\times$ 100) for $I/I_{sat} = 100$ because both χ' and χ'' are strongly saturated.

13

that are small or comparable to I_{sat}, irrespective of the relative beam intensities. It should be noted that this discussion ignores the effects of residual absorption, so that the maximum nonlinear response may occur at a different frequency than where the contrast in χ is largest.

However, if strong, unequal input beams are involved, the situation is quite different. In such a case, both "dark" and "light" regions are strongly saturated. Near the transition frequency, the two regions saturate identically and there is no nonlinearity "contrast"; only for frequencies detuned on the order of $(I/3I_{sat})^{1/2}$ homogeneous linewidths from resonance will the two regions begin to saturate differently. Thus the best nonlinearity is achieved for substantial detunings from resonace under conditions of high optical intensity with low contrast between light and dark regions. It is this regime that is of particular interest to this program because we are interested in weak signal beams mixing with very strong pump beams. Consideration of this aspert of strong saturation in both light and dark regions is particularly important in understanding FWM in Doppler-broadened saturable absorbers such as sodium.

3.1.2 FWM in Doppler-Broadened Saturable Absorbers

In a homogeneously broadened transition, the resonance condition is given by

$$|\omega_L - \omega_0| \leq 2\Gamma \qquad (3-3)$$

i.e., the optical field frequency ω_L must be within a homogeneous linewidth of the isolated, stationary absorber transition frequency ω_0. Only part of the absorbers in a Doppler-broadened transition can interact with the optical fields because of the Doppler shifts induced by motion of the absorbers. In this case, the resonance condition now becomes

$$|\omega_L - \omega_0 - k_L \bullet v| \leq 2\Gamma \qquad (3-4)$$

where k_L is the optical wavevector and v is the absorber velocity. The

14

vector dot product $k_L \cdot v$ is the velocity component along the optical field propagation direction which gives rise to the Doppler shift of the resonance frequency ω_0. Thus, the optical field interacts resonantly only with absorbers that have velocity components that shift their (stationary) resonance frequency to that of the optical field.

The consequences of this selective velocity interaction in FWM experiments are several. Consider the standard counterpropagating pump beam FWM geometry illustrated in Figure 3-2. The forward pump, E_f, interacts resonantly with absorbers with velocity $v=(\omega_f-\omega_0)/k_f$. The signal beam, E_s, which intersects E_f at a small angle θ_{fs}, must interact with the *same* group of absorbers if an interference grating is to be produced; this requires that

$$|\omega_s - \omega_f| \leq 2\Gamma. \qquad (3-5)$$

Since the maximum contrast in χ is close to the Doppler-shifted resonance frequency of the absorbers simultaneously interacting with E_f and E_s, the efficient readout of the spatial grating requires that E_b be at this frequency where the χ contrast is largest. For low intensities, this is not at ω_f because the back pump is counterpropagating to E_f. Hence the absorbers interacting with E_f and E_s are only resonant with E_b if

$$|\omega_f + (k_f/k_b)\omega_b - (1+(k_f/k_b))\omega_0| \leq 2\Gamma \qquad (3-6)$$

In the case of degenerate four wave mixing (DFWM), the above resonance condition can only be satisfied for $\omega_L = \omega_0$ (or $v=0$). Figure 3-3 illustrates this for DFWM, showing the velocity groups that the different fields interact with. Figure 3-3 also shows χ' in frequency space showing the offset of the back pump from the frequency where χ' is largest. This illustrates that DFWM can be performed with the laser detuned from ω_0, but that χ is sampled off-resonance by $2k \cdot v$, resulting in a weak nonlinearity.

In fact the very low power, low Na density experiments reported in Reference 3-1 show DFWM reflectivity exactly on the stationary resonance ($v=0$) with a linewidth substantially narrower than the Doppler width. This

15
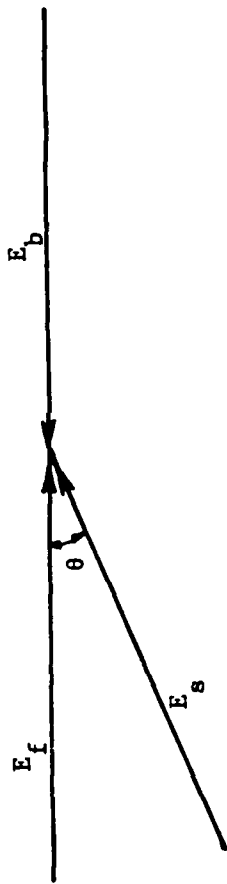
STANDARD PHASE CONJUGATING BACKWARD FWM CONFIGURATION

STANDARD CONFIGURATION IN VELOCITY SPACE

$$v_{s,x} = \frac{\Delta\omega\cos\theta}{k_s}$$

$$v_{s,y} = \frac{\Delta\omega\sin\theta}{k_s}$$

$$v_f = \frac{\Delta\omega}{k_f}$$

$$v_b = \frac{\Delta\omega}{k_b} = -v_f$$

Figure 3-2. Standard counterpropagating pump configuration for backward FWM phase conjugation. Also presented is the configuration in velocity space, showing the velocity groups resonant with each input wave.

16
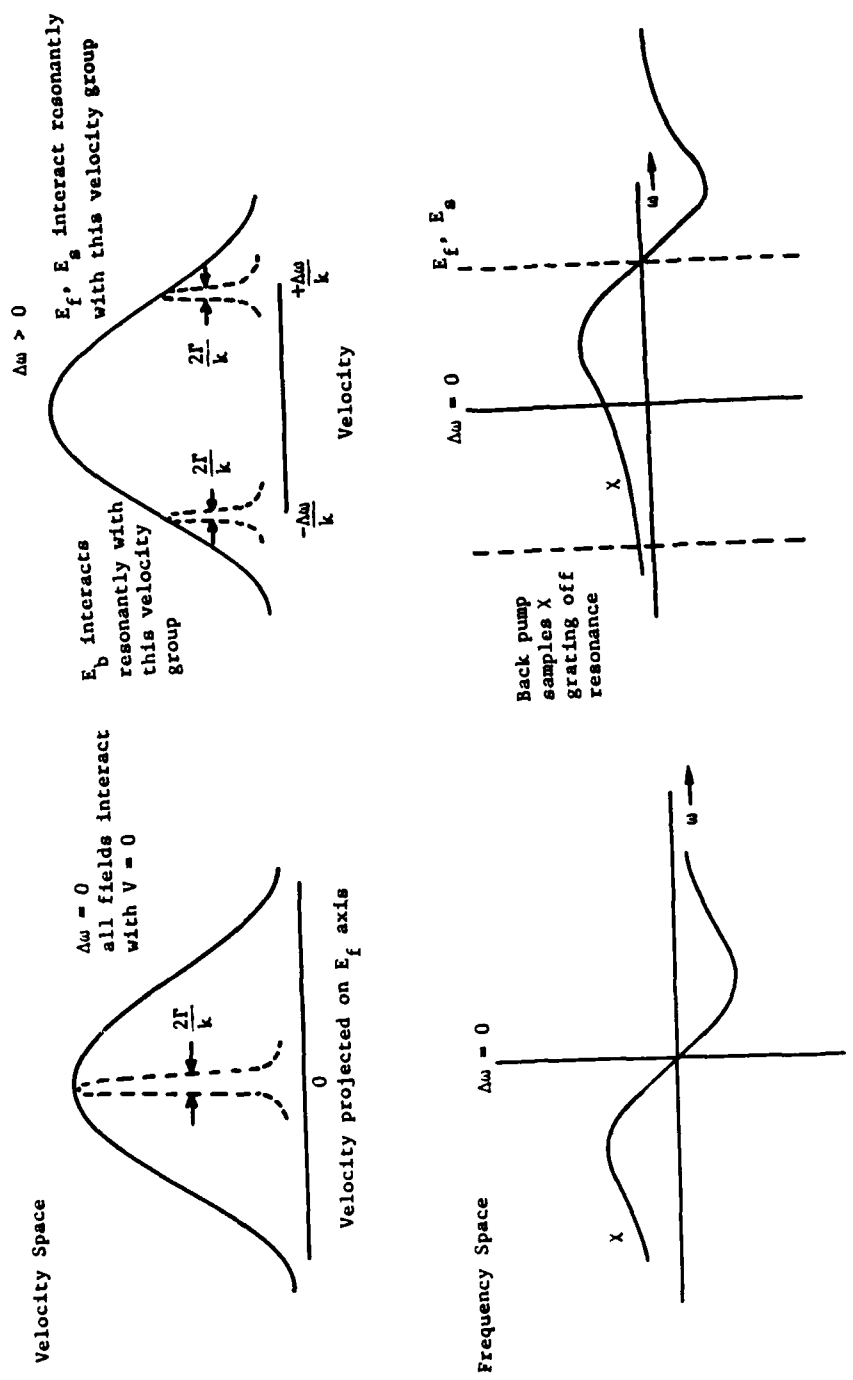
Figure 3-3. Interactions in velocity and frequency space for DFWM experiments performed on-resonance ($\Delta\omega = 0$) and off-resonance. When $\Delta\omega \neq 0$, the back pump does not interact resonantly with the velocity group in which the E_f/E_f grating is written. This grating is sampled off resonance by 2 $\Delta\omega/k$.

is as expected since under these conditions the deleterious effects of the small absorption at line center (ω_0, $v=0$) are unimportant and the nonlinearity is so small that it must be sampled on-resonance to achieve any DFWM reflectivity. Humphrey, et. al. (Reference 3-2) obtain similar results with linewidths approaching the homogeneous width of Na in the collisionless regime.

The situation under high reflectivity conditions of strong linear absorption and high pump intensity is quite different. When there is strong linear absorption near ω_0, higher reflectivity is actually achieved for off resonance operation. It is better to reduce the absorptive loss by detuning the laser frequency and "read" the nonlinearity nonresonantly. This is discussed in detail in Section 4.3.1.

Another consideration in Doppler-broadened saturable absorbers is the fraction of absorbers participating in the experiment. Figure 3-4 illustrates that absorbers with velocities within a range Γ/k_f of $v=\Delta\omega_f/k_f$, where $\Delta\omega_f$ is $\omega_f-\omega_0$, interact with E_f. These absorbers define a disc in 3-dimensional velocity space with a thickness along the direction of optical propagation of Γ/k_f, and a radial distribution given by the Maxwellian velocity distribution in the directions orthogonal to the propagation axis. A similar disc defines absorbers interacting with E_s. It is absorbers in the velocity volume defined by the intersection of these two discs that participate resonantly in establishing the spatial interference grating between E_f and E_s.

The number of absorbers in the intersecting volume is determined by their absolute velocity, i.e. the length of the vectors in Figure 3-4 that originate at $v=0$ and terminate within the selected volume. The magnitude of these velocities are, in turn, determined by the laser detuning from resonance, $\Delta\omega$, and the angle between the two fields in question. The fraction of absorbers with appropriate velocities, N_{ex}/N_{tot}, can then be determined from the Maxwell velocity distribution

$$N_{ex}/N_{tot} = (M/2\pi RT)^{3/2} \iiint \exp^{[-M(v_x^2+v_y^2+v_z^2)/2RT]} dv_x dv_y dv_z \qquad (3-7)$$

where the integration is over the intersecting volume. This fraction is a key parameter in determining the efficiency of the nonlinear process, and so considerable insight into the dependence of the FWM signal on various

18

Absorbers resonant with E_s

$\frac{2\Gamma}{k_f}$

$V_s = \frac{\Delta\omega}{k_s}$

Absorbers
simultaneously
resonant with E_s, E_f

$V = 0$ $V_f = \frac{\Delta\omega}{k_f}$

$\frac{2\Gamma}{k_s}$

Absorbers resonant with E_f

$\frac{2\Gamma}{k}$

Discs have soft
edges fading to
∞ with Maxwellian
velocity distribution

$V_s = \Delta\omega/k_s$

$V = 0$ $V_f = \frac{\Delta\omega}{k_f}$

$\frac{2\Gamma}{k}$
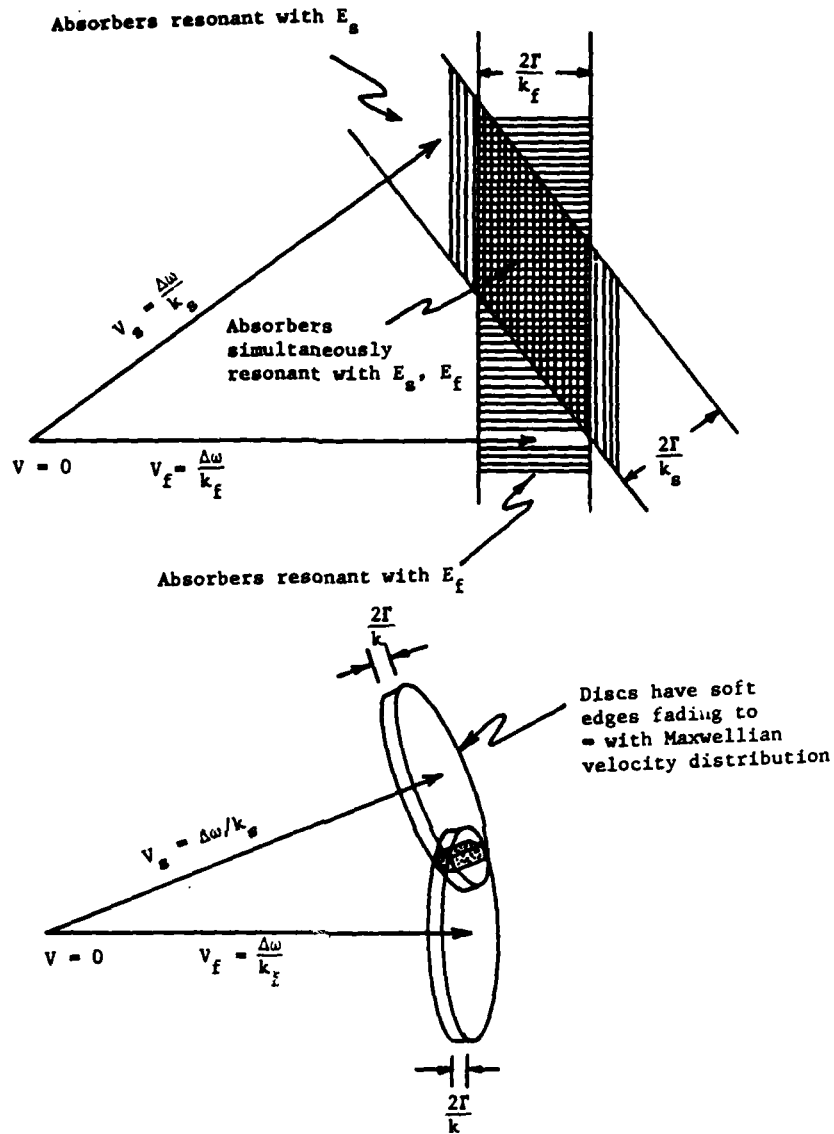
Figure 3-4.   Interaction of signal and forward pump beams in velocity
space.   Due to finite homc,eneous width, Γ, there are population
"diamonds" (2-D) of absorbers with velocities such that they can
simultaneously interact with both optical fields.   In three-
dimensional velocity spac-, the "diamonds" are actually the
intersection of pupulation discs.

parameters can be gained by considering the impact of experimental conditions both on the size of the intersection volume and on the magnitude of velocities contained within this volume.

As an illustration, consider Figure 3-5 which shows in two dimensions the intersecting volumes for degenerate optical fields crossing at different angles. The shaded diamond-shaped areas indicate the populations which have the proper velocities to simultaneously interact with the signal and forward or backward pump fields. Except in the case of exactly counterpropagating signal and pump fields, there is always a velocity group that is resonant with both fields regardless of $\Delta\omega$ (counterpropagating fields require $\Delta\omega=0$). However, as the crossing angle increases, the required velocity increases from a minimum of $\Delta\omega/k$ to ∞. This results in a rapid dropoff in absorber population participating resonantly in the experiment, particularly if $\Delta\omega$ is comparable to the Doppler width, $\Delta\omega_D$. This is because for this detuning, the minimum velocity (for colinear beams) already is approximately the average thermal velocity, v_T, a velocity where the Maxwellian distribution changes rapidly. Such detunings were found to be necessary experimentally for achieving high reflectivity. The thermal velocity is shown as the circle in Figure 3-5.

As an example of the power of this physical model for achieving a basic understanding of FWM physics, one can conclude from examining Figure 3-5 that the interference grating formed by the back pump, E_b, and E_s ("the back grating") will be increasingly unimportant in DFWM experiments in Doppler-broadened systems when $\Delta\omega$ is changed from zero. The very large crossing angle requires that the absorbers which can record the spatial interference pattern of the back grating have a very large velocity. Therefore only a small fraction of the total population can contribute to the FWM signal via the back grating under these conditions.

3.1.3 Other Effects due to Thermal Motion

In addition to the Doppler effects discussed in the last section, thermal motion of the absorbers also impacts a FWM experiment by "washing out" the interference gratings formed by E_f+E_s and E_b+E_s. These
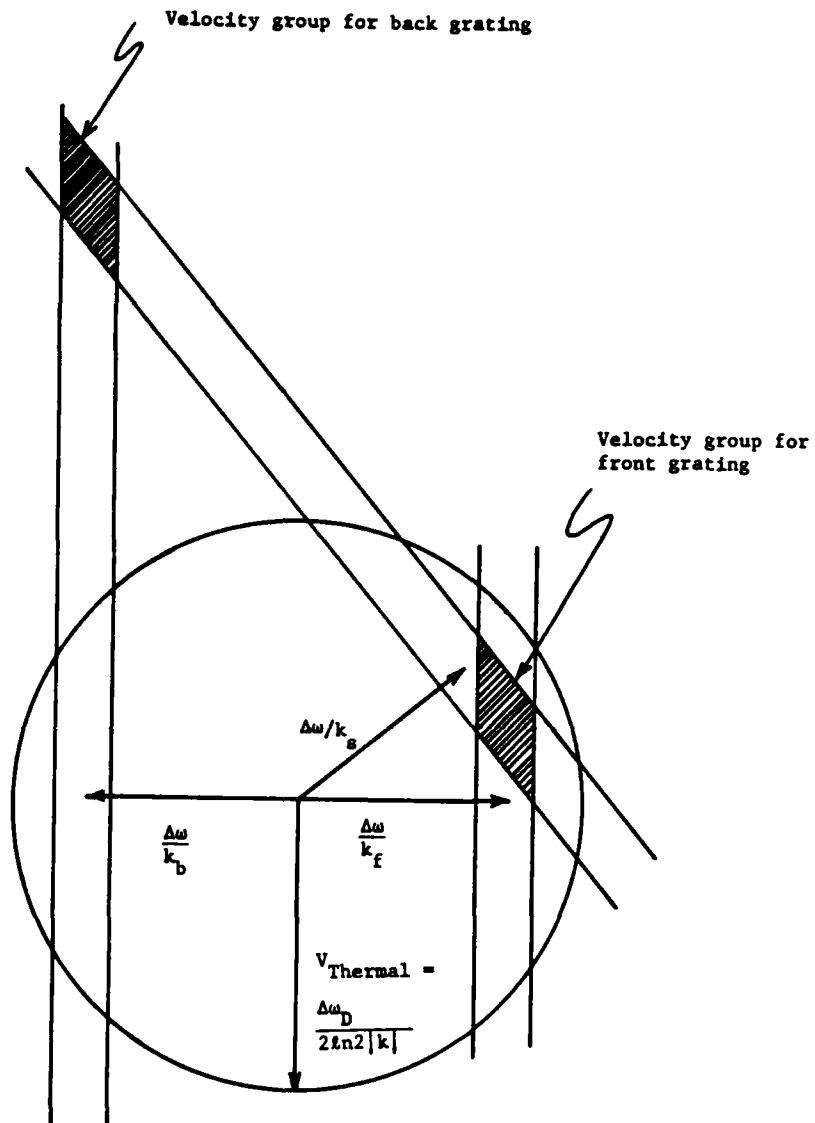
Figure 3-5. Velocity groups in which the forward (E_f/E_s) and back (E_b/E_s) gratings are written for DFWM. The circle corresponds to the thermal velocity. The back grating is usually unimportant because of the large velocity required to be simultaneously resonant with E_b and E_s.

gratings contain the unique spatial variation in refractive index that leads to scattering of pump energy into the signal and conjugate directions with exactly the correct phase relationship. The grating spacing for two plane waves E_f and E_s crossing at angle θ_{fs} is given by

$$\Lambda_{fs} = (\lambda/2)/\sin(\theta_{fs}/2). \qquad (3-8)$$

For arbitrary waves, the spacing between grating lines can vary somewhat because of spatial phase variations. The grating is oriented so that grating lines are parallel to the bisector of θ_{fs}, i.e. with a grating vector defined by k_f-k_s. It is the velocity component along the grating vector perpendicular to the grating lines that leads to thermal washout. Interestingly, the Doppler resonance condition selects absorbers with velocities primarily along the grating lines, i.e., with velocities that do not carry absorbers from light to dark regions. It is only because of finite homogeneous width that there is any cross grating line velocity, as illustrated in Figure 3-6.

The maximum cross grating velocity in the resonant velocity group is just $v=(\Gamma/k)/\sin(\theta/2)$, however there are only two points in velocity space, at two of the apices of the population diamond, that correspond to resonant absorbers with that cross grating velocity. The average grating destroying velocity is the weighted average over the upper (lower) half of the population diamond

$$
\langle v_{gd} \rangle = \frac{\displaystyle\int_{L1}^{L2}\int_{0}^{L3} v_{gd}\exp^{[-MV^2/2RT]}dV' + \int_{L2}^{L4}\int_{0}^{-L3} v_{gd}\exp^{[-MV^2/2RT]}dV'}{\displaystyle\int_{L1}^{L2}\int_{0}^{L3} \exp^{[-MV^2/2RT]}dV' + \int_{L2}^{L4}\int_{0}^{-L3} \exp^{[-MV^2/2RT]}dV'} \qquad (3-9)
$$

whe e

$$V^2 = (v_{gd}^2 + v_{x'}^2) \qquad dV' = dv_{gd}dv_{x'}$$

and the limits of integration are given by

$\frac{\lambda}{2} \sin (\theta/2)$

Velocity Space

Grating orientation
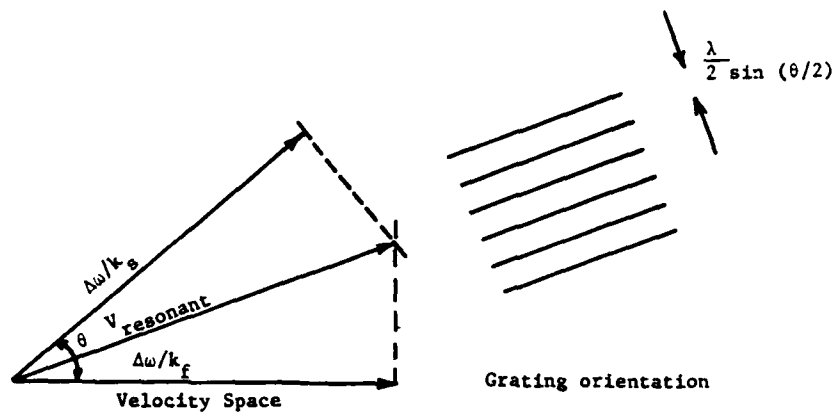
$\Gamma = 0$ Resonant absorbers have no cross grating
velocity component
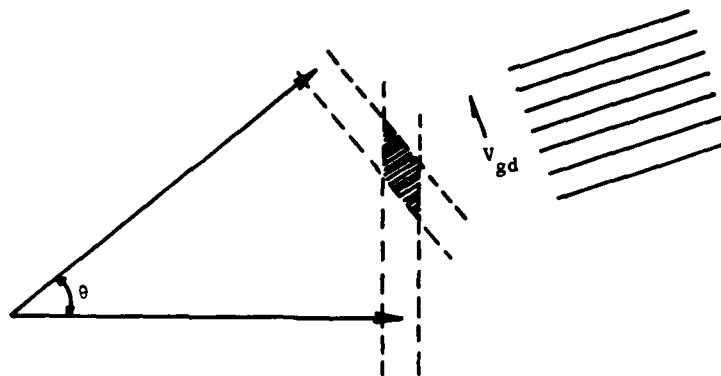
$\Gamma > 0$ Some resonant absorbers now have velocity components
that destroy the grating

Figure 3-6.   Grating washout due to cross-grating velocity, V_{gd}, requires
a finite homogeneous width when operating off-resonance.

$$L1 = \frac{\Delta\omega - \Gamma}{k \cos \theta/2} \qquad L2 = \frac{\Delta\omega}{k \cos \theta/2} \qquad L4 = \frac{\Delta\omega + \Gamma}{k \cos \theta/2}$$

$$L3 = (v_{x'} - L1) \cot \theta/2$$

The integration is over only one half of the diamond since velocities in either direction perpendicular to the grating are equally effective in washing out the grating ($<v_{cg}>$ is zero integrated over the entire resonant velocity diamond, but the gratings do indeed wash out!). Note that in the Doppler limit, $\Gamma \leq \Delta\omega_{pb} \ll \Delta\omega_D$, the velocity weighting in the direction of the grating lines ($v_{resonant}$ in Figure 3-6) is uniform across the population diamond and the average grating destroying velocity is given by

$$<v_{gd}> = ((2RT/(\pi M))^{1/2} \frac{(1 - \exp^{[-M\Gamma^2/(2RTk^2 \sin^2(\theta/2))]})}{\mathrm{erf}[M^{1/2}\Gamma/((2RT)^{1/2}\sin(\theta/2))]} \qquad (3-10)$$

Note that for the case where the two fields are colinear, $<v_{gd}> = (2RT/\pi M)^{1/2}$, which is $(2/\pi)^{1/2}$ times the one-dimensional rms velocity.

The thermal washout time, then, is the time required for absorbers to travel one-half the fringe spacing, i.e.,

$$t_{washout} = \lambda/[4\sin(\theta/2)<v_{gd}>] \qquad (3-11)$$

Several aspects of grating washout due to thermal motion can be appreciated from Equations 3-10 and 3-11. First, grating washout requires a finite homogeneous width Γ for $\theta_{fs} \neq 0$ because it is this width that gives rise to the population diamond and resonant absorbers with velocities different than $\Delta\omega/k\cos(\theta/2)$. Secondly, the average grating destroying velocity increases with Γ if one is still in the limit where the mean free path of the molecules is large compared to the physical dimensions of the interaction volume. This would be the case, for instance, if power-broadening was the dominant mechanism for homogeneous broadening, in which case Γ should be replaced by $\Delta\omega_{pb}/2$ in the

24

above equations.

3.2 SODIUM HYPERFINE SPECTROSCOPY

Many of the experimental results discussed in Section 4 depend
strongly on the characteristics of the particular sodium transition used
in these studies. All of the work reported here was performed at or near
the resonance of the $^3P_{1/2}$-$^3P_{3/2}$ transition, commonly called the
D_2 line. Because Na has a nuclear spin of I=3/2, the purely electronic
transition is broken into six closely spaced hyperfine components.
Therefore, calculations of saturation intensity, transition moment, linear
absorption, etc. need to account for the hyperfine components that are
involved. This is particularly the case when using laser sources with
linewidths small compared to the hyperfine splittings.

Figure 3-7 presents the hyperfine level structure of the D_2 line
and a stick spectrum showing the frequencies and relative line strengths
of the six dipole-allowed hyperfine transitions. The ground state
consists of two hyperfine levels, F=1 and F=2, separated by 1.77 GHz.
This splitting in the ground state accounts for the separation of the
hyperfine spectrum into two separate groups of three closely spaced
transitions, the F=1 to F'=0,1,2 group and another corresponding to the
F=2 to F'=1,2,3 lines. This second group is stronger in absorption, both
because the transition moments are larger and because the F=2 state has
5/8 of the ground state population due to the relative degeneracies of the
two ground state hyperfine levels. Relative line intensities, effective
Einstein A coefficents, and dipole transition moments of the six
transitions are listed in Figure 3-8. Because of the magnetic degeneracy
of the F and F' hyperfine levels, one must actually consider the dipole
moments of transitions between magnetic sublevels within a particular
hyperfine component to obtain the correct transition moment. This results
from the dependence of magnetic sublevel selection rules on the
polarization of the field, i.e. ΔM=0 for linear polarization, +1 for
right circular polarization, and -1 for left circular polarization. The
transition moments for individual magnetic sublevel transitions in the F=2
to F'=3 and F=1 to F'=0 transitions are listed in Figure 3-8 as examples

$3\ ^2P_{3/2}$

F' =

58.8 MHz   3

34.5 MHz   2

15.8 MHz   1

0

$16,973\ cm^{-1}$

F =

2

$3\ ^2S_{1/2}$

1.77 GHz

1

2-3

2-2

$16,973\ cm^{-1}$

1-1   1-2

2-1

1-0

-.7   -.6   -.4   -.2   0   .2   .4   .6   .8   1.0   1.1

$\frac{\Delta\omega}{2\pi}$(GHz)
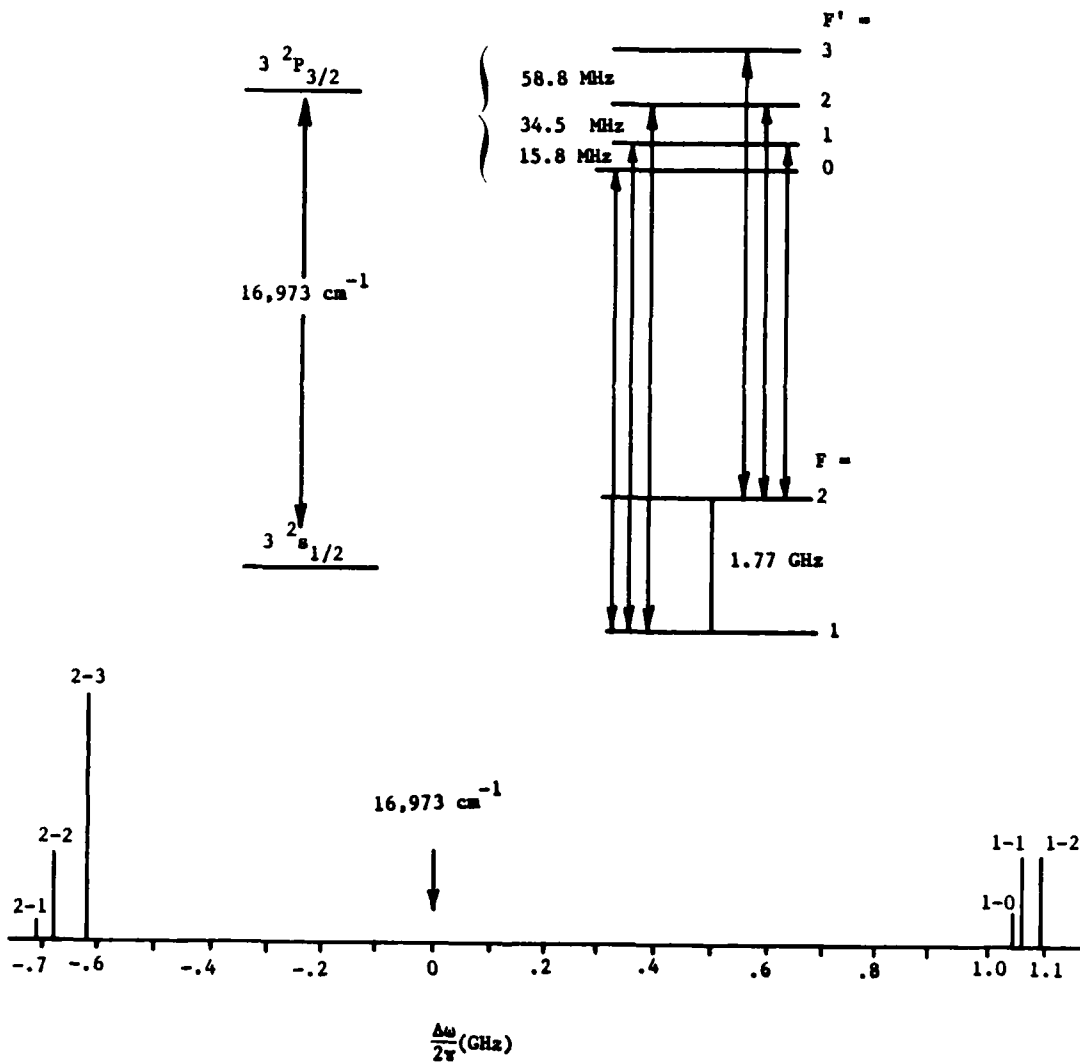
Figure 3-7.   Energy level diagram and hyperfine spectrum of the
Na D_2 line at 16,973 cm^{-1}.

26

ATOMIC SPECIES = Na D_2 - 5890 Angstrom Line

UPPER STATE ELECTRONIC ANG. MOMENTUM = 3/2
LOWER STATE ELECTRONIC ANG. MOMENTUM = 1/2
NUCLEAR MOMENTUM   = 3/2
ELECTRONIC TRANSITION A COEFFICIENT = 6.22×10^7 S^{-1}
TOTAL ELECTRONIC TRANSITION DIPOLE MOMENT = 1.27×10^{-17} esu·cm

F-UPPER	F-LOWER	Rel. Int.	Compt. A	Dipole Momnt (ESU*CM)
0	1	.0625	6.22×10^7	6.35×10^{-18}
1	1	.156	5.18×10^7	1.04×10^{-17}
1	2	.0313	1.03×10^7	4.49×10^{-18}
2	1	.156	3.11×10^7	1.04×10^{-17}
2	2	.156	3.11×10^7	1.04×10^{-17}
3	2	.437	6.22×10^7	1.68×10^{-17}

TOTAL NUMBER OF HYPERFINE LINES = 6

MAGNETIC SUBLEVEL TRANSITION MOMENTS

F:F'	M'-M	M	$\mu_{(F,M:F',M')} \times 10^{18}$
2:3	0	-2	-3.67
		-1	-4.64
		0	-4.92
		+1	-4.64
		+2	-3.67
	+1	-2	+1.61
		-1	+2.84
		0	+4.02
		+1	+5.19
		+2	+6.35
	-1	-2	+6.35
		-1	+5.19
		0	+4.02
		+1	+2.84
		+2	+1.61
1:0	0	0	+3.67
	+1	-1	+3.67
	-1	+1	+3.67

Figure 3-8. Spectroscopic parameters of the Na D_2 line.

27

since these two transitions are the most important in the FWM work reported here.

The frequency separations of the hyperfine transitions are large compared to the bandwidth of the CW ring dye laser used in our experiments (< 1 MHz), however the effects of Doppler broadening make it impossible to isolate individual hyperfine components. Figure 3-9 shows the overlapping Doppler-broadened lineshapes of the six transitions (T = 500 K), along with their sum, which is the absorption lineshape expected for the D_2 line. It is readily apparent that a laser at frequency ω_L can be simultaneously resonant with several different hyperfine transitions, albeit with different velocity groups because $\Delta\omega$ will be different for the different transitions. Each transition will contribute to the FWM response at ω_L according to its dipole moment and $\Delta\omega$, which determines the population fraction and the amount off-resonance the nonlinearity is "read" in a DFWM experiment. This concept is illustrated in Figure 3-10a, which shows the two-dimensional population diamonds resonant with the different hyperfine transitions when the laser is tuned to the 1-0 frequency, ω_{1-0}. Clearly, there is substantial population with velocities such that the laser is also resonant with the 1-1 and 1-2 transitions because their (angular) frequency offsets from ω_{1-0} (100 and 314 MHz respectively) are small compared to the Doppler width of 10.7 GHz at 500 K. The fact that the F=2 to F'=1,2,3 transitions are about 10.7 GHz away suggests that they also contribute very weakly due to velocity components in the wings of those lines.

The contribution of the 1-1 and 1-2 transitions to the FWM response at $\omega_L-\omega_{1-0}$ is limited however by the effects of optical pumping. Optical pumping arises when population pumped from the lower hyperfine state (F=1) into a particular upper hyperfine state can radiate to other lower state hyperfine levels (in this case F=2). Since the F=2 state is not connected with any of the upper hyperfine levels by the optical field, the effect of driving the 1-1 and 1-2 transitions is to pump population from one of the groundstate hyperfine components (F=1) to the other (F=2). The F=1 population is removed in those velocity groups where the 1-1 and 1-2 transitions are resonant with the laser, and hence the contribution of these transitions to the FWM response is reduced to zero.

Actually, the F=1 population is not completely removed due to the
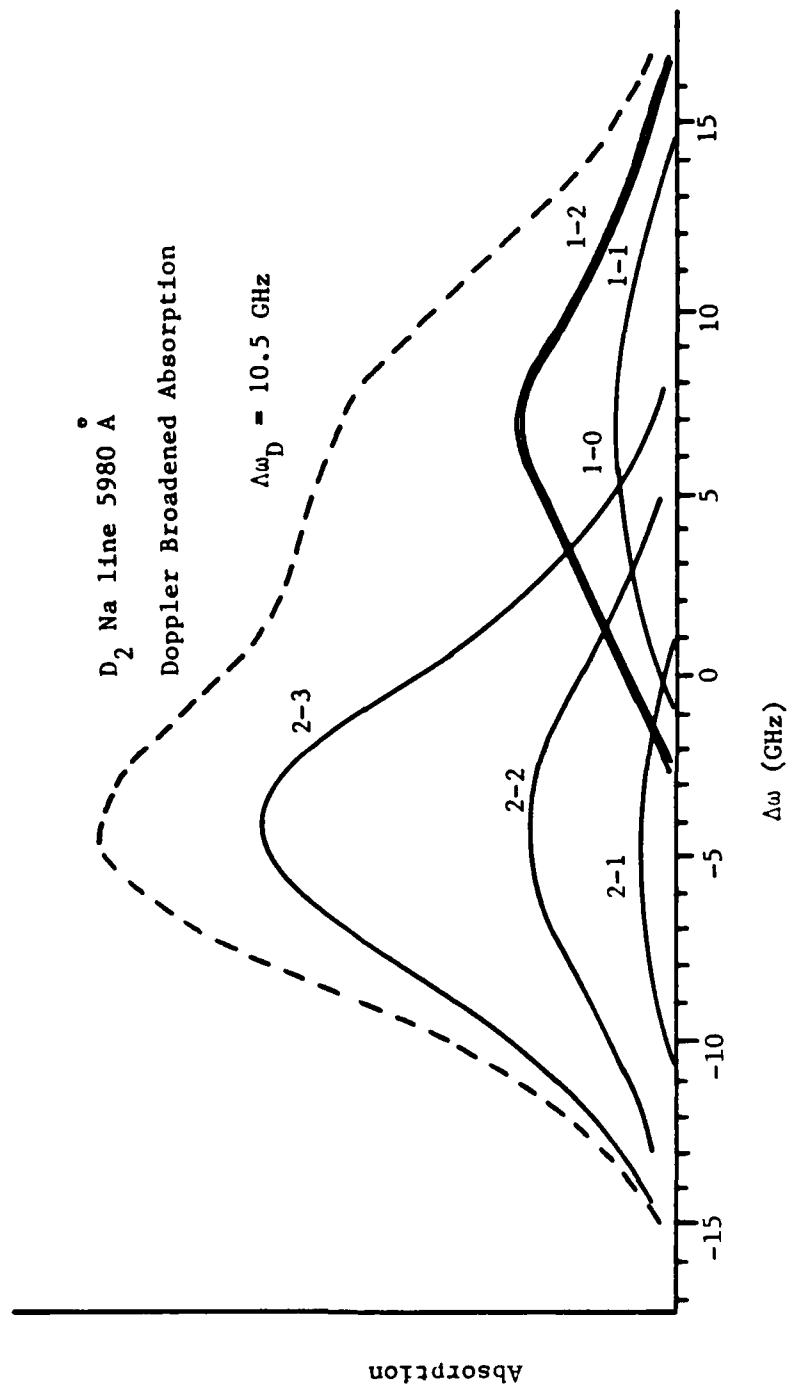
Figure 3-9. Doppler-broadened profiles of the six Na D_2 line hyperfine components at T = 500 K. Shown are the relative intensities and their sum, which represents the observed D_2 line absorption profile.

29

a) Low Power

$\omega_L = \omega_{1-0}$

$\Delta\omega/k_s$

1-2

.05 $V_{thermal}$

@ 500 K

1-0

1-1

$\Delta\omega/k_f$

300 cm/s = $\frac{r}{k}$

b) High Power I/I_{SAT} (1-0) = 1000

Only this thin velocity region is resonant with 1-0 and not optically pumped via 1-1 and 1-2 transitions

1/3 $V_{thermal}$
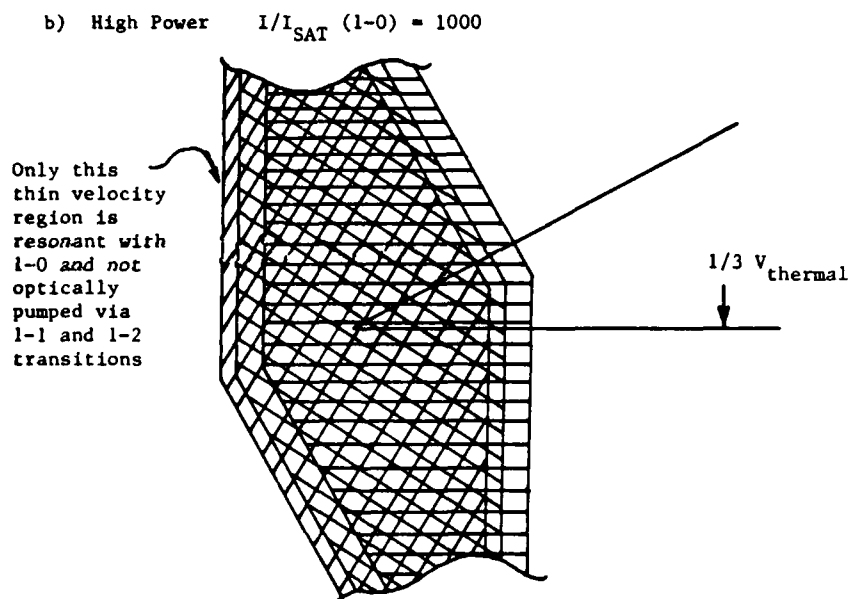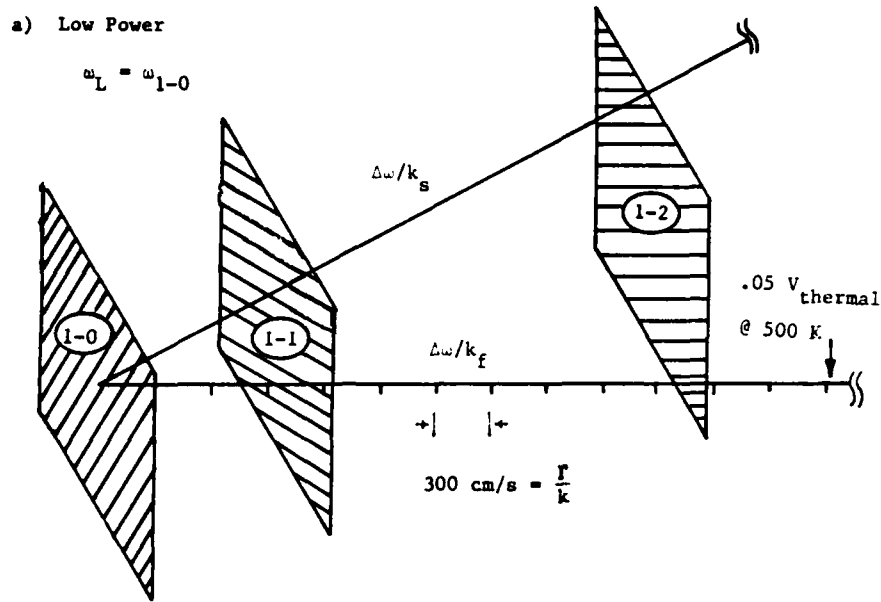
Figure 3-10.   a).   At low power, the velocity groups resonant with the 1-0, 1-1, and 1-2 transitions are distinct. Each contributes to FWM reflectivity, however optical pumping reduces the F = 1 population for the 1-1 and 1-2 transitions. b). The three velocity groups overlap strongly under high power conditions. Most population in the 1-0 diamond is also in the 1-1 and 1-2 diamonds and subject to optical pumping.

30

mitigating impact of diffusion. Na atoms with the appropriate velocities diffuse from unradiated regions into the laser beam; the steady state F-1 population is determined by the optical pumping rate compared to the diffusional rate. As a result, the 1-1 and 1-2 transitions will have a nonzero contribution to the FWM response. For low optical power DFWM experiments, the contribution will be very small because the nonlinearity is being "read" off resonance as discussed above in Section 3.1. Another mechanism for mitigating the effects of optical pumping is to consider the overlap of the wings of the F=2 to F'=1,2 transitions with the laser frequency. This provides a mechanism for optical pumping from F=2 to F=1, counteracting the optical pumping in the other direction. However, this mechanism can only occur when the homogeneous width is substantial because the two velocity groups involved in the F=1 transitions and the F=2 transitions are very different. Velocity changing collisions in fact would lead to the large homogeneous width required, however such conditions were not realized in the experiments reported here.

When strong optical fields are employed, the situation is somewhat more complex than illustrated in Figure 3-10a. Under these conditions, the homogeneous width increases due to power broadening according to

$$\Delta\omega_{pb} = 2\Gamma(1+I/I_{sat})^{1/2} \tag{3-12}$$

where Γ is the homogeneous half width at low power and

$$I_{sat} = I_{sat}(\Delta\omega=0,v=0)(1+(\Delta\omega-k\bullet v)^2/\Gamma^2) \tag{3-13}$$

is the local saturation intensity for velocity group v and laser detuning $\Delta\omega$. Figure 3-10b illustrates the case when the power-broadened homogeneous width exceeds the frequency separation of the 1-0,1-1, and 1-2 transitions when ω_L is tuned to ω_{1-0}. While the population diamond for the 1-0 transition is substantially larger because of the increased homogeneous width, much of the population is subject to optical pumping because of the overlapping diamonds of the 1-1 and 1-2 transitions. As discussed above, the F=1 population for velocities in the overlapping regions is reduced.

In addition to the overlapping populations in velocity space, one

31
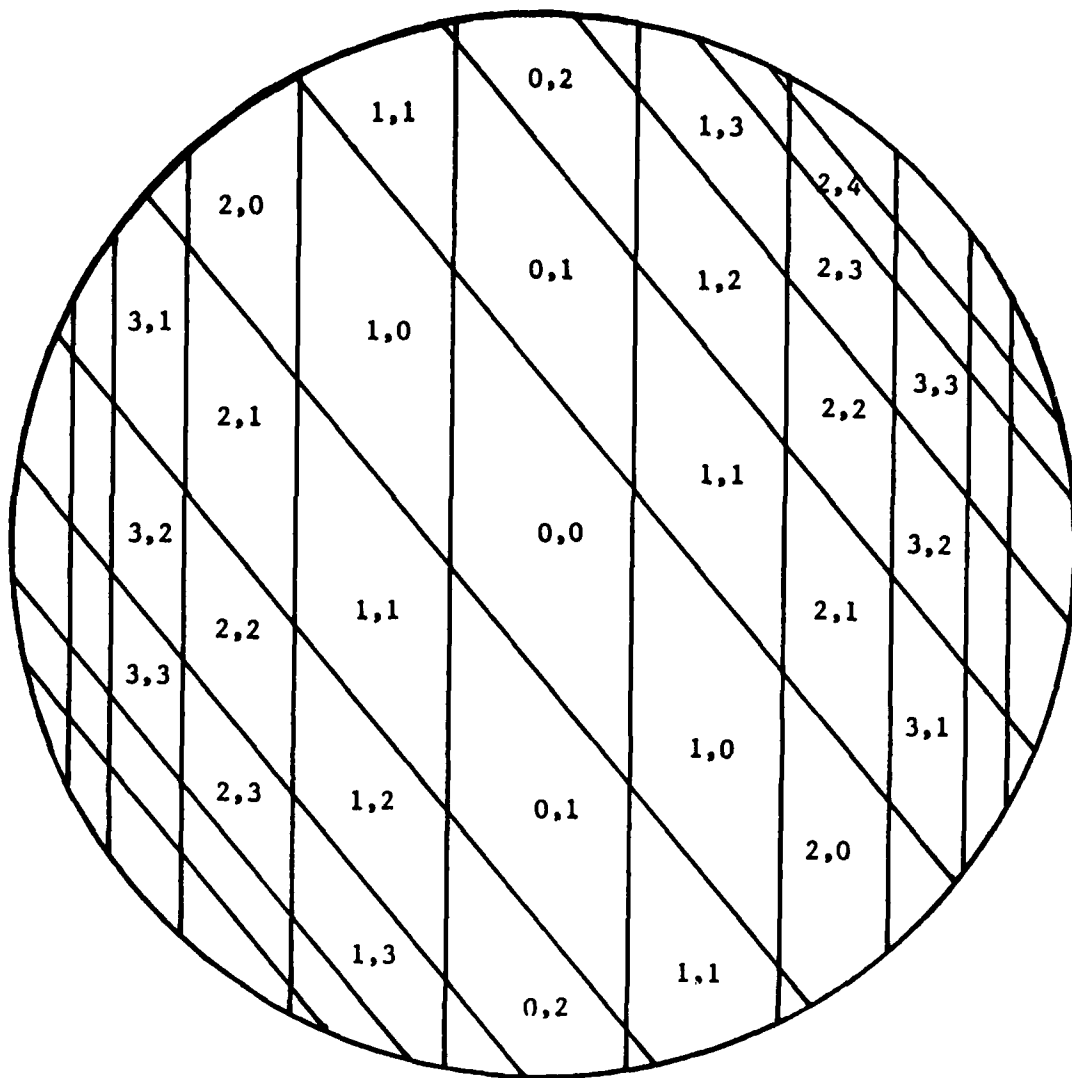
Figure 3-11. A population diamond grid showing on and off resonance
diamonds. The numbers in the diamond represent the
number of homogeneous linewidths off-resonance of E_f
and E_s respectively.

must consider the effect of strong optical fields on the nonlinearity. For strongly saturating fields, the maximum nonlinear response in frequency space can occur many homogeneous linewidths off resonance (see discussion in Section 3.1). As a result, the on-resonance population diamonds illustrated in Figure 3-10a and 10b may be contributing only weakly to the FWM response. Off-resonance population diamonds, where the optical field can sample χ at the frequency where the contrast is largest, can contribute more if they have a sufficient population fraction. The three hyperfine components still remain coupled in the same way as illustrated in Figure 3-10b. but it is the overlap of off-resonance diamonds that is pertinent. Because the power broadening is dependent on $\Delta\omega-k\cdot v$, the populations of diamonds decrease with increasing detuning from the laser; this is illustrated in Figure 3-11. Actually, it is only the area (volume) of the population diamonds that decreases; the velocity distribution must also be considered to estimate the actual change in participating population.

The coupling of the 1-0, 1-1, and 1-2 transitions is just the overlap of three such grids, each centered on its own resonant velocity group. It should be noted that the spacings in the three grids are not identical because $I_{sat}(\Delta\omega=0, v=0)$ is different for each of the transitions. Furthermore, it should be appreciated that the population diamonds are not hard "boxes"; rather the grid lines in Figure 3-11 represent the Doppler-shifted velocities corresponding to the half-height of Lorentzian distributions in frequency space. Thus there is some overlap of tails in the population diamond grid that is not adequately represented in diagrams of population diamonds.

3.3 ANALYTICAL APPROACH

A major objective of this program was to determine FWM characterisitics and capabilities in sodium vapor under the high CW reflectivity conditions that many missions are likely to require. As a result, the experiments were neither in the homogeneous or Doppler limits even though the laser bandwidth was generally very narrow in comparison with Γ, the intrinsic homogeneous width of the system. This is because of substantial power-broadening of the lines (c.f. Equation 3-12) induced by the strong

optical pumping fields. For the 50-100 W/cm^2 pump fields employed in our experiments, I/I_{sat} is 10^3-10^4 giving rise to power-broadened linewidths, $\Delta\omega_{pb}$, 30-100 times the collision-free intrinsic homogeneous width of Γ=62.5 MHz. Thus the homogeneous width was 20-60% of the Doppler width, too large to satisfy the Doppler limit condition that the homogeneous linewidth (including power broadening) be very small compared to the Doppler width. The Doppler limit is tantamount to saying the field interacts only with absorbers within a very narrow velocity spread, i.e., the effects of thermal motion in the ensemble can be ignored. The Doppler-broadened regime is inherently an "on-resonance" small-signal regime so the nonlinearity is primarily an absorptive (χ'') one. For the experimental conditions in our experiments, so few homogeneous subcomponents span the line ($\Delta\omega_{pb} \sim .2\Delta\omega_D$) the assumption that χ' doesn't saturate is no longer valid. In fact, Woerdman and Schuurmans (Reference 3-3) present results for experiments in the same experimental regime indicating that to first order, the nonlinear polarization obtained in the absence of strong linear absorption or pump depletion can be modeled reasonably well as a purely dispersive suscept-ibility with saturation effects.

Our experimental conditions for high reflectivity did not satisfy the homogeneous limit either. Because $\Delta\omega_{pb} < \Delta\omega_D$, the total ensemble of sodium can behave homogeneously only when the laser detuning $\Delta\omega$ is much larger than $\Delta\omega_D$, a situation where the complicating effects of thermal motion can be ignored (except for grating washout). All velocities respond to the field essentially identically because $\Delta\omega \gg$ $k \cdot v_i$ for all i. In this case, the nonlinearity is strictly dispersive because the interaction is far off-resonance. The intermediate case, where $\Gamma < \Delta\omega_{pb} < \Delta\omega_D$ is substantially more difficult to treat because many velocity groups contribute to varying degrees, just as one would expect from the physical picture described above. TRW started an effort to describe this experimental region theoretically; the effort is described in Section 7. However, to date there is no tractable analytic solution for this regime. For this reason, the experimental results will be discussed primarily in terms of the physical picture. The importance of FWM in homogeneously broadened systems was not discounted, however, and several models were developed

optical pumping fields. For the 50-100 W/cm^2 pump fields employed in our experiments, I/I_{sat} is 10^3-10^4 giving rise to power-broadened linewidths, $\Delta\omega_{pb}$, 30-100 times the collision-free intrinsic homogeneous width of $\Gamma=62.5$ MHz. Thus the homogeneous width was 20-60% of the Doppler width, too large to satisfy the Doppler limit condition that the homogeneous linewidth (including power broadening) be very small compared to the Doppler width. The Doppler limit is tantamount to saying the field interacts only with absorbers within a very narrow velocity spread, i.e., the effects of thermal motion in the ensemble can be ignored. The Doppler-broadened regime is inherently an "on-resonance" small-signal regime so the nonlinearity is primarily an absorptive (χ'') one. For the experimental conditions in our experiments, so few homogeneous subcomponents span the line ($\Delta\omega_{pb} \sim .2\Delta\omega_D$) the assumption that χ' doesn't saturate is no longer valid. In fact, Woerdman and Schuurmans (Reference 3-3) present results for experiments in the same experimental regime indicating that to first order, the nonlinear polarization obtained in the absence of strong linear absorption or pump depletion can be modeled reasonably well as a purely dispersive suscept- ibility with saturation effects.

Our experimental conditions for high reflectivity did not satisfy the homogeneous limit either. Because $\Delta\omega_{pb} < \Delta\omega_D$, the total ensemble of sodium can behave homogeneously only when the laser detuning $\Delta\omega$ is much larger than $\Delta\omega_D$, a situation where the complicating effects of thermal motion can be ignored (except for grating washout). All velocities respond to the field essentially identically because $\Delta\omega \gg k\cdot v_i$ for all i. In this case, the nonlinearity is strictly dispersive because the interaction is far off-resonance. The intermediate case, where $\Gamma < \Delta\omega_{pb} < \Delta\omega_D$ is substantially more difficult to treat because many velocity groups contribute to varying degrees, just as one would expect from the physical picture described above. TRW started an effort to describe this experimental region theoretically; the effort is described in Section 7. However, to date there is no tractable analytic solution for this regime. For this reason, the experimental results will be discussed primarily in terms of the physical picture. The importance of FWM in homogeneously broadened systems was not discounted, however, and several models were developed

35

during this program. They are also discussed in Section 7.

3.4 REFERENCES

3-1   J. F. Lam, D. G. Steel, R. A. McFarlane, R. C. Lind, Appl. Phys.
      Lett. 38, 977 (1981); D. G. Steel and R. A. McFarlane, Phys. Rev.
      A27, 1687 (1983).

3-2   L. M. Humphrey, J. P. Gordon, P. F. Liao, Opt. Lett. 5, 56 (1980).

3-3   J. P. Woerdmann and M. F. H. Shuurmans, Opt. Lett. 6, 239 (1981).

4.0 REFLECTIVITY MEASUREMENTS

This section reports experimental data and analysis of the observed functional dependence of FWM reflectivity on parameters of practical concern such as pump intensity, frequency offset, and signal viewing angle (field of view). Data was obtained for both narrowband ($\Delta\nu \sim 1$ MHz) and broadband ($\Delta\nu \sim 2$ GHz) laser operation, and interpreted in terms of the model presented in Section 3.

4.1 REFLECTIVITY MEASUREMENT OBJECTIVES

Many proposed mission applications of four wave mixing technology require phase conjugation of optical signals returning from a remote target. Good FWM reflectivity is generally necessary, but from a practical point-of-view must be obtained using CW or long-pulsed pump sources because of target range uncertainty that translates into timing uncertainties for pump pulses in the FWM medium. For this reason, the major emphasis of our reflectivity experiments was to determine characteristics of sodium FWM using modest CW pump powers in a configuration that resulted in high (> 100%) reflectivity. Frequency offset of peak reflectivity, field-of-view, and intensity dependence were measured because all have significant impact on the practical implementation of this technology. This same motivation of determining FWM reflectivity under conditions that can be easily implemented also gave rise to our objective to understand reflectivity under broadband laser excitation. Such information allows system designers to trade off FWM performance with complexity and fieldability of the pump lasers.

4.2 EXPERIMENTAL DESIGN

All degenerate four wave mixing experiments shared a common skeletal arrangement which is diagrammed in Figure 4-1. A Coherent 20 W Ar^+ pump laser and 699-21 ring dye laser typically generated 700-800 mW single frequency (measured to be <1.5 MHz FWHM) or 1.3 W broadband (~2 GHz FWHM) output at the Na D_2 wavelength. The dye laser output was s-polarized to all reflecting optics in both the pump and probe/noise beam

37
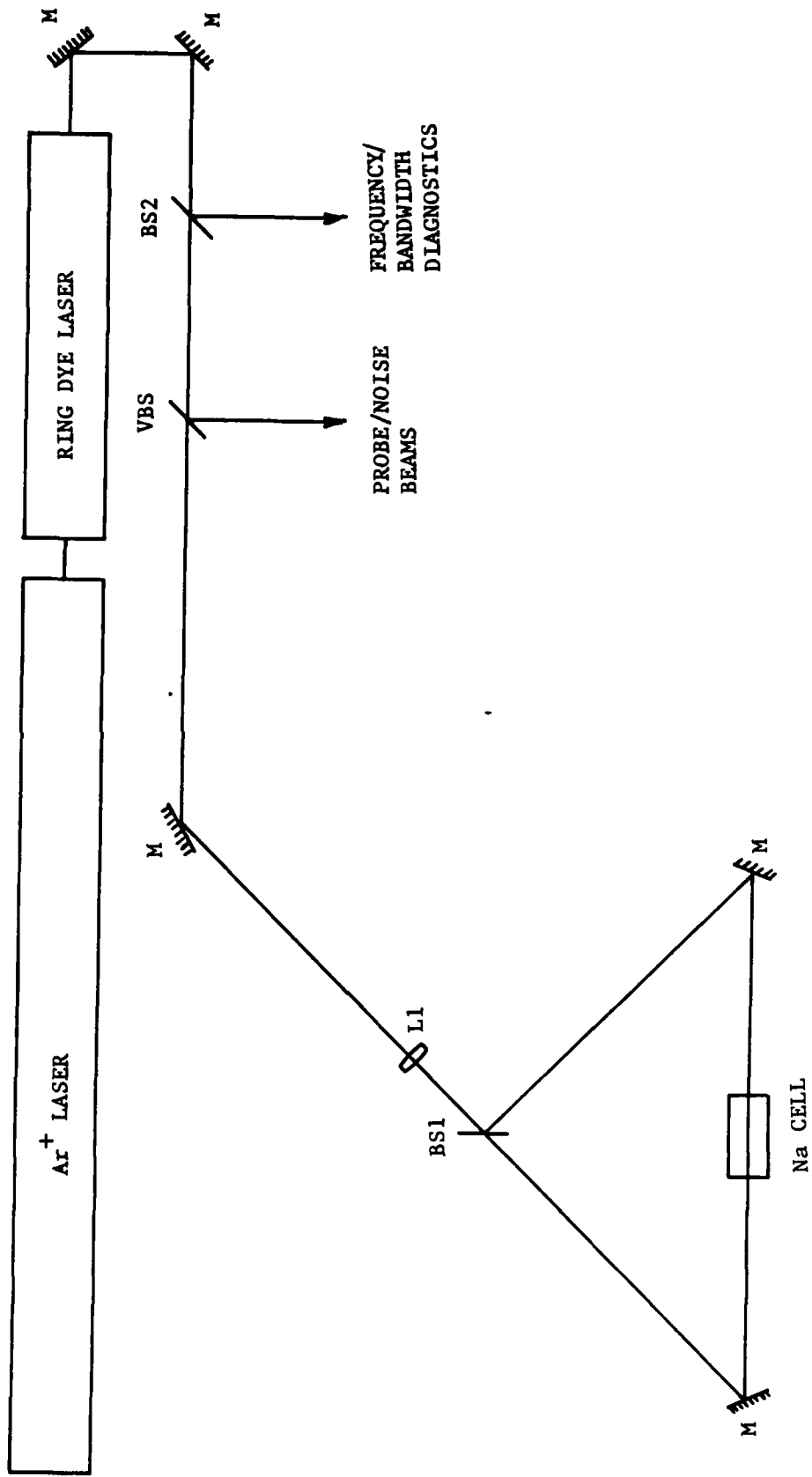
Figure 4-1. Basic experimental layout for DFWM phase conjugation experiments in sodium vapor.

paths to insure a high degree of copolarization at the Na cell. Turning mirrors (M) were visible dielectric or MAXBRIte™ coated Zerodur substrate optics with twentieth wave or better surface figures. A 50-50 beamsplitter (BS1) served to generate the two pump beams and was angle tuned to power match both pump legs to within 5%. Lens L1, a 90.0 cm focal length spherical achromat, imparted equal convergence to each pump leg resulting in equal intensity counterpropagating pump fields at the Na cell. BS2 was a 4% first surface, AR coated second surface beamsplitter which provided a sampling of the main beam for frequency and/or bandwidth analysis. The probe and noise beams originated from a high quality variable beamsplitter (VBS) inserted into the main beam path which, depending on the particular experiment at hand, would allocate the necessary amount of power into the probe/noise leg.

Laser bandwidth was measured with either a 150 MHz free spectral range (FSR) confocal Fabry-Perot etalon with a finesse of 100 for single frequency operation, or a 2 GHz FSR Fabry-Perot of finesse 50 for broadband output. Rough laser frequency measurements to ~ 1 GHz accuracy were made by a Burleigh wavemeter; for higher accuracy frequency measurements, an on line Lamb dip frequency diagnostic was assembled. Following the experimental approach of Hansch et al. (Reference 4-1), a reference beam and probe beam of equal intensities were produced from the two surfaces of an uncoated flat (see Figure 4-1). The two beams were directed through a 10 cm Na vapor cell which typically operated at 400-410 K. A third saturating beam was sent through the Na cell in a counterpropagating direction to the probe and reference beams and carefully overlapped the probe beam path in the cell. The output of the probe and reference beams was detected by matched photodiodes and sent to a high sensitivity differential amplifier whose output was displayed on an oscilloscope. With proper cell temperature and beam overlap, two lines were clearly detected (lower trace, Figure 4-2) representing transitions originating from the hyperfine split $3s^2S_{1/2}$ ground state of the Na D_2 line. Since the positions of these transitions are accurately known, frequency accuracy to 50 MHz was possible.
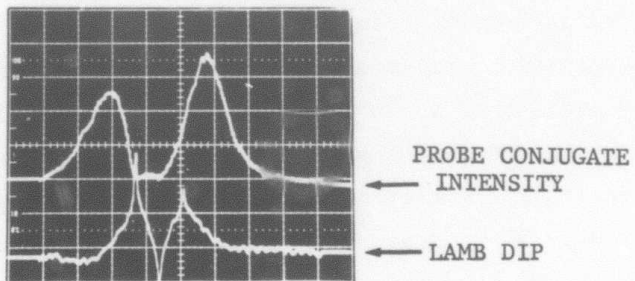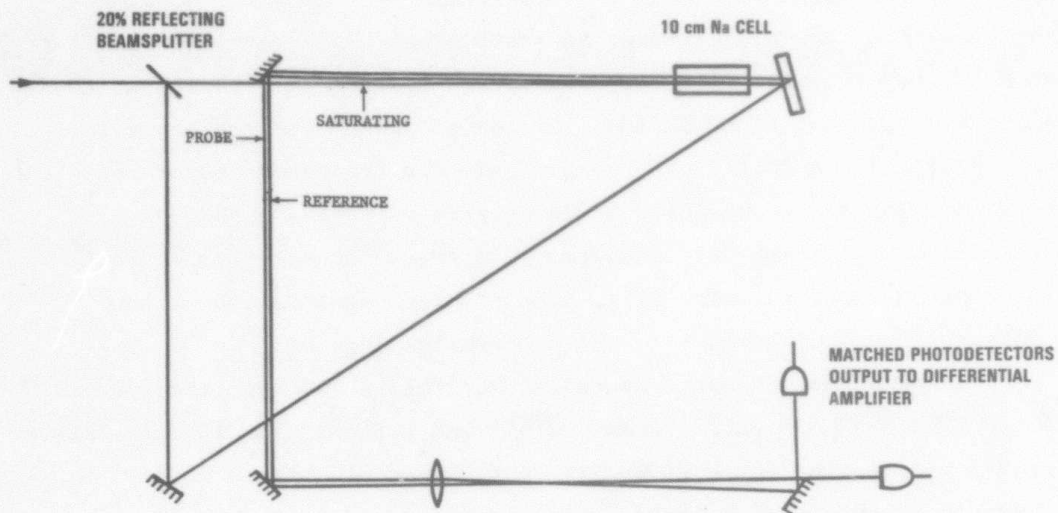
Figure 4-2. Lamb Dip Experiment Layout and Sample Result.

4.3 NARROWBAND LASER PUMPING RESULTS ($\Delta\nu < 1$ MHz)

4.3.1 DFWM Reflectivity Frequency Spectrum

The observed frequency dependence of the DFWM reflectivity in the narrowband dye laser experiments will be examined in this section. For small pump intensities, it has been shown that optical pumping effects play an important role in the FWM of the sodium D_2 resonance line (Reference 4-2). When resonantly driving the D_2 line, only the 2-3 and 1-0 hyperfine transitions are free from optical pumping and are, therefore, the only ones which contribute significantly to the steady-state DFWM reflectivity at low pump powers. This was discussed in some detail in Section 3.2. At high pump powers, which are required when large DFWM signals are desired, all six D_2 hyperfine transitions can contribute to the signal, but in a complicated way that depends on optical pumping, diffusion in and out of the beam, the explicit values for the detuning from each of the hyperfine transition frequencies ($\Delta\omega_i = \omega_L - \omega_i$), and the homogeneous power-broadened widths, $\Delta\omega_{pbi}$.

Figure 4-3 shows the frequency dependence of FWM reflectivity for experimental conditions giving very high reflectivites (R= 160-230%). In this case, as well as the conditions in Figure 4-4 for conditions of lower R, the maximum reflectivity of the 2-3 transition occurs on the low frequency side of its Doppler-broadened absorption line whereas the maximum reflectivity for the 1-0 transition occurs on the high frequency side of its Doppler-broadened absorption.

This spectral dependence can be understood as follows. In all of these cases, the on-resonance absorptive component is well saturated because $I/I_{sat} \gg 1$. Because the dispersive component of the nonlinearity is zero at resonance (c.f. Figure 3-1), one expects a dip in FWM reflectivity at resonance; such dips have been reported previously (References 4-3, 4-4). In our experiments, the reflectivity does indeed drop off near the 2-3 and 1-0 resonances for this reason, but does not recover for frequencies between those two resonances because of the very strong linear absorption still present in the center portion of the Doppler-broadened D_2 line. The absorption is strongly saturated in this region, being 10-100 times smaller than the small-signal attenuation,

PEAK FWM REFLECTIVITY ∿ 160%
(230% observed)

DOPPLER ABSORPTION PROFILE
OF D_2 LINE

ω_o (2-3) ω_o (1-0)

DFWM REFLECTIVITY

−5 −4 −3 −2 −1 0 1 2 3 4 5 6

FREQUENCY OFFSET FROM CENTER OF D_2 LINE, $\Delta\nu$ (GHz)
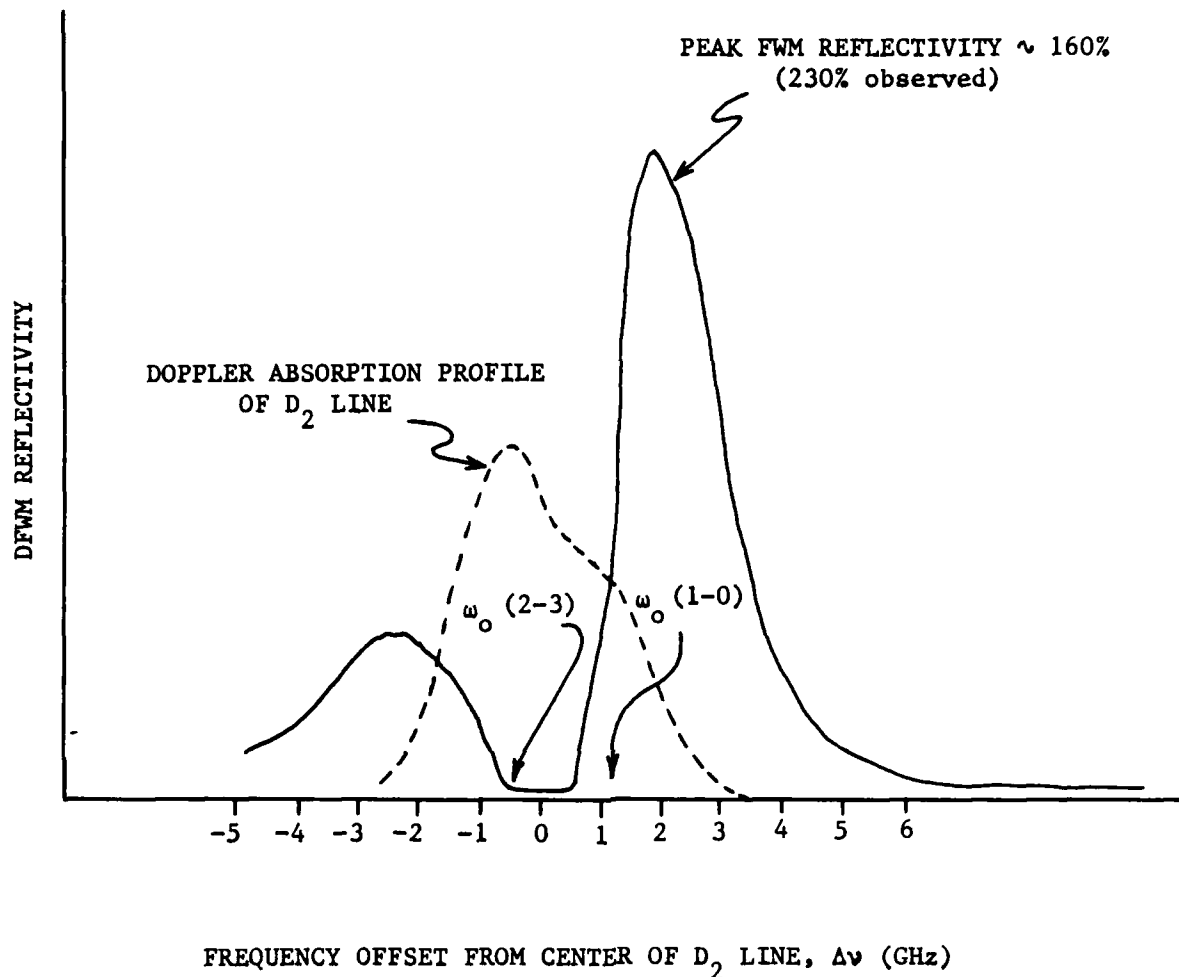
Figure 4-3. Typical frequency spectrum of the DFWM reflectivity under high
(R > 100%) conditions. The spectrum was obtained by scanning
a narrowband dye laser through the Na D_2 resonance. Shown for
reference is the relative Doppler absorption profile of the D_2
line.
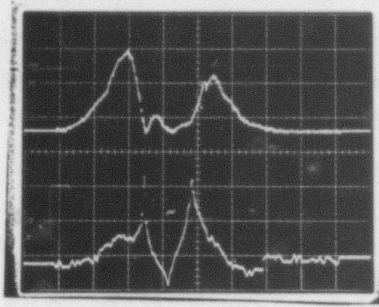
a) DFWM Reflectivity R = 3.9%
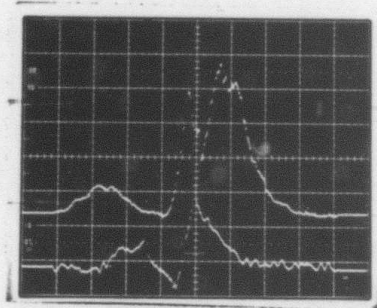
b) DFWM Reflectivity R = 77.9%

Figure 4-4.   Frequency spectra of DFWM reflectivity under lower
              R conditions a). Under low R conditions, the peak
              corresponding to the 2-3 transition is stronger, as
              expected from state degeneracy and oscillator strength
              arguments b). At higher R, the peak corresponding to
              the 1-0 transition becomes larger. On-resonance
              dips in reflectivity (2-3 in Figure 4-4a and 1-0
              in 4-4b) are observed, indicating that the absorptive
              component of the susceptibility, χ'', is still contrib-
              uting to FWM R under these conditions.

α_0, but is still substantial since α_0 was about 200 cm^{-1} in these experiments. At lower sodium densities (and hence lower R) than investigated here, the linear absorption is lower and FWM reflectivity can be observed at these intermediate frequencies (see Reference 4-3). Thus it is the combination of higher nonlinear response off-resonance and the strong linear absorption necessarily present for achieving high reflectivity that accounts for the observed spectral dependence.

A more detailed examination of Figure 4-3 shows that while the reflectivity goes to zero at the 2-3 resonance, there is substantial reflectivity at the 1-0 resonance frequency. Two factors account for this. First, the linear absorption is highest at the 2-3 frequency, remaining higher than that at the 1-0 frequency throughout the wing of the 2-3 transition. A second factor is the relative contributions from the other hyperfine transitions. Consider the FWM response at ω_{10}. The absorptive component of the 1-0 transition is well saturated and its dispersive component is zero. However, at this frequency, the dispersive components of the 1-1 and 1-2 transitions are not zero. The transition moments of the 1-1 and 1-2 transitions are both stronger than the 1-0 and, as discussed in Section 3.2, they can contribute signal if diffusion into the optical field is sufficiently fast to offset the effects of optical pumping. A similar argument holds for response at ω_{23} but the 2-2 and 2-1 transitions are weak in comparison to the 2-3 transition and their contribution is further degraded by the stronger linear absorption.

The role of linear absorption in determining the spectral response is again evident in Figure 4-5, which presents the observed intensity dependence of the FWM reflectivity spectrum. As the pump power increases, the hole between the two reflectivity peaks begins to narrow because of increasing saturation of the linear absorption. The reflectivity peaks broaden mostly towards the center of the D_2 line because that is where the absorption has the strongest effect. Another factor leading to the increased FWM bandwidth is that the homogeneous width increases with intensity. This enlarges the velocity population diamond, increasing the effective number density interacting in the experiment for a given laser frequency. This mechanism also predicts that the broadening is primarily towards linecenter of the D_2 line. Because of the Maxwellian velocity

44
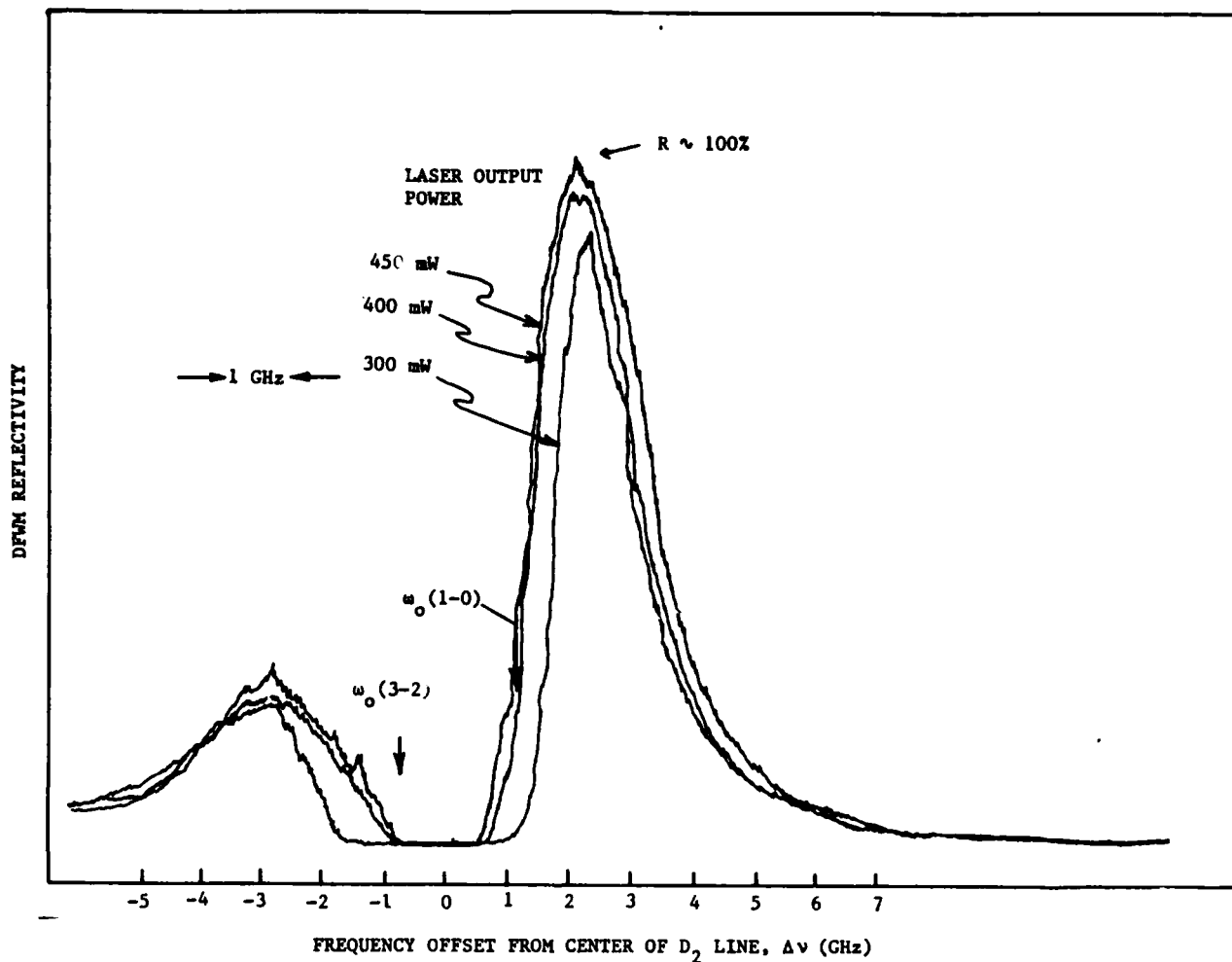
Figure 4-5. Observed dependence of DFWM frequency spectrum as a function of pump power. The spectra were obtained by scanning a narrowband dye laser through the Na D_2 line resonance.

distribution, the number density increases more rapidly on the side of the population diamond that moves towards lower velocity (and hence line center) than on the side moving away towards higher Doppler velocity.

Another interesting feature of the intensity dependence of the FWM reflectivity spectrum can be seen by comparing the spectra in Figures 4-3 and 4-4. There is dramatic change in relative amplitude of the two reflectivity peaks as the pump intensity is increased. Despite the complicated dependence of the DFWM signal on the parameters mentioned at the beginning of this section, transitions originating from the F=2 lower hyperfine level are expected to contribute more to the DFWM signal for two reasons. First, they carry more oscillator strength than those originating from the F=1 lower hyperfine level as can be seen from the values presented in Figure 3-8. Note that the dominant contributing transition from F=2 is the 2-3 transition, which has the strongest transition moment of all, while the dominent transition from F=1 is the 1-0, which has the second smallest transition moment. The saturation intensity is proportional to $1/\mu^2$; the nonlinear $\chi^{(3)}$ term is proportional to μ^4. Secondly, the F=2 hyperfine level has 5/8 of the total ground state population, so there are more absorbers contributing to the signal due to transitions from this level.

Hence the DFWM reflectivity would be expected to be largest on the low frequency side of the broad absorption line shown in Figure 3-9. This is in fact what is observed under the low pump power, low FWM reflectivity conditions ($R \approx 1.6\%$) shown in Figure 4-4a. At even lower powers, the reflectivity due to the F=2 transitions is much larger than that due to the F=1 transitions (References 4-2,4-5).

Under high pump power conditions, the 2-3 peak is observed to be substantially smaller than the 1-0 peak on the high frequency side of the D_2 line. This is illustrated in Figure 4-4b and 4-3 for cases where the FWM reflectivity is approximately 75% and 160%. Such a changeover in the relative magnitude of reflectivity arising from the F=2 and F=1 transitions has been observed in pulsed experiments (Reference 4-6). Peak reflectivity for high pump power CW conditions also has been reported to be near the 1-0 transition rather than the 2-3 transition (Reference 4-7).

This apparent anomaly of the peak reflectivity shifting from the low frequency side of the line, where the contribution to FWM reflectivity

is expected to be largest, to the high frequency side as the pump power is increased arises from another nonlinear effect. This nonlinear interaction involves changes in the propagation characteristics of the intense pump fields induced by spatial intensity variations in the same fields. Two of these self-action effects, self-focusing and self-defocusing, are responsible for the observed intensity effects in the FWM reflectivity spectrum.

In nonlinear media, intensity dependent changes in the material's refractive index cause self-focusing or self-defocusing of propagating laser beams that have nonuniform intensity profiles. The equation describing the nonlinear index change (Δn) for Gaussian laser beams propagating in resonant media is:

$$\Delta n = \frac{-\pi N |\mu|^4 E_o^2}{[\hbar(\omega_o - \omega_L)]^3} \tag{4-1}$$

where μ is the transition dipole moment, N is the (atomic) number density, ω_L is the laser frequency and ω_o is the transition frequency and E_o is the electric field amplitude. It can be seen from this equation that when the laser is tuned to a frequency above the transition frequency, $\Delta n > 0$. This corresponds to a positive lens and the nonlinear medium will have a tendency to focus the laser beam. For laser frequencies below the transition frequency $\Delta n < 0$ and the nonlinear medium will act as a negative lens, tending to defocus the propagating laser beams. Furthermore, it has been shown (Reference 4-8) that the minimum power for self-focusing to affect a Gaussian laser beam is given by:

$$P_{sf} = \frac{3.174 \times 10^{-3} \lambda_o^2 c}{n_2} \tag{4-2}$$

where λ_o is the vacuum wavelength of the laser, c is the speed of light, and $n_2 = 2\Delta n/|E_o|^2$. P_{sf} is on the order of 100 μW for the conditions in the experiments presented here.

The DFWM pump powers employed in TRW's experiments were in the range of 100-600 mW, so self-focusing (self-defocusing) is expected to impact the observed spectral behavior. The 1-0 transition has a larger

47

reflectivity than expected which grows relative to the 2-3 reflectivity peak as I increases because self-focusing increases the effective pump intensity and hence DFWM reflectivity at this frequency. Conversely, the 2-3 transition has a smaller reflectivity than expected because the self-defocusing on the low frequency side of 2-3 transition decreases the pump intensity. Note that self-defocussing is inherently a self-limiting process and so is not expected to play a significant role in determining the FWM reflectivity near the 2-3 transition. Further evidence in support of this explanation comes from both previous observations of self-focusing/self-defocusing in sodium vapor (Reference 4-9) and from observations of greatly increased beam divergences in our experiments. This is discussed in more detail in the next section.

4.3.2 Self-action Effects

The self-action effect of self-focusing and self-defocusing of a single narrowband CW dye laser beam in sodium vapor has been examined previously in detail (Reference 4-9). The purpose of the experiments described here was to characterize the effects of self-focusing and self-defocusing on the DFWM process. These often strong effects include large changes in reflectivity and in the divergences of all laser beams, including the conjugate signal beam. One consequence of the latter is that the phase conjugate fidelity can be degraded at high FWM reflectivity because of the large pump powers. This may limit the conditions under which an atomic vapor phase conjugator may be usefully operated.

Both transmitted pump beams and the conjugate return were observed to have substantially increased divergence in high reflectivity experiments where the sodium density was high and pump intensities were large. An experiment to understand and quantify this effect was performed using the standard counterpropagating pump geometry shown in Figure 4-6. In this particular experiment, care was taken to ensure that the focal points of the two counterpropagating pump beams coincided so that E_f and E_b were phase conjugates at all points along the pump axis. Furthermore, the Na cell was located at this common focal point. The cell length of 1 cm was short compared to the calculated Rayleigh distance of 7.7 cm, so the pump wavefronts had a minimum of curvature in the

48

Figure 4-6. Experimental arrangement for measuring self-action effects under high R conditions in Na vapor. Spot size was measured as a function of distance using a translating iris diaphragm.

interaction region. The signal beam, incident at angle θ_{fs} with respect to the forward pump, was also focused at the center of the cell.

The conjugate return beam diameter was measured as a function of distance from the Na cell and found to be diverging for experiments on both the 2-3 and 1-0 sides of the line. Figure 4-7 presents these data for three different Na densities. Figures 4-7a and 4-7b show results for Na densities where self-action effects were observed, while 4-7c shows observed divergence in the absence of appreciable self-focusing. Geometric constraints prevented measurements closer than about 60 cm from the cell. However, estimated conjugate beam behavior near the Na cell was obtained by fitting the data for Gaussian beam propagation. Two different Gaussian beam profiles are shown in Figure 4-7a for the 1-0 transition data: one that matched beam dimensions at 0 and 100 cm using the measured probe spot with the cell removed, and the other that matched the observed divergence in the 60-100 cm region. Both profiles indicate that the 1-0 conjugate beam is converging as it leaves the Na cell, then diverging. Figures 4-7b and c, in which the lines are Gaussian beams matched to the observed divergences and propagated back to the effective focal points, show that the effective convergence imparted by the Na cell increased as the sodium density was increased. This observation, along with the fact that the 2-3 divergence is essentially the same for all three conditions, suggests that the effect is due to self-focusing.

However, neither of the Gaussian beam profiles accurately matches the conjugate beam propagation characteristics. It is very unlikely that the beam diameter of the probe in the cell is that measured in the absence of sodium vapor because of self-focusing induced by the strong pumps; furthermore the observed beam divergence is not predicted well. The divergence-matched profile requires inordinately large beam diameters in the cell, inconsistent with self-focussing and filamenting of the pump beams. This strongly suggests that the 1-0 conjugate return is not a Gaussian beam, even though the three input waves, E_f, E_b, and E_s, are Gaussian. Such behavior was predicted by Grynberg, et al. (Reference 4-10) who showed that intensity overlap of comparably-sized Gaussian input beams would yield a non-Gaussian conjugate wave because of the intensity dependence of the reflectivity.

Such an effect should also impact the 2-3 conjugate return. It can

50
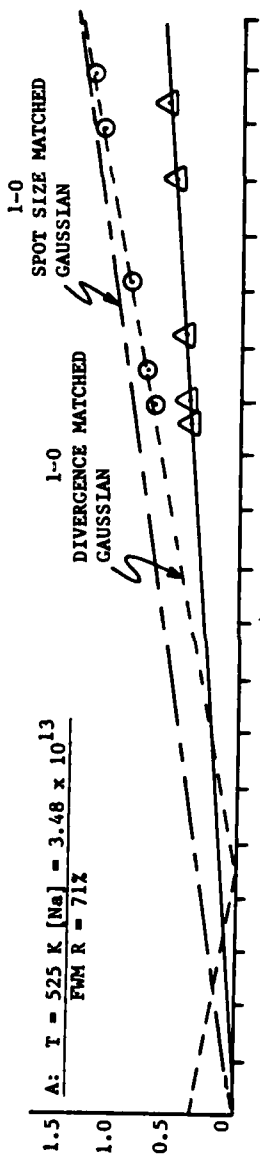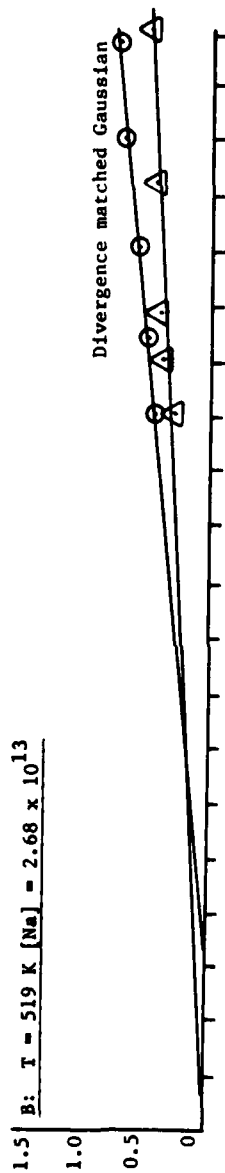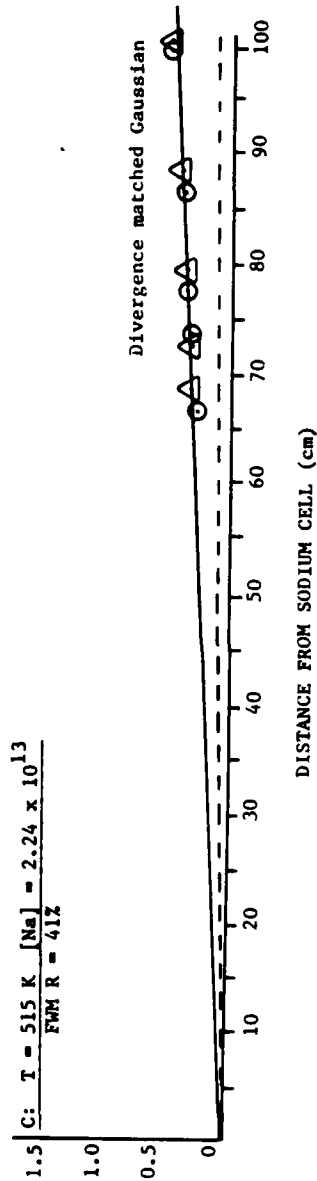
Figure 4-7. Observed conjugate beam radius as a function of distance from the Na FWM cell for three different Na densities. Shown are conjugate returns for the 3-2 and 1-0 transitions, corresponding to the two reflectivity peaks in Figure 4-3.

51

be seen from Figure 4-7c that the divergence of the 2-3 conjugate beam is significantly greater than that of a freely propagating Gaussian input signal beam (dotted line). In these experiments the size of the pump beams was $w_o = 200 \ \mu m$ (radius of 1/e E-field) whereas that of the probe was $w_o = 150 \ \mu m$. For these conditions the average pump intensity experienced by the probe beam varies greatly across the beam. For example, the central 10% of the probe beam will interact with a pump intensity which is ~6 times greater than the pump intensity that the outer 10% ($r = .9 \ w_o$ to $r = w_o$) of the probe beam will interact with. Depending upon the exact experimental conditions, the phase conjugate reflectivity can change appreciably across this aperture due to variations in intensity. For example, for strongly saturating conditions, the outer edge may be reflected more efficiently. Thus when the Gaussian pump and probe beams are comparable in size, the probe beam and the phase conjugate beam will be diffracted in the DFWM process by a gain aperture which is a complicated function of the pump transverse intensity profile.

This effect can alter the effective conjugate spot size in the interaction region, leading to return beams that are not true conjugates of the input signal wave. For the lower sodium number density condition of Figure 4-7c, the aperturing effect appears to be sufficiently dominant to mask the differences in the divergences of the self-focused and self-defocused phase conjugate beams. At higher sodium number densities, the self-action nonlinearity is larger so differences in self-focusing and self-defocusing become evident.

Even stronger lensing effects than those shown in Figure 4-7 have been observed in our experiments at higher pump intensities and sodium number density. These focusing effects have limited our maximum obtainable DFWM reflectivity in sodium vapor. Despite this, we have measured CW DFWM reflectivity of up to 230%, which is about a factor of two larger than previously reported values in the literature. Importantly, these lensing effects were not observed to be significant for reflectivities below 40-50%. Good resolution fidelity and aberration correction was observed in experiments in this lower reflectivity regime. These results are reported in Section 6.

4.3.3 Saturation Effects

The gain aperturing effect mentioned above depends strongly on the saturating effects of the overlapping input beams. Saturating effects were discussed in general in Section 3; this section will examine FWM saturation effects in sodium vapor in the Rabi regime where $2\Gamma < \Delta\omega_{pb} < \Delta\omega_D$. Our high reflectivity measurements were in this experimental regime where saturation characterisitics were neither those of a homogeneous system (Γ or $\Delta_{pb} \gg \Delta_D$) nor those of a system in the Doppler limit ($\Delta\omega_{pb} \ll \Delta\omega_D$).

In homogeneously-broadened absorption lines the saturation intensity increases by a factor of $(1 + \delta^2)$ as the laser is detuned by $\delta = \Delta\omega/\Gamma$ homogeneous half-widths from line center. In contrast, the saturation intensity in the Doppler limit is independent of the detuning of the laser from line center because the laser is on resonance with the one velocity group with which it can interact. Thus $\delta \approx 0$ regardless of the laser detuning from line center where $v=0$ because δ is measured from the Doppler-shifted line center frequency of the resonant velocity group, $\Delta\omega-k\bullet v$, i.e., $\delta = (\Delta\omega-k\bullet v)/\Gamma$ (see Equation 3-14).

Theoretical analysis (Reference 4-11) for homogeneously-broadened lines indicates that maximum reflectivity as a function of pumping intensity (I) occurs $I/I_{sat} \approx 1$. This condition can be met for arbitrarily large I by detuning the laser to increase I_{sat}. The requisite detuning is approximately

$$\delta = [I/I_{sat}(\Delta\omega=0)]^{1/2} \tag{4-3}$$

which matches the condition derived in Section 3.1 for the frequency offset where χ begins to saturate differently if the pumps are significantly stronger than the signal wave. For detunings much smaller than this, $I/I_{sat} \gg 1$ and the nonlinearity has no "contrast" between light and "dark" regions.

Since the absorption line in the Doppler and Rabi regimes is a (Gaussian) distribution of homogeneous absorption lines, each with a slightly different line center frequency, it is useful to consider the relative contribution of each of these homogeneous packets to the total

DFWM reflectivity. Two laser parameters determine this: the laser
frequency, which determines the Doppler shift k•v and the effects of
linear absorption, and the laser intensity, which determines χ as a
function of δ. The contribution of a particular velocity group is then
determined by its population fraction and its value of δ. Note that the
value of δ depends on the homogeneous width over which v is weighted.
In the Doppler limit, v is essentially constant ($-\Delta\omega/k$) over 2Γ; as
the power-broadened homogeneous width approaches $\Delta\omega_D$, $<v>\rightarrow 0$ and
δ becomes $\Delta\omega/\Delta\omega_{pb}$, the value in the homogeneous limit.

The discussion in Section 3.1.2 showed that in the case of DFWM,
the back pump "reads" the nonlinearity off-resonance by 2k•v. As a
result, one would expect the highest reflectivity when $\delta\Gamma$ is equal to
this offset, i.e., the peak reflectivity would be expected at

$$\Delta\omega = 1/2 \ (I/I_{sat}(\Delta\omega=0))^{1/2}\Gamma. \tag{4-4}$$

Measured values of $\Delta\omega$ for the FWM reflectivity peaks on both the 2-3 and
1-0 transitions were 3-4 times larger than predicted from Equation 4-4.
This is expected, however, because Equation 4-4 does not take into account
the impact of residual linear absorption or the effective increase of I on
the 1-0 side of the line due to self-focusing. Both of these effects
should disappear as the Na density is reduced.

4.3.4 Field of View

Figure 4-8 presents the observed dependence of DFWM reflectivity on
θ_{fs}, the angle between the forward pump and signal, under conditions
of high CW reflectivity. The experimental arrangement for making these
measurements was the same as for the active tracking demonstration
described elsewhere. The scanning geometry, reproduced in Figure 4-8, was
chosen to minimize changes in the interaction volume as the angle was
swept. The experiment was also designed to keep any residual phase
mismatch due to misalignment of the pump beams constant as the signal beam
angle was scanned. It is important to minimize the impact of these other
effects that can reduce FWM reflectivity so that the true angular
dependence under high R conditions can be determined.

The angular dependence of the reflectivity can be understood

54

T = 508 K

PUMP INTENSITY: 155 W/cm^2

PROBE POWER: 2.3 mW

$(\sin \theta)^{-2}$ DEPENDENCE

BACK PUMP

θ_{min}

FORWARD PUMP

SIGNAL BEAM

DFWM REFLECTIVITY

8= θ_{min} 10   15   20   25   30

SIGNAL BEAM-FORWARD PUMP ANGLE, θ_{fs} (mrad)
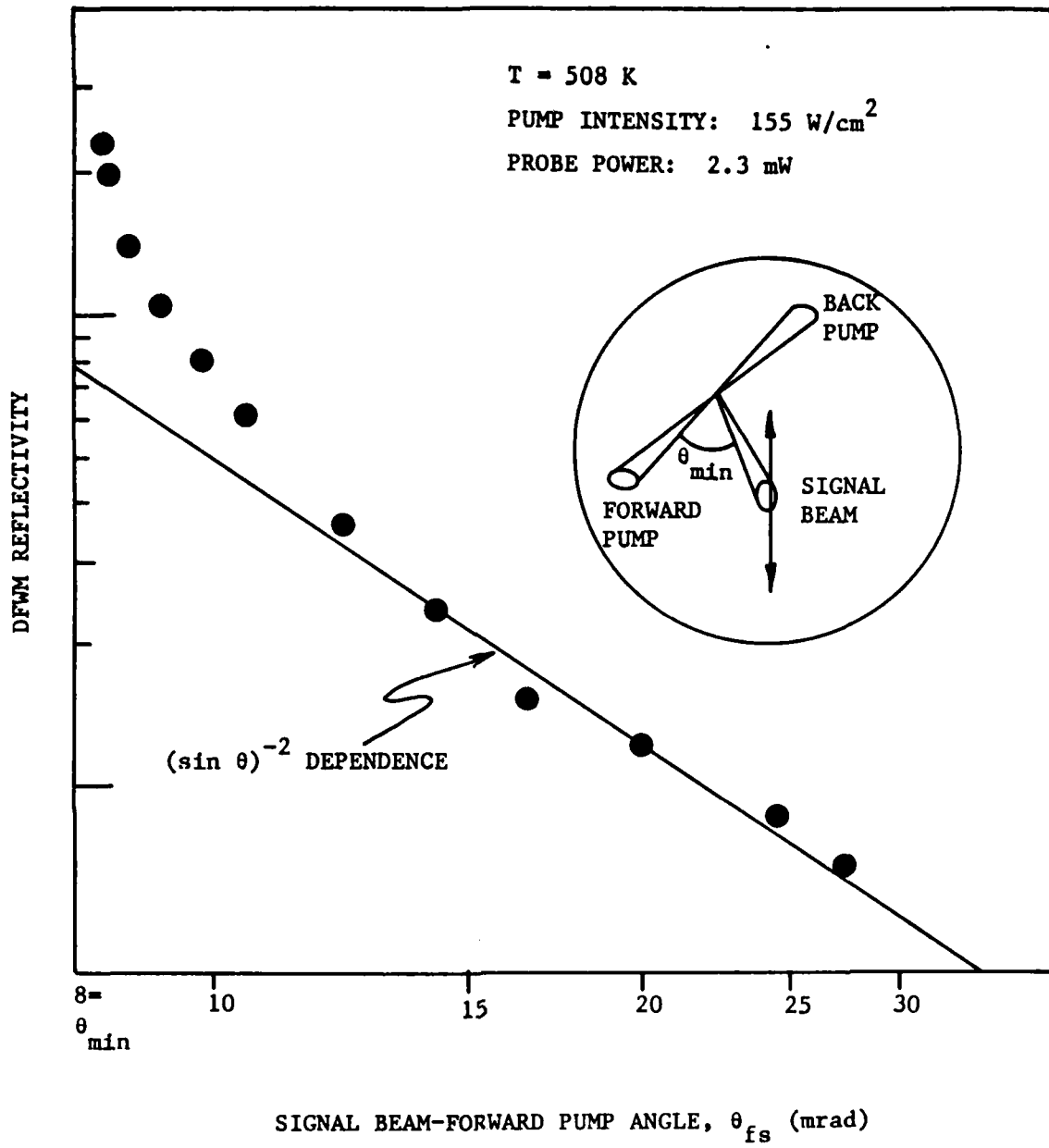
Figure 4-8. Observed angular dependence of DFWM reflectivity under high reflectivity (R > 150%) conditions. Shown is the predicted $\sin^{-2} \theta$ dependence.

qualitatively in terms of the angular dependence of the population of sodium atoms comprising the refractive index grating. When $\theta_{fs}=0$, the population discs (c.f. Figure 3-4) resonant with E_f and E_s coincide, yielding the largest possible sodium atom population for the nonlinear interaction. For large θ_{fs} in the Doppler limit, the velocity is essentially constant over the population diamond, and so the sodium density available for forming the grating is just

$$N_{ex}=N_{tot}(8M/\pi RT)^{\frac{1}{2}}\exp[-M\Delta\omega^2/2RTk^2\cos^2(\theta/2))](\Gamma^2/k^2\sin\theta) \qquad (4\text{-}5)$$

which for $\Delta\omega=0$ varies as $1/\sin\theta$. This is the population fraction that interacts with the optical fields, but because of grating washout it is not the effective population comprising the grating. At most angles, the grating lifetime is determined by washout, which in turn is determined by the grating spacing given in Equation 3-8. Thus the effective N'_{ex} for large θ varies as $(\sin\theta)^{-2}$, and the expected angular dependence of FWM reflectivity varies as $(\sin\theta)^{-4}$ since $R \propto N^2$. This simple derivation, based on the physical model discussed in Section 3, matches the large angle predictions from more complex formulations published by Wandzura (Reference 4-12) and Nilsen and Yariv (Reference 4-13). Equation 4-5 is not valid for the small angles of our data because the population diamond extends over a wide range of velocities perpendicular to E_f and E_s. In this case, N_{ex} is given by

$$N_{ex} = N_{tot}(M/2\pi RT)\int_{\Delta\omega-\Gamma/k}^{\Delta\omega+\Gamma/k}\int_{v_L}^{v_L+2\Gamma/k\sin\theta}\exp^{[-M(v_x^2+v_y^2)/2RT]}dv_y dv_x \qquad (4\text{-}6)$$

where

$$v_L = \{(\Delta\omega-\Gamma)/k\}\tan(\theta/2) - \{v_x-(\Delta\omega-\Gamma)/k\}\cot\theta$$

Note that Γ should be replaced by $1/2\Delta\omega_{pb}$ if power-broadening is contributing to the homogeneous width. N_{ex} calculated from Equation 4-6 must still be reduced by the effect of grating washout. The washout

effect is also reduced substantially because the grating spacing is increased and because the grating lifetime can now be controlled by the radiative lifetime of the excited state. In sodium, radiative decay (upper state lifetime $\tau = 16$ ns) is a stronger grating loss mechanism than grating washout for angles smaller than about 50 mrad; the grating steady state population is determined primarily by radiative lifetime for angles less than about 15 mrad.

The above model would predict that reflectivity in homogeneously broadened lines would fall off as $(\sin \theta)^{-2}$ due only to grating washout because there would be no angular dependence to the participating population, N_{ex}. Calculations using Equation 4-6 would indicate that similar behavior would be expected in the experiment reported here because $dN_{ex}/d\theta$ is essentially zero if $\theta \leq \Delta\omega_{pb}/\Delta\omega_D$, the ratio of the power-broadened homogeneous width to the inhomogeneous width. This conclusion is supported by the numerical computation of Nilsen and Yariv, presented as Figure 4-9, which shows an approximate $(\sin \theta)^{-2}$ dependence for angles in our data range. This calculation, while generic, does fit closely parameters for sodium at temperature used in our experiments. It clearly shows the decreasing importance of grating washout at small angles as the grating spacing increases and radiative processes begin to control the grating lifetime and steady-state population. It also begins to show the effects of nonzero $dN_{ex}/d\theta$ at the larger angles, where the calculation begins to fall off faster than $(\sin \theta)^{-2}$.

Our experiments were performed in the Rabi regime, so the pertinent homogeneous width was $\Delta\omega_{pb}$, which was typically $0.2\Delta\omega_D$. Thus the observed $(\sin \theta)^{-2}$ for angles larger than ≈ 15 mrad is as expected. For smaller angles, the reflectivity is observed to exhibit a stronger angular dependence rather than rolling off as grating washout becomes unimportant. This may be an experimental artifact arising from changes in the effective interaction volume defined by the overlap of Gaussian signal and pump beams, or may be due to residual pump misalignment giving rise to an angular phase mismatch. It can be easily shown that even with pump misalignment, the phase mismatch in a DFWM experiment goes to zero when E_f and E_s are colinear. The impact on an experimental measurément depends on the acceptance angle of the conjugate beam detector.

57
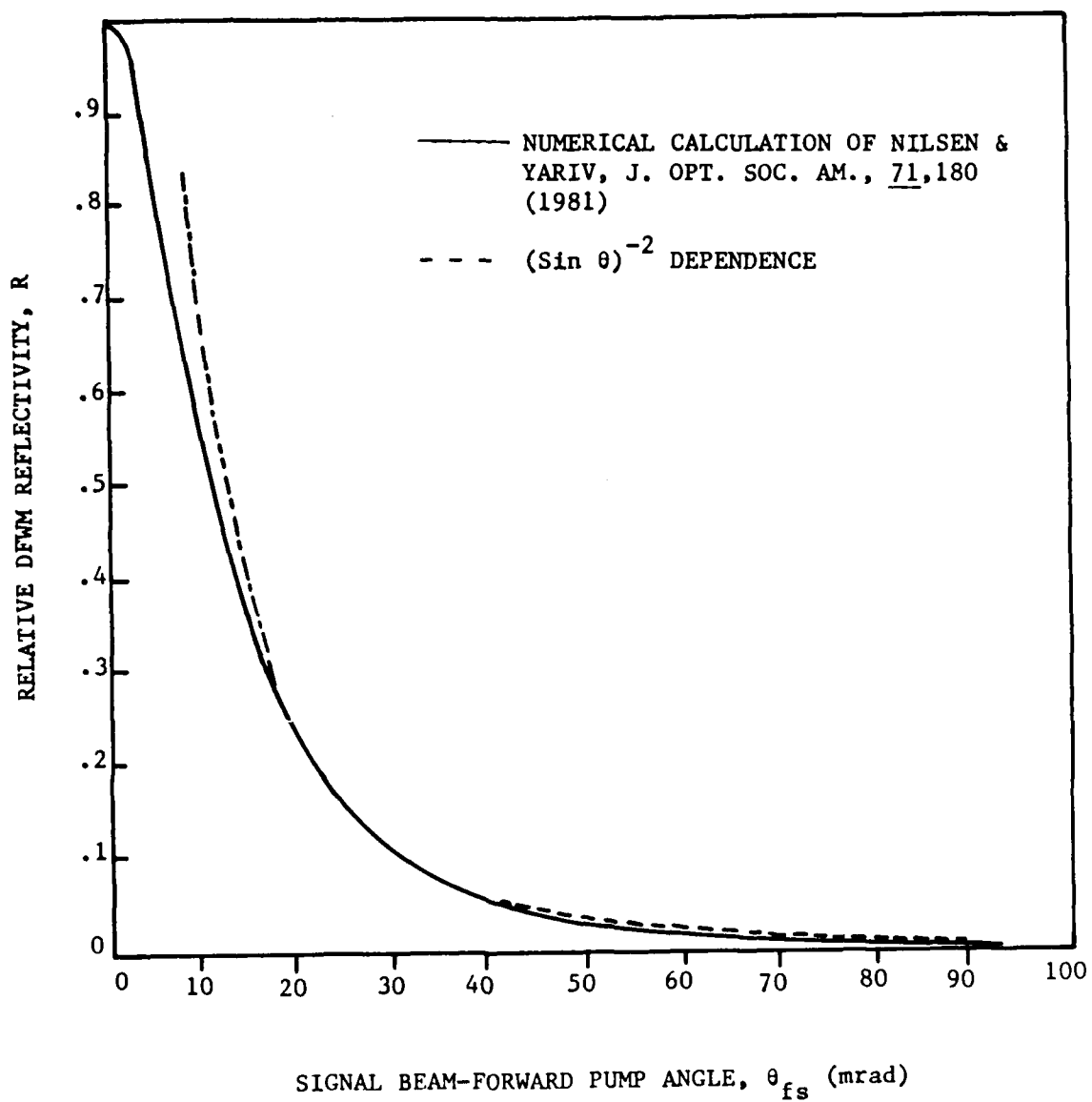
Figure 4-9. Predicted $\sin^{-2} \theta$ dependence compared to numerical calculation of FWM reflectivity in the Doppler limit. The numerical calculation follows predicted behavior at small angles.

The simple model presented above must be considered in more detail in light of the discussion of saturation and off-resonance contributions (Section 3.1.1 and 4.3.3), as well as the effect of optical pumping when there is strong overlap of neighboring hyperfine transitions (Section 3.1.2). These effects are important in our experiments and will substantially alter the velocity distributions that must be integrated over in Equation 4-6. Optical pumping modification of the velocity profile has been considered by Humphrey, et al. (Reference 4-5), whose theoretical treatment shows that optical pumping can account for the (sin θ)$^{-2}$ dependence they observed for angles up to 1 rad in a low-power, Doppler-limit experiment. However, those experiments were performed using a magnetic field to split the magnetic sub-level degeneracies; in the absence of the field they report a (sin θ)$^{-4}$ dependence at these large angles. This change in angular dependence with the application of a magnetic field of a few Gauss was unexplained.

The above model, in conjunction with Equations 3-9, 3-11, 3-12, and 4-6, can be used to estimate the angular dependence of R for different values of I and $\Delta\omega$, once the effects of optical pumping and strong saturation have been considered. A few basic observations can be made, however, concerning the field-of-view in the high reflectivity regime of our experiments. First, large $\Delta\omega$ is necessary, which effectively eliminates the contribution of the back grating formed by E_b and E_s. Under low power, on-resonance conditions, this grating becomes increasingly important as θ_{fs} increases, mitigating the loss of reflectivity from the forward grating. Secondly, the increased homogeneous width due to power-broadening leads to increased N_{ex} and larger θ before $dN_{ex}/d\theta$ becomes important, but also leads to more rapid grating decay because the average cross-grating velocity, $<v_{gd}>$, is increased (see Equation 3-9 and accompanying discussion). For small θ, $<v_{gd}> \approx v_{thermal}$ independent of Γ (or $\Delta\omega_{pb}$) so one would expect that the field of view would increase with Γ, as predicted by Nilsen and Yariv. However, strong overlap of the hyperfine components coupled with optical pumping (c.f. Figure 3-10b) can effectively reduce N_{ex} and increase angular sensitivity at the higher intensities required for good FWM reflectivity.

59

4.4 BROADBAND REFLECTIVITY

The reflectivity experiments described so far were performed with a laser bandwidth of $\approx$ 1 MHz, narrow compared to any of the characteristic frequencies of the sodium medium. Such a source bandwidth is not easily achieved under laboratory conditions; a requirement for such a bandwidth would have significant impact on the practicality of fielding a sodium vapor FWM for mission applications. To ascertain the effects of wider source bandwidths, FWM reflectivity was measured using the broadest bandwidth available from our laser source.

The ring dye laser when operated in the broadband configuration has a frequency bandwidth of 2 GHz consisting of a number of longitudinal loop modes spaced by ~90 MHz. The coherence length of 15 cm was long compared to the interaction lengths in our experiments so the modes were mutually coherent. Even though the broadband laser power (1.25W) is greater than the narrowband power (800 mW), the broadband power is distributed over ~22 longitudinal modes, resulting in a power per mode that is ~14 times less than for single frequency operation. Changes in the output beam diameter result in an intensity ~20 times lower per optical mode. The experimental setup was the same as for the narrowband reflectivity measurement, except that meaningful frequency measurements of the broadband laser were not possible because of inherently unstable operation of the laser. Because of this instability, it was not possible to measure the spectral dependence of broadband reflectivity.

Surprisingly high reflectivity was observed. Reflectivity was measured to be ~15-20% in a 3 cm cell containing sodium in a 1 torr buffer of Ar. A 6% reflectivity was measured in a 1 cm cell with no added buffer gas. To first order, $R \propto L^2$ so the reflectivity in the 3 cm cell appears to be diminished by the buffer gas; such a result is consistent with our observations in narrowband experiments and the results of other workers (Reference 4-7). An interesting and unexplained phenomenon was that the best reflectivity in the case of the 3 cm cell was observed to occur when the two counterpropagating pump beams were deliberately misaligned. These results can be explained qualitatively in terms of the differences in broadband and narrowband dye laser operation. These

differences affect relative contributions to the DFWM signal by various velocity groups of the Doppler-broadened absorption line.

One of the main differences between broadband and narrowband DFWM is that the level of saturation per optical mode will be smaller for broadband operation by a factor of ~20. Since the pump intensity/saturation dependence of the DFWM signal (Section 4.3.1) can be quite strong, it would be expected that the broadband reflectivity will be much less than the narrowband reflectivity. I/I_{sat} for each of the broadband modes is a factor of 20 less than the narrowband single mode I/I_{sat}, but there are ~22 of these broadband modes. These two factors do not cancel one another, however, because the FWM signal is proportional to the square of the polarization and the sum of the squares of each of the 22 broadband polarization components (which assumes mutual coherence among the modes) will be less than the square of the single (large) narrowband polarization component. For the numbers in our experiments, this simplistic argument would indicate that the broadband reflectivity would be about 6% of the narrowband reflectivity, remarkably within a factor of two of the observed ratio of about 3% (6%/230%) under high reflectivity conditions in the 1 cm cell. Stronger self-focussing in the narrowband experiments could account for this difference. A more complete analysis would require incorporating the effects of a nonuniform distribution of optical energy over the longitudinal modes and consideration of saturation effects. These considerations would require detailed information on the actual frequency spectrum of the laser line with respect to the Doppler-broadened D_2 line before a more careful comparison between broadband and narrowband reflectivities can be made. We were not able to collect this information with our present experimental configuration.

Another consequence of the broadband power distribution is that contributions to the signal will now be possible from non-degenerate four-wave mixing (NDFM) processes. Because of the range of optical frequencies, ω_L, the resonance conditions described by Equations 3-3 and 3-4 in Section 3.1.2 can be satisfied over a wide range of velocities for both the forward and backward gratings. The nearly co-linear E_f and E_s beams interact with the same sodium velocity group to write an efficient refractive index grating at a detuning $\Delta\omega$ from the Doppler-line center. For very small θ, these two fields will generally

correspond to the same longitudinal optical mode in both the signal and forward pump fields because they must be within a homogeneous width of each other to write the interference grating. For our experiments, the power broadening under broadband conditions was such that only one or two modes could interact to form a grating. (This limitation in the number of modes writing the grating holds at larger angles also, but the mode may not be the same in the signal and forward pump fields because they experience different Doppler shifts. This "mode-hop", where it is the n+1 mode of the signal field writing a grating with the nth mode of the forward pump, occurs at such large angles in our experiments that such interactions do not need to be considered here.)

Unlike the case of DFWM discussed in Section 3.1.2, there are now many optical modes in E_b for reading out the forward grating. Consider a case where the homogeneous width allows interaction of only one optical mode from each field with a particular velocity group. At small angles when the grating is written by the same optical mode ω_n in E_f and E_s, a phase-matched DFWM experiment occurs for the ω_n mode in E_b. This mode sees the nonlinearity Doppler-shifted by $2(\omega_n-\omega_0)$. All other modes in E_b participate in NDFWM experiments. Figure 4-10 shows that these NDFWM interactions are also phase matched if $\theta_{fs}=0$. For nonzero θ_{fs}, the phase mismatch for mode $\omega_n \pm \xi$ ($\xi \ll \omega_n$) is

$$\Delta k \approx (\xi/c)[(1-\cos\theta_m)/\cos\theta_m] \qquad (4\text{-}7)$$

where $\theta_m=$ arcsin $\{\omega_n\sin\theta_{fs}/(\omega_n+\xi)\} \approx \theta_{fs}$, and ξ is the frequency difference of the two modes in the NDFWM experiment. In our experiments, the maximum value of ξ is $2\pi(2 \text{ GHz})$, which for a θ_{fs} of 8 mrad, results in excellent phase matching for all modes over the 1 cm inter-action length. Thus all modes in E_b are backscattered in phase-matched FWM experiments. The efficiency for a particular mode, $E_{b,i}$, is deter-mined by how much off resonance it reads the χ grating generated by E_f and E_s at ω_n, the linear absorption at ω_i, and the effects of contrast and saturation discussed in Section 3.1. For example, given that E_f and E_s are detuned by $\Delta\omega$, the back pump mode at $\omega_n-2\Delta\omega$ reads the χ grating on resonance, but because of the lineshape of the D_2 line tends to be strongly absorbed.

62

ENERGY CONSERVATION REQUIREMENT: $\omega_f + \omega_b - \omega_s = \omega_c$

PHASE MATCHING REQUIREMENT: $\vec{k}_f + \vec{k}_b - \vec{k}_s = \vec{k}_c$

$\theta_{fs} = 0$

$\vec{k}_f = \left(\frac{\omega_n}{c}\right)\hat{x}$

$\vec{k}_b = -\left(\frac{\omega_n - \zeta}{c}\right)\hat{x}$

$\Delta\vec{k}_{pump} = \vec{k}_1 + \vec{k}_2 = (\zeta/c)\hat{x}$

$\vec{k}_s = (\omega_n/c)\hat{x}$

$\vec{k}_1 + \vec{k}_2 - \vec{k}_s = -\left(\frac{\omega_n - \zeta}{c}\right)\hat{x}$

$= \vec{k}_c$
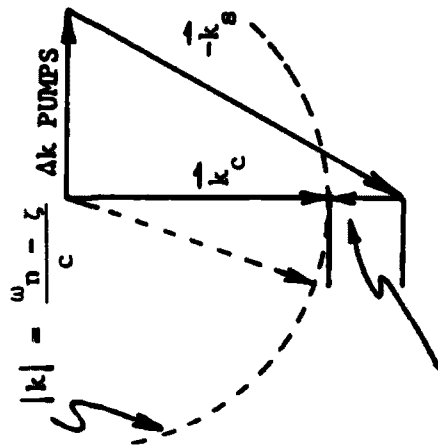
PHASE MATCHED FOR ANY MODE $\omega_n \pm \zeta$ IN BACK PUMP

$\theta_{fs} \neq 0$

LOCUS OF POINTS WITH $|k| = \frac{\omega_n - \zeta}{c}$

Δk PUMPS

$-\vec{k}_s$

$\vec{k}_c$

MINIMUM RESIDUAL PHASE MISMATCH DETERMINES MAGNITUDE AND ANGULAR OFFSET OF CONJUGATE FROM INCOMING SIGNAL BEAM

Figure 4-10. Frequency and phase-matching conditions in NDFWM experiments occuring during broadband laser pumping. The experiments are strictly phase matched only for $\theta_{fs} = 0$, but the mismatch at $\theta_{fs} \neq 0$ is negligible for the 2 GHz bandwidth used in these experiments.

63

At large angles where "mode-hop" has occurred, the signal now arises purely from NDFWM interactions. Letting mode ω_n be that of E_f, and considering E_s to be mode ω_{n+1}, a conjugate beam at ω_{n-1} will be formed by scattering of the ω_n (back pump) mode in E_b. The appropriate shift in conjugate wave frequency about ω_n is a result of the Doppler shift from the E_f/E_s grating, which in this nondegeneate experiment is produced by the traveling interference wave at $\omega_f(-\omega_n)-\omega_s(-\omega_{n-1})$. Phase matching arguments are essentially the same as those presented above. Efficiency considerations are similar to the case where the same mode in E_f and E_s interact, except that the finite response time of sodium becomes important when nondegenerate fields write the gratings. The time dependence of the traveling grating must be slow compared to the response time of sodium, i.e., $|\omega_f-\omega_s| < 1/T_1$ (or the Rabi frequency), otherwise the grating contrast will become blurred.

An important difference between high reflectivity experiments using narrowband and broadband sources is the contribution of gratings formed by signal and back pump fields (the "back" grating). The discussion in Section 3.1.2 and Figure 3-5 indicate that back gratings are not important in narrowband DFWM experiments. This is not the case in broadband experiments, where mode ω_n in the signal field can interact with the same velocity group as mode $\omega_n-2\Delta\omega$ in the back pump, producing a grating that is well within $v_{thermal}$. Such gratings are "read" by all modes in E_f, and are inherently NDFWM interactions. Efficiency arguments are similar to those presented above, with some modifications. First, because of the finite response time of sodium, the traveling grating written by E_s (ω_n) and E_b ($\omega_n-2\Delta\omega$) will smear unless $2\Delta\omega < 1/T_1$. Thus only one or two modes near ω_0 can result in important back gratings. These few back gratings are still "read" by all modes in E_f, with phase mismatches that are negligible in our experiments.

If sufficient overlap of the laser line with the sodium absorption line exists so that $\Delta\omega$ approaches zero, back gratings and their NDFWM contribution will be important in broadband experiments. An example is field-of-view. The back grating has its minimum spacing at $\theta_{fs}\approx 0$, where the ravages of thermal washout minimize its contribution to the FWM

64

reflectivity. As θ_{fs} is increased, the back grating contribution to FWM reflectivity increases, offsetting the loss of reflectivity from the forward grating. Thus one would expect a larger field-of-view for broadband operation. Experimental observation of this is presented in Figure 4-11, which shows the angular dependence of broadband reflectivity compared to that of normalized narrowband reflectivity.

4.5 ACTIVE TRACKING DEMONSTRATION

An active tracking demonstration was performed to show the automatic tracking capabilities of a phase-conjugating FWM. Figure 4-12 shows the experimental setup, which consisted of the standard counterpropagating pump beam geometry, except that the back pump was generated by a retroreflecting mirror. The signal beam, which essentially constituted a very bright glint, was split off of the pump leg by a beamsplitter and directed to a galvometrically scanned rotating mirror (RM) located at the radius of curvature of a spherical mirror (SM). The sodium cell FWM was also located at the radius of curvature of the spherical mirror and placed such that the cell and the rotating mirror were on opposite sides and equally spaced from the optical axis of the spherical mirror. This arrangement permitted a substantial angular sweep of the incoming signal beam over the surface of the spherical mirror while maintaining approximately the same interaction length in the sodium cell. The conjugate return reflected off of the spherical and rotating mirrors and was separated from the incoming signal beam by a beam splitter. The conjugate was monitored by passing it through an aperture to measure diviation from the signal path, and displayed on a white card. If the FWM cell provided accurate automatic tracking, the conjugate beam would retrace the signal beam path precisely, and since the rotating mirror was essentially stationary on the timescale of the optical roundtrip from it to the sodium cell, the conjugate beam would pass through the aperture and be visible on the display card.

Automatic tracking of the input signal beam was observed for angular scans of 50 mrad, a limitation imposed by the size of the spherical mirror. The rotating mirror was driven at 1000 Hz, providing an angular scan rate in excess of 100 radians/s. Under all conditions, the conjugate
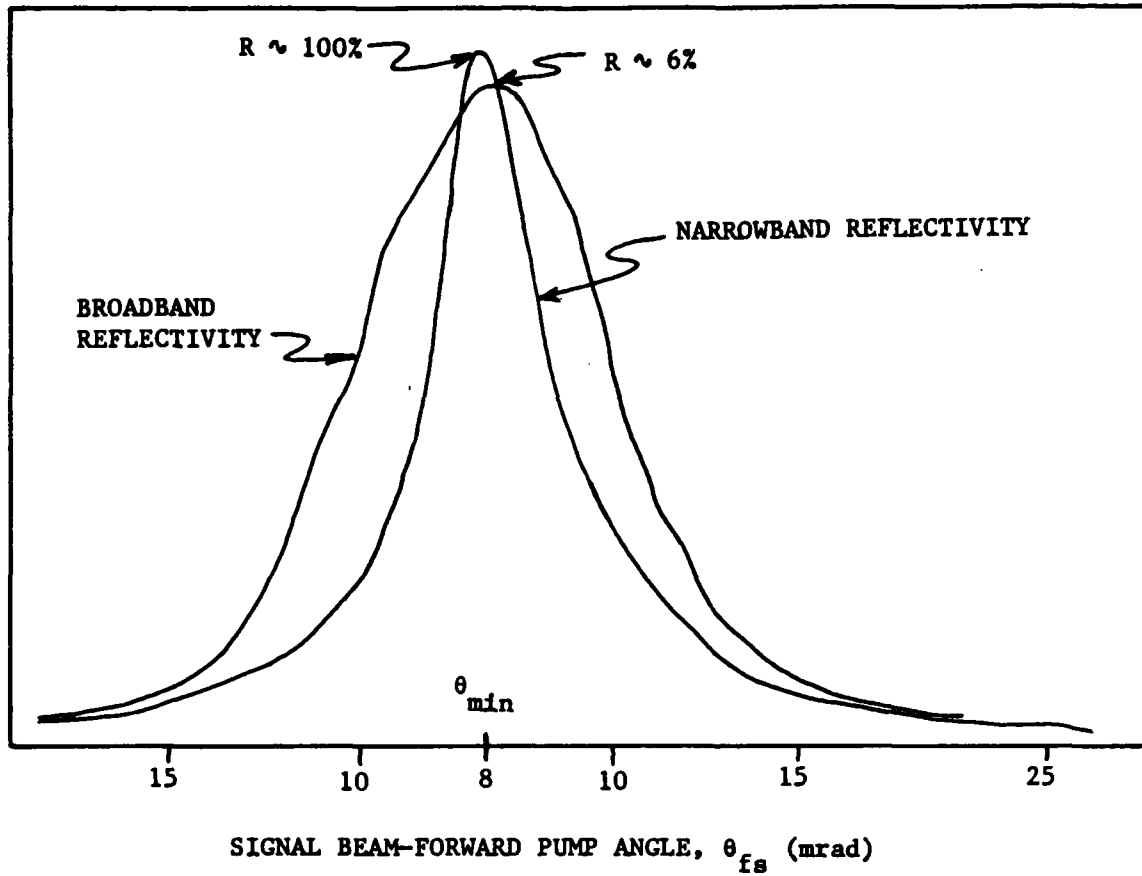
Figure 4-11. Observed angular dependence of DFWM reflectivity using broadband (2 GHz) laser irradiation. Data was collected in the same manner as narrowband reflectivity (also shown), except that data was recorded photographically to overcome frequency instability of laser during broadband operation.
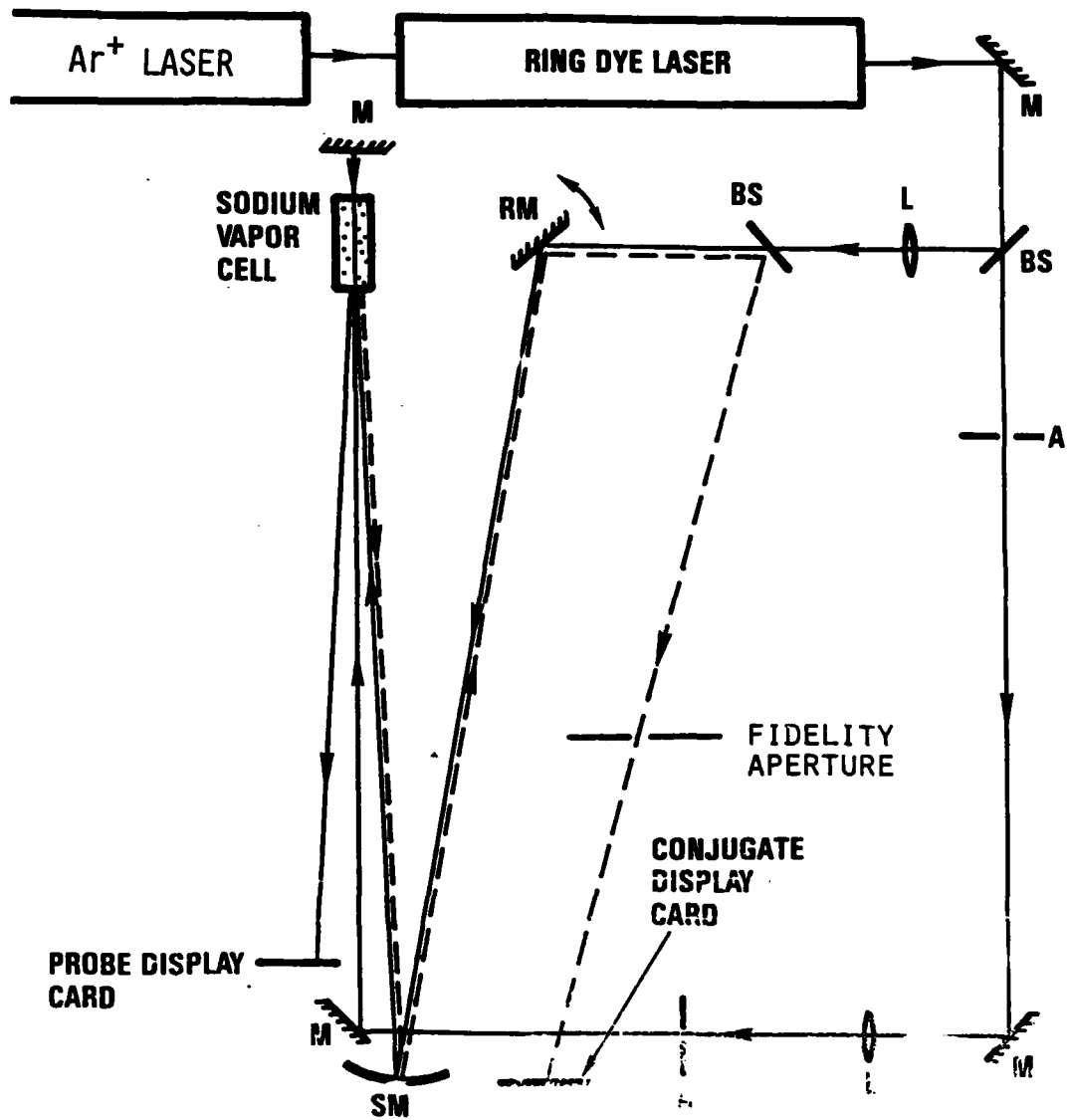
Figure 4-12: Experimental setup for the active-tracking demonstration and field-of-view measurements.

return was observed to pass through the aperture. Angular deviation was less than 1 μrad, which was the precision of our measurement. This experiment demonstrates that while FWM reflectivity drops off very rapidly in sodium vapor, the effective field-of-view for automatic tracking can be substantially larger if the FWM reflectivity is adequate.

4.6 REFERENCES

4-1   T. W. Hansch, M. D. Levenson, A. L. Schalow, Phys. Rev. Lett. 26, 946 (1971).

4-2   D. G. Steel and R. A. McFarlane, Phys. Rev. A27, 1687 (1983); ibid, Phys. Rev. A27, 1217 (1983).

4-3   J. P. Woerdmann and M. F. H. Schuurmans, Opt. Lett. 6, 239 (1981).

4-4   P. F. Liao, D. M. Bloom, N. P. Economou, Appl. Phys. Lett. 32, 813 (1978).

4-5   L. M. Humphrey, J. P. Gordon, P. F. Liao, Opt. Lett. 5, 56 (1980).

4-6   P. Kumar, Opt. Lett. 10, 74 (1985).

4-7   D. G. Steel and R. C. Lind, Opt. Lett. 6, 587 (1981).

4-8   E. L. Dawes and J. H. Marburger, Phys. Rev. 179, 862 (1969).

4-9   J. E. Bjorkholm and A. Askin, Phys. Rev. Lett. 32, 129 (1974).

4-10 G. Grynberg, B. Kleinmann, M. Pinard, Opt. Comm. 47, 291 (1983).

4-11 R. C. Lind, D. G. Steel, G. J. Dunning, Opt. Eng. 21, 190 (1982).

4-12 S. M. Wandzura, Opt. Lett. 4, 208 (1979).

4-13 J. Nilsen and A. Yariv, J. Opt. Soc. Am. 71, 180 (1981).

5.0 CROSSTALK ANALYSIS AND EXPERIMENTS

Crosstalk between a phase conjugate wave and noise waves was investigated experimentally to evaluate detectivity limits intrinsic to the FWM process. Crosstalk was observed, but only under high probe/noise conditions where pump depletion occurs. These measurements, which fully satisfy the contract SOW, thus show that crosstalk is insignificant under the weak probe conditions likely to be encountered in phase conjugated optical links. It was determined that analysis of FWM physics beyond that required by the SOW was desireable, however, so a theoretical evaluation of crosstalk was undertaken on TRW IR&D. This evaluation is included because it substantiates our experimental conclusions.

5.1 OBJECTIVES AND BACKGROUND

The detectivity of a signal on a phase conjugate wave can be limited by crosstalk between the phase conjugate wave and one or more noise waves in the FWM cell. In this section we shall examine

a. intensity crosstalk, i.e., unwanted temporal intensity variations, and

b. phase crosstalk, i.e., unwanted effects of a noise wave's transverse phase distribution.

In Section 6, spatial crosstalk, i.e., unwanted transverse intensity patterns, is examined and shown to derive from the intensity crosstalk mechanisms identified in this section.

We start with a survey of possible crosstalk mechanisms such as pump depletion, probe depletion, etc., as well as some observations about what might be expected in the Na vapor experiments to be discussed next. For each experiment there is a description of its design, followed by a presentation of the results and conclusions.

It will be seen that, for combined probe-noise beam intensities that are low to moderate compared to the total pump intensity, the crosstalk appears to be due principally to a combination of pump depletion and intensity saturation of the FWM interaction. At higher probe-noise intensities, there is evidence of contributions from other mechanisms. An

empirical expression that fits the data on probe reflectivity vs. probe intensity can be used to predict the intensity crosstalk for arbitrary probe/noise intensity ratios. It will be shown experimentally that the predictions are quite accurate. This same expression will be used to predict the tolerable noise intensity (or, conversely the necessary probe intensity) in a system for communicating via intensity modulation.

5.2 CROSSTALK MECHANISMS

To describe FWM, we start with Maxwell's equations and eliminate the $\vec{B}$ field to obtain the wave equation for the electric field. If all electric fields are copolarized the result in cgs units is

$$\nabla^2 E - \frac{\epsilon}{c^2} \frac{\partial^2 E}{\partial t^2} - \frac{4\pi}{c^2} \frac{\partial^2 P_{NL}}{\partial t^2},$$

where P_{NL} is the nonlinear part of the induced polarization. There are at least four waves present (the two pumps, the probe and the probe conjugate), so we make this explicit by writing

$$E - \Sigma_m E_m.$$

In the slowly varying wave approximation, the expression for each field is

$$E_m - 1/2 \, \tilde{E}_m(\vec{r},t) \, \exp[i(\vec{k}_m \cdot \vec{r} - \omega_m t)] + c.c.,$$

where c.c. is the complex conjugate and $E_m(\vec{r},t)$ is assumed to vary slowly with respect to $\vec{r}$ and t compared with the rapid variation of the exponential. For FWM in a Kerr-like medium, the nonlinear polarization has the form

$$P_{NL} - \chi^{(3)} E^3,$$

where $\chi^{(3)}$ is the third order susceptibility. In steady state, the slowly varying envelope approximation to the wave equation is

$$\frac{d\tilde{E}_m(\vec{r})}{dz} - \frac{i\pi\omega_m}{2nc} \chi^{(3)} \quad \tilde{E}_j(\vec{r})\tilde{E}_k(\vec{r})\tilde{E}_l^*(\vec{r}) \, \exp[i(\vec{K}-\vec{k}_m)\cdot\vec{r}] \tag{5-1a}$$

where $\omega_j + \omega_k - \omega_l - \omega_m,$ \hfill (5-1b)

and $\vec{K} - \vec{k}_j + \vec{k}_k - \vec{k}_l,$ \hfill (5-1c)

and where the z-axis is parallel to $\vec{k}_m$. Strictly speaking, all combina-

tions $\tilde{E}_j$, $\tilde{E}_k$, and $\tilde{E}_l$, which are any three of the waves composing the total field, must be included as source terms on the right hand side of Eqn. 5-1a, but very few of the possible triplets make significant contributions.[1] Unless $\vec{k}_m$ is very close to $\vec{K}$, the rapidly varying exponential causes E_m to be very small. Thus $\vec{k}_m$ must be parallel to $\vec{K}$, and we must have $|\vec{K}| \approx \omega_m/nc$, ie., there must be very little phase mismatch. For degenerate FWM, $\omega_m - \omega$, the input frequency, for all m.

Eqn. 5-1a shows that the element of wave $dE_m(\vec{r})$ created in the interval dz is proportional to the three contributing waves, E_j, E_k, and E_l. Furthermore, at any point (x,y) in the plane normal to the z-axis, $dE_m(x,y,z)$ is proportional to the magnitudes of these three waves at that point. This behavior will be important in the understanding of transverse spatial crosstalk.

Eqn. 5-1a also says that any trio of existing waves, E_j, E_k, E_l, whose new wave vector $|\vec{K}| \approx \omega/nc$, may give rise to a new wave; if $\vec{K}$ is equal to the wave vector of an existing wave, then dE_m will be an increment to that wave. The crosstalk experiments were done near absorption resonances in Na vapor, so the medium was not Kerr-like. Instead the susceptibility is intensity dependent and the induced polarization at any point vanishes as the total intensity at that point becomes arbitrarily large (Ref. 5-1, 5-2, 5-3 and discussion in Section 3.1). Consequently, the fields radiated by the oscillating polarization decrease for sufficiently large input intensity. This is reflected in the replacement of the constant $(i\pi\omega/2nc)\chi^{(3)}$ in Eqn. 5-1 by $W_{jkl}(I)$, a function of the total intensity in the interaction region. $W_{jkl}(I)$ decreases for very large total intensity. This saturation behavior will later be seen to be a significant factor contributing to crosstalk.

The FWM generation of the probe-conjugate wave E_{pc}, and the amplification of the transmitted probe E_p are described by

$$dE_{pc} - W_{fbp}(I) \; E_f E_b E_p^* \; dz \tag{5-2a}$$

and

$$dE_p - W_{fbpc}(I) \; E_f E_b E_{pc}^* \; dz \tag{5-2b}$$

---

[1]To simplify the notation, $\tilde{E}$ will be represented as E from here on.

where E_f and E_b are the forward and backward pump waves. Now we can anticipate that if the total intensity I is already in the saturation regime, then a noise wave, strong enough to significantly increase I, will decrease the probe-conjugate intensity, i.e., it will cause crosstalk.

Terms describing absorption or gain should be included in Eqn. 5-2: they are ignored here because we are primarily interested in terms that create new waves. Also ignored are focusing terms that are proportional to coupling triplets of the form $(E_f E_f^*)E_p$, $(E_f E_f^*)E_{pc}$, $(E_b E_b^*)E_p$, and $(E_b E_b^*)E_{pc}$.

5.2.1 Intensity Crosstalk

First we consider FWM waves that are generated in the absence of noise beams. Two waves, $dE_1 \sim E_p E_b E_f^*$ with wave vector $\vec{k}_p - 2\vec{k}_f$ and its conjugate $dE_{1c} \sim E_{pc} E_f E_b^*$ with wave vector $2\vec{k}_f - \vec{k}_p$, are created with strong coupling since each triplet contains two strong pump waves. There is, however, some phase mismatch because our probe beam was at an angle of the order of 10 mrad from the pump beams, so that the above wave vector magnitudes were not exactly equal to ω/nc. Thus the intensities of these waves are expected to be considerably smaller than those of the probe and probe-conjugate.

Other weaker waves, created by triplets with only one strong pump term, are $dE_2 \sim E_p E_b E_{pc}^*$ with wave vector $2\vec{k}_p - \vec{k}_f$ and its quasi-conjugate[2] $dE_{2c} \sim E_{pc} E_f E_p^*$ (wave vector: $\vec{k}_f - 2\vec{k}_p$); again there is an angular phase mismatch. These two now give rise to a two-step infinite series of waves and quasi-conjugates:

Wave	Wave Vector	
$dE_m \sim E_{m-1} E_b E_f^*$	$(m-1)\vec{k}_p - m\vec{k}_f$	m odd 3...∞
$dE_m \sim E_{m-1} E_p E_{pc}^*$	$m\vec{k}_p - (m-1)\vec{k}_f$	m even 4...∞
$dE_{mc} \sim E_{(m-1)c} E_b E_f^*$	$m\vec{k}_f - (m-1)\vec{k}_p$	m odd 3...∞
$dE_{mc} \sim E_{(m-1)c} E_{pc} E_p^*$	$(m-1)\vec{k}_f - m\vec{k}_p$	m even 4...∞

The phase mismatch for each succeeding generation increases, thus reducing the power fed from one generation to the next. In addition, this phase mismatch-induced decrease in $|E_m|$ relative to $|E_{m-1}|$ itself enhances the relative decrease of $|E_{m+1}|$. The result is a rapid decrease in the power

---

[2] If the pump waves are exactly plane, these will be true conjugates.

channeled into higher generation waves, E_m. The above considerations indicate that at fixed input pump intensities, the probe-conjugate intensity will first increase, and then saturate as the input probe intensity increases. There are three causes of saturation:

1. There is an intrinsic saturation built into the coupling coefficient $W_{fbp}(I)$.

2. The pump depletion necessary to provide energy to the conjugate beam decreases the coupling triplet.

3. The pump depletion necessary to create the higher generation waves also decreases the coupling.

It will be seen later that a quantitative description of the saturation of the probe-conjugate intensity allows us to predict the intensity crosstalk accurately.

With the introduction of a noise wave E_n, many new interactions occur that can in principle contribute to crosstalk because they lead to depletion of the pump, probe, and/or conjugate beams. First, in a manner analogous to that for the probe beam, the pump beam is depleted by the creation of a noise-conjugate beam E_{nc}, and amplification of the transmitted noise. Second, there is creation of waves analogous to E_1 and E_{1c}: E_1' and its conjugate E_{1c}', where E_p and E_{pc} are replaced in the coupling triplets by E_n and E_{nc} respectively. Third, there are completely new interactions capable of producing crosstalk that are not present in the absence of a noise beam. For example, both the pump and either the probe or the probe conjugate are depleted by the creation of new waves via the following coupling triplets:

Triplet	Wave Vector[3]
$E_b E_p E_n^*$	$\vec{k}_p - \vec{k}_f - \vec{k}_n$
$E_f E_p E_n^*$	$\vec{k}_p + \vec{k}_f - \vec{k}_n$
$E_b E_p E_{nc}^*$	$\vec{k}_p - \vec{k}_f + \vec{k}_n$
$E_f E_p E_{nc}^*$	$\vec{k}_p + \vec{k}_f + \vec{k}_n$ †
$E_b E_{pc} E_n^*$	$\vec{k}_p - \vec{k}_f - \vec{k}_n$
$E_f E_{pc} E_n^*$	$-\vec{k}_p + \vec{k}_f - \vec{k}_n$
$E_b E_{pc} E_{nc}^*$	$-\vec{k}_p - \vec{k}_f - \vec{k}_n$ †
$E_f E_{pc} E_{nc}^*$	$-\vec{k}_p + \vec{k}_f + \vec{k}_n$

The coupling for this third category of waves is weaker because only one factor in the triplet is a pump wave; also two of the 8 terms have a large phase mismatch and the remainder have small mismatches. Therefore, for probe and noise intensities small compared to that of the pump, they cannot be as significant in crosstalk as the pump depletion due to generation of the noise conjugate, $dE_{nc} \sim E_f E_b E_n^*$, and amplification of the noise beam, $dE_n \sim E_f E_b E_{nc}^*$.

The probe and its conjugate can also be directly depleted through coupling triplets that lead to growth of the noise and noise-conjugate waves: $dE_n \sim E_p E_{pc} E_{nc}^*$ (wave vector: $\vec{k}_n$) and $dE_{nc} \sim E_p E_{pc} E_n^*$ (wave vector: $-\vec{k}_n$). This coupling is weak, because there are no pump waves in the triplet, but the phase match is perfect. It will be seen later that our experimental results eliminate these two terms as significant sources of crosstalk in the range of probe-plus-noise intensities we studied.

There are also infinite sequences of waves created in the presence of the noise wave such as:

$dE_1'' \sim E_b E_p E_n^*$	$\vec{k}_p - \vec{k}_f - \vec{k}_n$
$dE_m'' \sim E_{(m-1)} E_p E_f^*$	$m[\vec{k}_p - \vec{k}_f] - \vec{k}_n$ m integer 2...∞

In general, some higher generation waves are simply higher order contributions to an earlier generation wave, and therefore end the sequence. Some, like those just listed, are part of an infinte sequence in which the phase mismatch gets increasingly large, and the coupling terms contain increasingly smaller fields.

---

[3]Wave vectors with three terms of the same sign, marked with †, have a momentum magnitude of $3\omega/nc$ and a very large phase mismatch.

We will show latter in this section that most of our crosstalk results can be explained by invoking only pump depletion caused by growth of the probe, probe-conjugate, noise, and noise-conjugate beams; and by the susceptibility saturation inherent in resonant media. At very high combined probe and noise intensities, however, it may be necessary to attribute part of the crosstalk to the creation of new waves that can exist only in the presence of a noise wave.

5.2.2 Phase Crosstalk

Phase crosstalk, that is, phase variations on E_n that are imparted to E_{pc}, can be studied by examining the coupling terms that contribute to the creation of E_{pc}; the conclusion below will be that no phase noise is transmitted.

In the first generation, we have the pumps, probe, and noise beams. Assume that an element of some second generation wave E_4 results from the coupling of three first generation waves: $dE_4 \sim E_1E_2E_3$. Then an element of a third generation wave E_7 results from the coupling of three second generation waves including E_4: $dE_7 \sim E_4E_5E_6$. Substituting for E_4. we obtain $dE_7 \sim E_1E_2E_3E_5E_6$. In general, an element of any higher generation wave is proportional to all of the lower generation waves that led to its creation. At each stage the number of factors in the coupling term is three, so the final number of factors must be odd, as in the expression for dE_7 above. Further the array of factors in any contribution to dE_{pc} must be of the form,

$$(E_iE_i^*) \; (E_jE_j^*) \; \ldots \; (E_kE_k^*)E_xE_{-x}E_p^*$$

where E_x and E_{-x} are waves travelling antiparallel to each other, such as E_fE_b, or E_pE_{pc}, or E_nE_{nc}. First, the number of unconjugated (unstarred) factors must be one greater than the number of conjugated (starred) factors for the wave element to have the frequency ω appropriate to E_{pc}. Second, each wave other than E_x or E_{-x} must be paired with its conjugate in order that the resultant wave vector be that of E_{pc}; the result is that all wave vectors cancel out, except that of E_p^*. In the above expression, then, we see that if the noise beam appears, it does so only in the pairs $E_nE_n^*$ or E_nE_{nc}. In either case, its phase distribution cancels out and is not imparted to the probe-conjugate wave.

5.2.3 Crosstalk Angular Dependence

In Na vapor the angular response of FWM is limited by thermal motion of the atoms. Particularly in cw experiments, atomic motion washes out the volume diffraction gratings formed by the interference of the probe and pump waves, unless there is only a very small angle between the two corresponding wave vectors. This is discussed in Section 4.3.4. The result is that there is essentially no reflectivity outside some small angle. Similarly, a noise beam cannot reflect outside of this angle, and therefore cannot cause pump depletion at larger angles. Thus we expect a rapid decrease in crosstalk as angular separation between the noise and pumps increases; at larger angles, however, we expect some residual crosstalk due to the intrinsic saturation of the susceptibility in resonant interactions.

5.2.4 Crosstalk Frequency Dependence

An off-resonant noise beam whose frequency is outside the Na linewidth will not reflect in the intensity range considered here. Furthermore, if the noise beam frequency is offset by more than the Na vapor homogeneous linewidth from the pump frequency, it will be poorly reflected (See Section 3.1). Therefore it cannot deplete the pump and cause crosstalk. We anticipate that the crosstalk caused by a noise beam at a given frequency will be correlated with its phase conjugate reflectivity at that frequency.

5.3 INTENSITY CROSSTALK EXPERIMENTAL DESIGN

The effect of a controllable noise source on the probe conjugate intensity was initially studied with the experimental arrangement in Figure 5-1. Two counterpropagating beams of equal intensity were produced by beam splitter BS1 and overlapped in the Na cell. A slight misalignment in the pump beams prevented feedback to the ring dye laser and was essential in maintaining a stable single frequency output. A 1.0 m focal length lens L1 was placed before BS1 to impart equal convergence to both pump legs. Pump intensities at the Na cell were typically 60-70 W/cm^2 after correction for cell window transmittance. The wedged beam-splitter WBS produced two separate beams; the first surface reflection was used to diagnose the frequency output of the dye laser by directing it

76
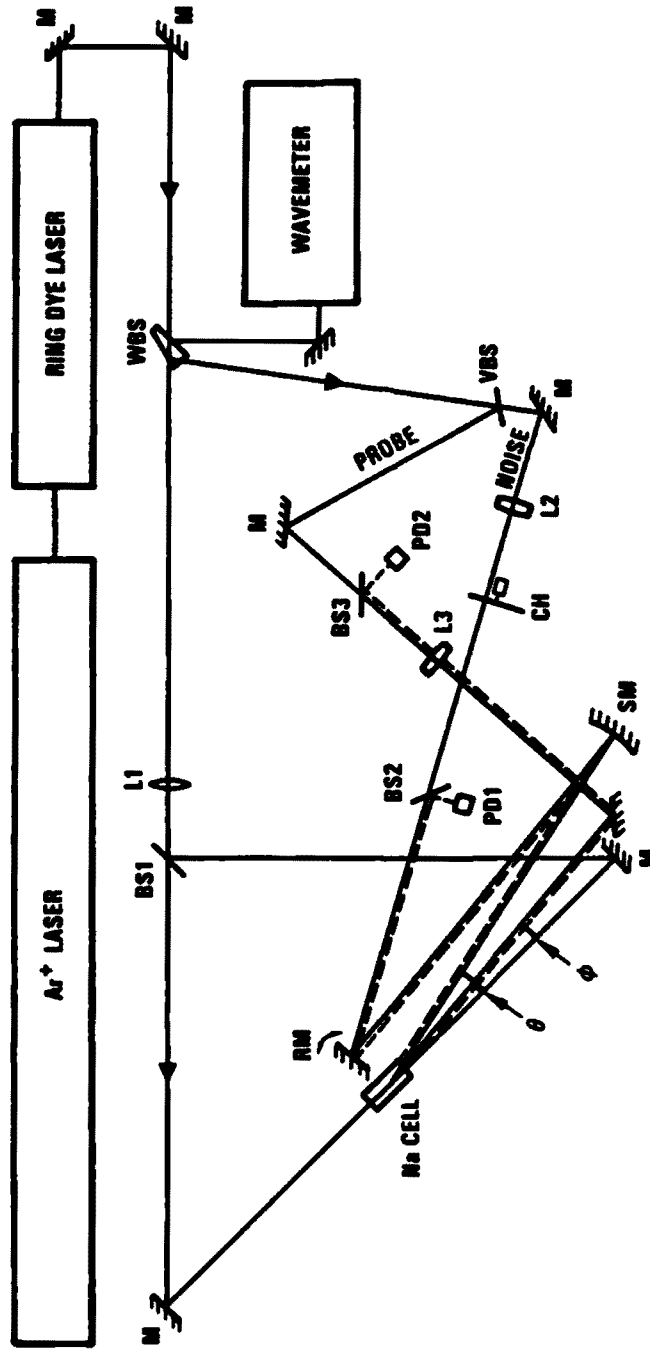
Figure 5-1. Intensity crosstalk experiment.

into a Burleigh wavemeter ($\approx$ 1 GHz frequency resolution), or when greater frequency resolution was required, into the Lamb dip diagnostic described in Section 4.1. The stronger second surface reflection was used to generate both the probe and noise beams. With a fixed total power of both beams established by WBS, the setting of the variable beamsplitter VBS determined the noise-probe intensity ratio.

The probe beam was passed through beamsplitter BS3, focusing lens L3, and directed into the Na cell at a fixed angle φ with respect to the pump beam axis. φ was kept at the minimum allowed by finite beam diameters and was measured to be 6.6 mrad for the arrangement diagrammed in Figure 5-1. Variable noise beam angles were obtained by the use of a precision spherical mirror SM and an electromechanically driven rotatable mirror RM. Both RM and the Na cell were located at radius of curvature distances from SM such that the noise beam overlap with the pump and probe beams remained constant at all noise beam input angles θ. θ was varied from a minimum of 13 mrad to 24 mrad with respect to the pump beam axis while the noise beam itself was moved in a direction perpendicular to the plane containing the pump and probe beams (See Figure 5-2). The noise beam was temporally chopped to detect small changes in the probe-conjugate intensity level in its presence. The probe- and noise-beam-conjugate intensities were measured by photodiodes PD2 and PD3 respectively, and their outputs were displayed on an oscilloscope.

5.4 INTENSITY CROSSTALK RESULTS

Typical crosstalk data appears in Figure 5-3 where S is the measured probe-conjugate intensity level in the absence of the noise beam and ΔS is the decrease in the conjugate intensity level in the presence of the noise beam. The ratio $\Delta S/S$ is defined to be the fractional crosstalk experienced by the probe conjugate due to the presence of the noise beam. The lower trace in Figure 5-3 displays the conjugate intensity of the chopped noise beam which was found to be correlated to the decrease observed in the probe conjugate level. Only decreases in probe-conjugate intensities were observed in the presence of noise beams; no increases in probe-conjugate levels were discerned with the addition of noise sources. This is consistent with the crosstalk mechanisms listed in Section 5.2, i.e., saturation of the resonant susceptibility and pump depletion.

78

$\phi = 6.6$ mrad

24 mrad $> \theta >$ 13 mrad
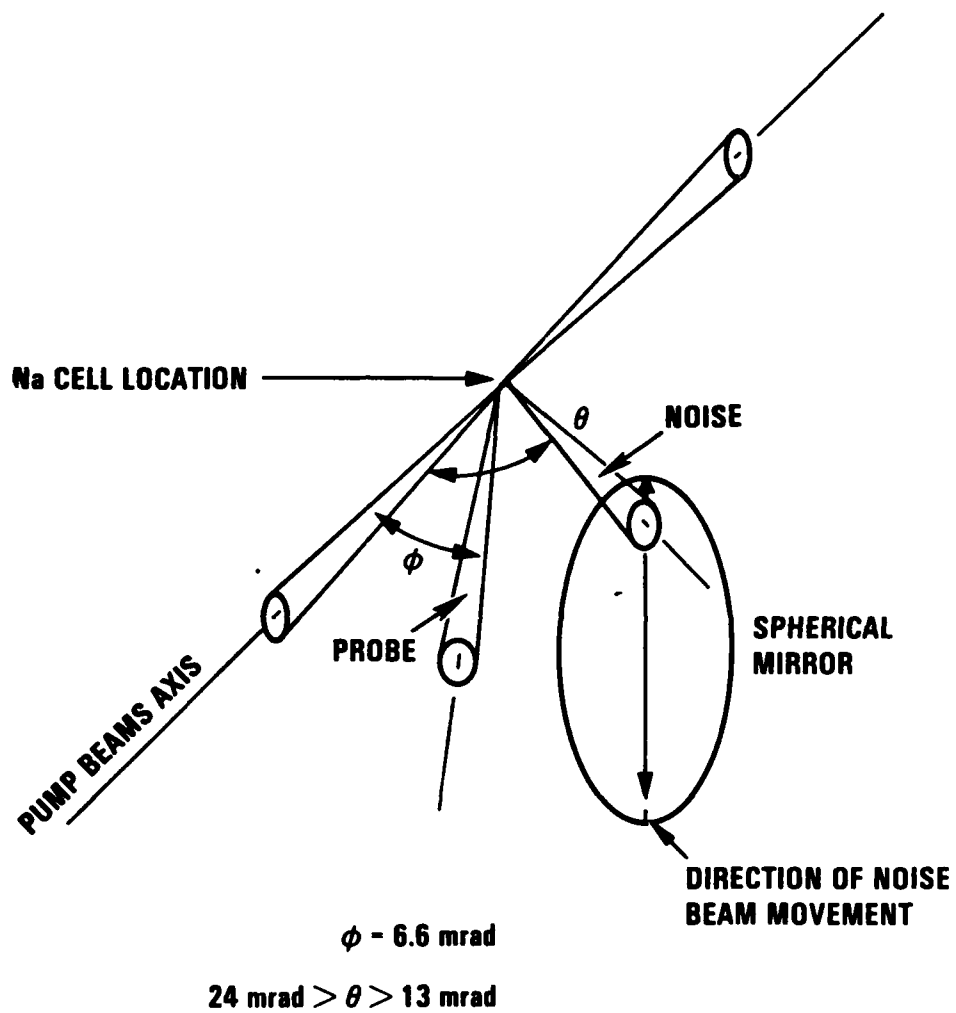
Figure 5-2. Geometry for intensity crosstalk experiments.

Crosstalk Experiment
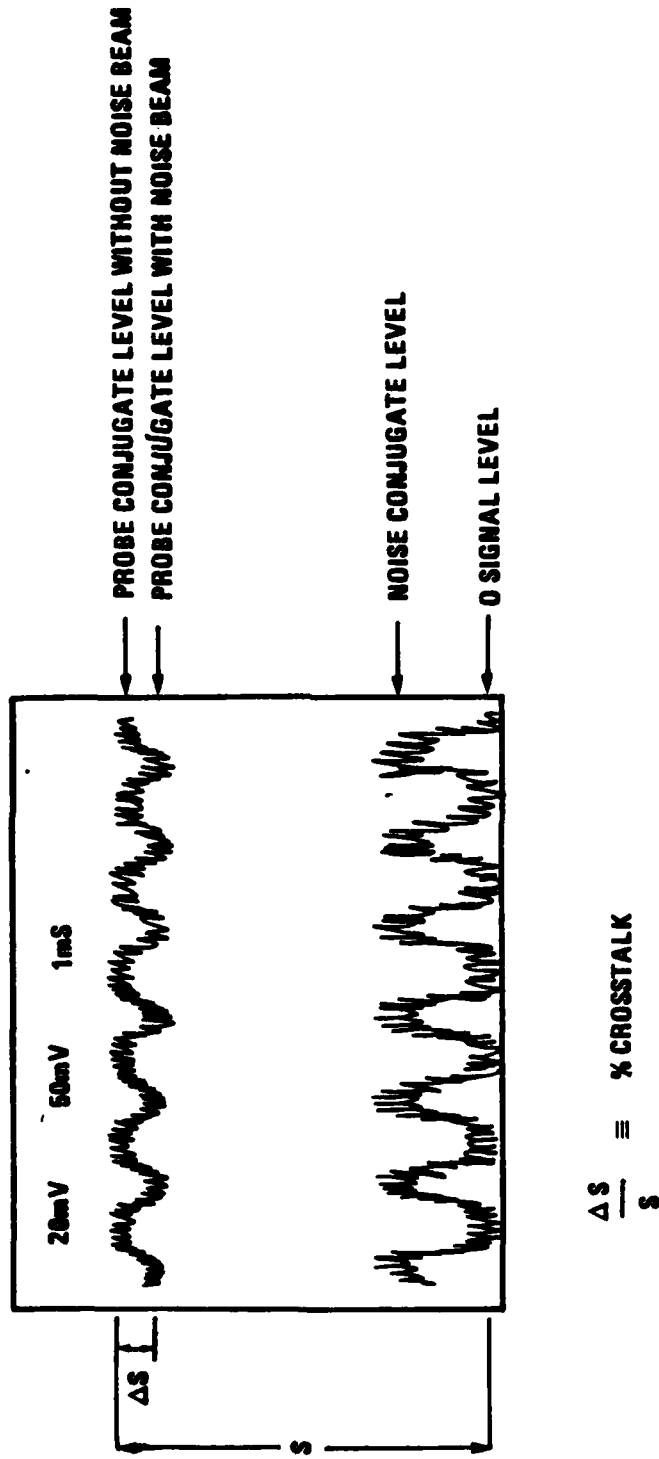
$$\frac{\Delta S}{S} \equiv \% \text{ CROSSTALK}$$

Figure 5-3. Typical intensity crosstalk data showing phase conjugate returns of the probe and noise beams. The noise beam was mechanically chopped.

5.4.1 Noise/Probe Intensity Ratio and Angle Variation

Noise-probe intensity ratios of 3:1 and 1:1 were used in the study of the effect of noise beam intensity and input angle on probe-conjugate intensity (See Figures 5-4 and 5-5). At noise-probe intensity ratios below 1:1, crosstalk was observed but was difficult to quantify due to the small change in the probe conjugate intensity. Data from Figures 5-4 and 5-5 are plotted in Figure 5-6 as percent crosstalk versus input noise beam angle from the minimum θ of 13 mrad. For both sets of data, increases in the noise input angle reduce the observed percent crosstalk. The 3:1 noise-probe intensity ratio produced consistently higher crosstalk values at all noise input angles when compared to the 1:1 data set; however, when normalized to their respective maxima in Figure 5-7, both data sets display similar angular dependences. A correlation between noise beam conjugate intensity and percent crosstalk can be seen in Figures 5-8 and 5-9 where the normalized noise-conjugate intensity and normalized percent crosstalk have been plotted against noise beam input angle. For the 3:1 intensity ratio data set (Figure 5-8), the noise conjugate intensity is seen to decrease more rapidly than the percent crosstalk with increases in noise input angle. A more similar angular dependence was demonstrated by the 1:1 intensity ratio data set in Figure 5-9 where relative noise-conjugate intensity and crosstalk differ at most by 6-7%.

These results suggest that the observed intensity crosstalk is caused by two terms: one angle dependent and one angle independent. In Section 5.2 we indicated that crosstalk induced by pump depletion should occur only within a small angular range between the noise and pump beams, namely, the range over which the noise-conjugate intensity is large. Figures 5-8 and 5-9 show that this range is about 8-10 mrad, consistent with the angular dependence data presented in Section 4.3.4, and Figure 5-6 confirms a sharp fall-off in crosstalk out to this angle. Section 5.2 also indicated that angle independent crosstalk due to susceptibility saturation is expected. The data does not extend to large enough angles to verify this expectation completely, but the curves in Figure 5-6 show signs of flattening at about 10 mrad.

Angle independent effects can be inferred from another viewpoint in Figure 5-8, where the noise-conjugate intensity and the crosstalk are both plotted as percentages of their maximum values versus the pump-

81

Probe power = 2.0 mW   Pump power = >360 mW

Noise power = 7.5 mW

Cell temperature = 248°C

ϕ = 6.6 mrad = pump beam-probe beam angle

θ = pump beam-noise beam angle

I_{pump} = 64 W/cm^2

I_{probe} = 0.7 W/cm^2 } corrected for window transmission

I_{noise} = 2.0 W/cm^2

θ (mrad)	Relative θ (mrad)	Noise Conjugate Intensity	Crosstalk % of Probe	% of Maximum Crosstalk
13.00	0	8.0 (100%)	20.6	100
13.93	0.93	5.7 (71.25%)	14.3	69.4
16.40	3.40	3.4 (42.5%)	11.5	55.8
19.85	6.85	1.5 (18.75%)	10.9	52.7
23.85	10.85	0.75 (9.38%)	8.82	42.8

Figure 5-4.   Intensity crosstalk results when the noise beam is 3-4 times larger than the probe beam.

Probe power = Noise power = 3-4 mW

Cell temperature = 245°C (no buffer gas) → 2×10^{13} atoms/cm^3

ϕ = probe-pump angle = 6.6 mrad (closest possible)

θ = pump beam-noise beam angle

I_{pump} = 64W/cm^2
I_{probe} = 1.0W/cm^2 } corrected for window transmission
I_{noise} = 0.8W/cm^2

Noise Conjugatge Intensity	θ (mrad)	Crosstalk % of Probe	% of Max. Crosstalk
8.0 (100%)	13.00 (minimum)	9.38	100
6.8 (85%)	13.93	8.21	87.5
6.0 (75%)	16.40	6.56	69.9
3.5 (44%)	19.85	4.73	50.6
2.8 (35%)	23.85	3.73	39.8

Figure 5-5. Intensity crosstalk results when probe and noise powers are equal.
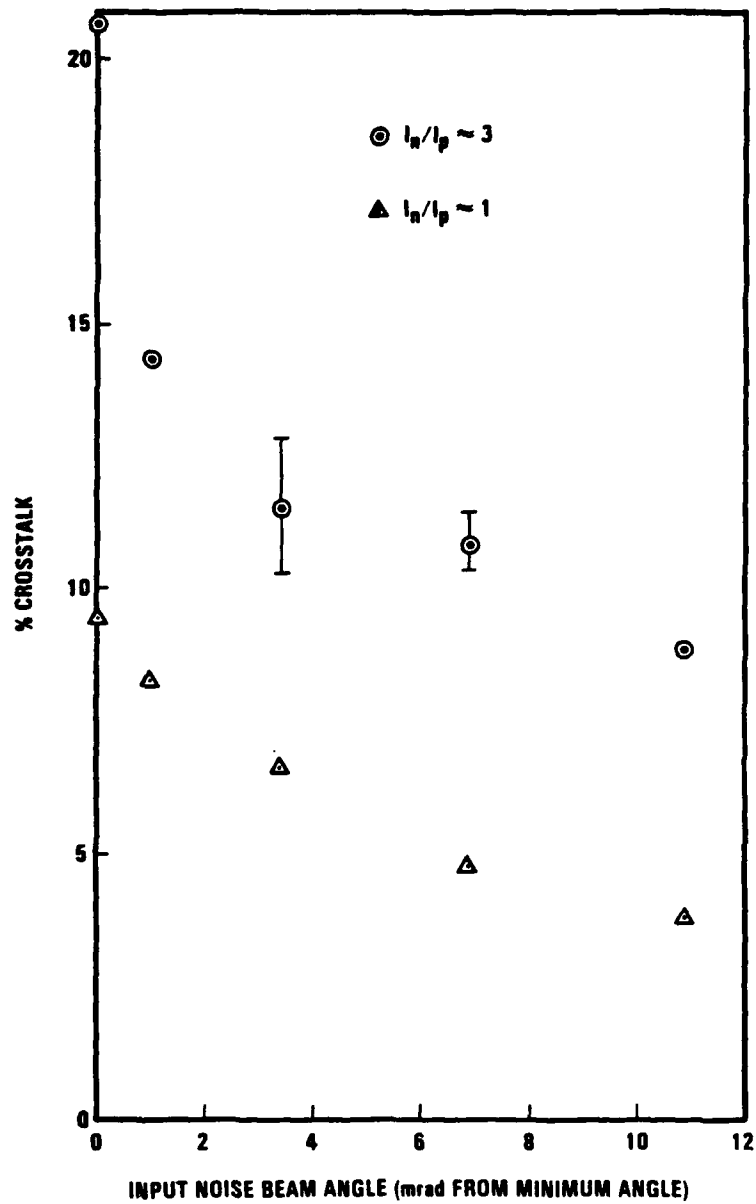
Figure 5-6. Intensity crosstalk data plotted in a function of
noise-pump angle.

84
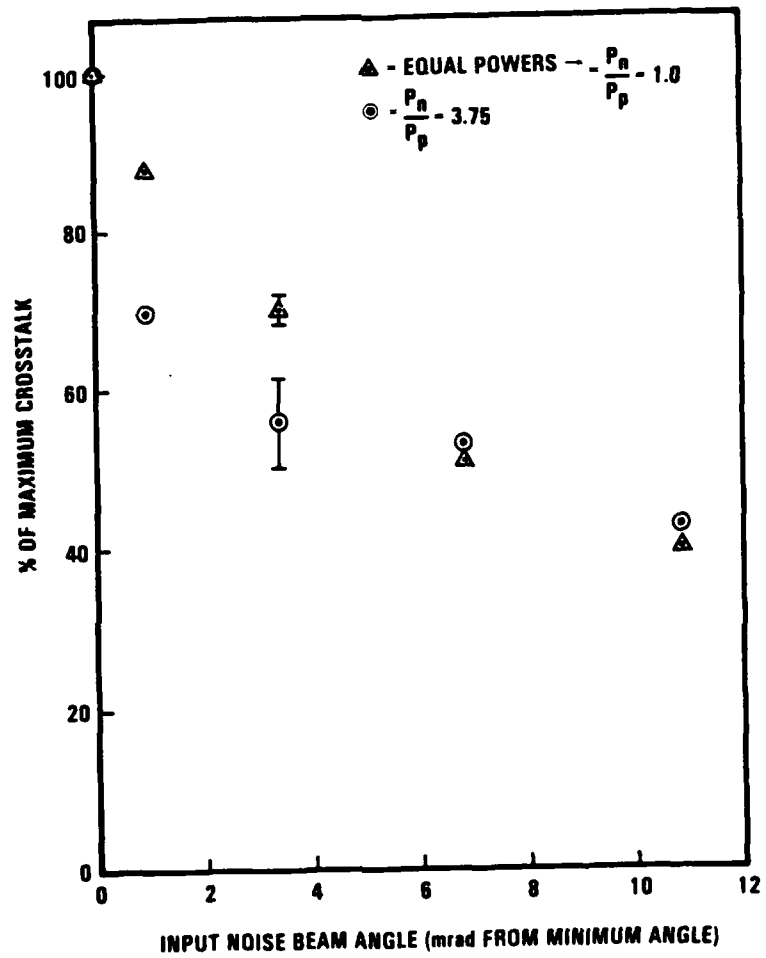
Figure 5-7. Normalized intensity crosstalk data showing
similar angular dependence for noise/probe
ratios of 3.75 and 1.0.
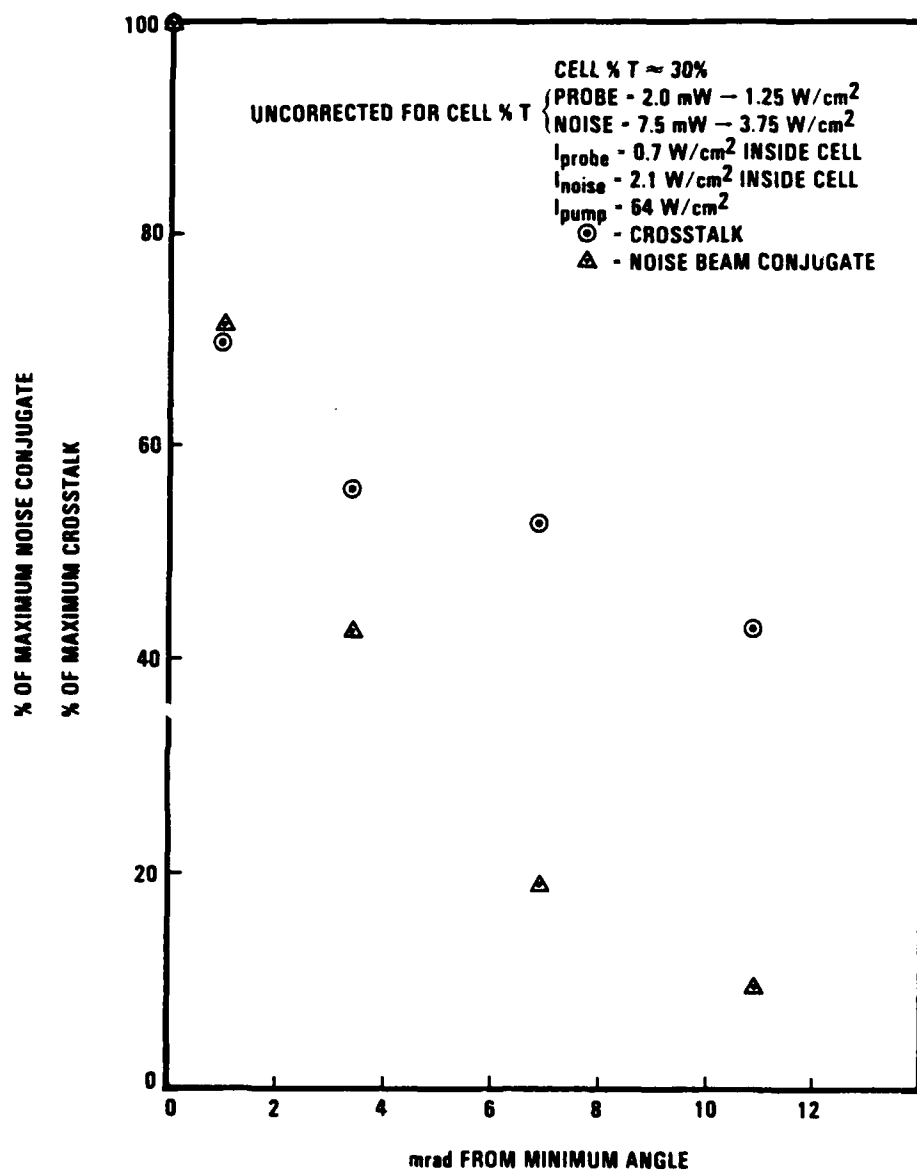
Figure 5-8. Noise conjugate intensity and observed crosstalk as a function of noise-pump angle for noise/probe ratio of 3.0.

noise angle. Here the noise-probe intensity ratio is 3:1, and we see the noise-conjugate intensity decreasing much more rapidly than the crosstalk. This should be compared with the behavior seen in Figure 5-9, where the same quantities are plotted for a noise-probe intensity ratio of 1:1. Here the noise-conjugate intensity falls off only slightly faster than the crosstalk. The relative behavior in these two figures can be explained by assuming that the crosstalk is dominated at smaller angles by pump depletion, and at larger angles, where the noise-conjugate intensity is small, by susceptibility saturation. The greater large-angle crosstalk in Figure 5-6 is expected because the higher noise intensity produced more saturation.

5.5 POLARIZATION CROSSTALK EXPERIMENTAL DESIGN

Intensity crosstalk studies were carried out where the polarization states of the probe and noise beams were varied. The experimental arrangement diagrammed in Figure 5-10 differs from the first crosstalk experiment (Figure 5-1) by the placement of the noise and probe beams on opposite sides of the pump beam axis. The data collected here, when all beams beams were copolarized, could then be compared with early crosstalk results to determine whether noise-probe beam angle and/or pump-noise/pump-probe beam angles were significant parameters in the determination of the extent of crosstalk.

Both the probe and noise beams were focused at the Na cell by a single high quality achromat L2 (focal length 45 cm) and their overlap with the pump beams carefully checked by replacement of the Na cell with a precision pinhole. The probe-pump angle φ and the noise-pump angle θ were kept to the minimum allowed by finite beam diameters and were measured to be 8.5 mrad and 10.5 mrad, respectively. The linear polarization of the noise and probe beams was manipulated by half waveplate polarization rotators WP placed behind L2. The waveplates were deliberately arranged to be the last optical elemnt in the noise and probe beam paths in order to maintain the direction of linear polarization of both beams. Polarization directions were determined with a Karl Lambrecht laser beam polarizer (MSCA10) and the degree of polarization, defined by

$$P = I_{parallel}/(I_{perpendicular} + I_{parallel}),$$
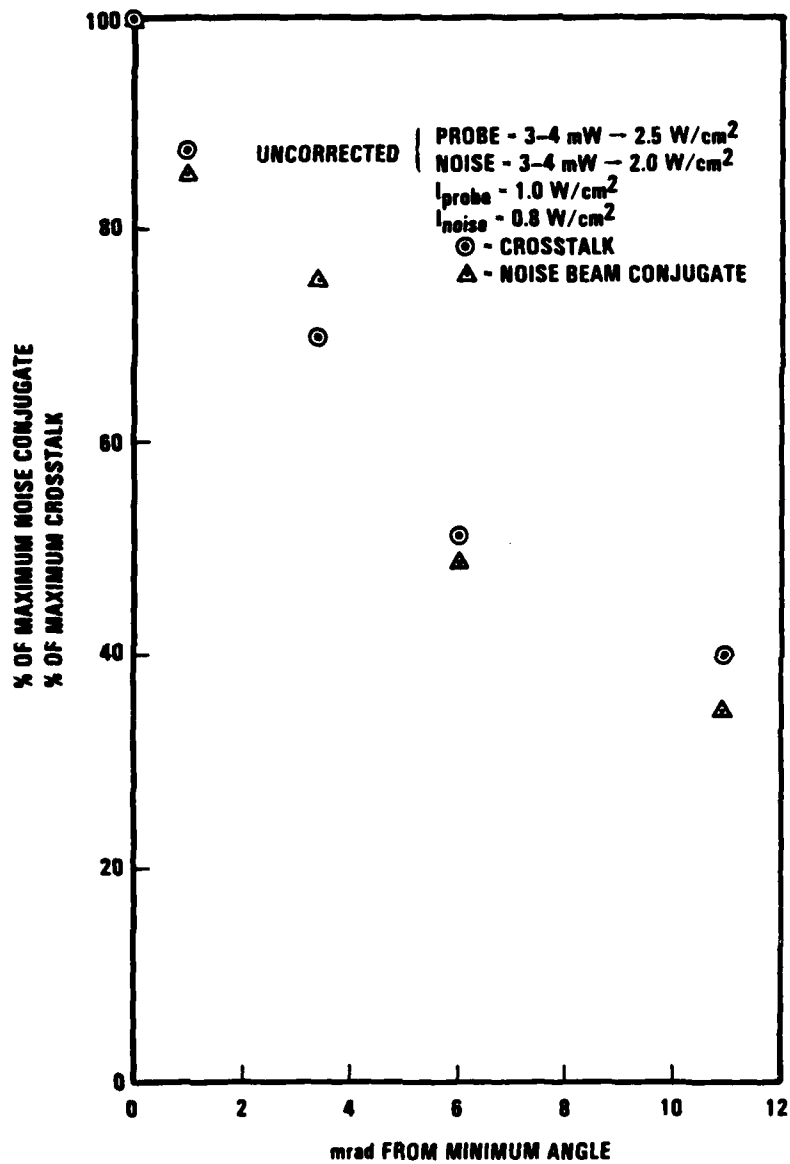
Figure 5-9. Noise conjugate intensity and observed crosstalk as function of noise-pump angle for noise/probe ratio of 0.8.
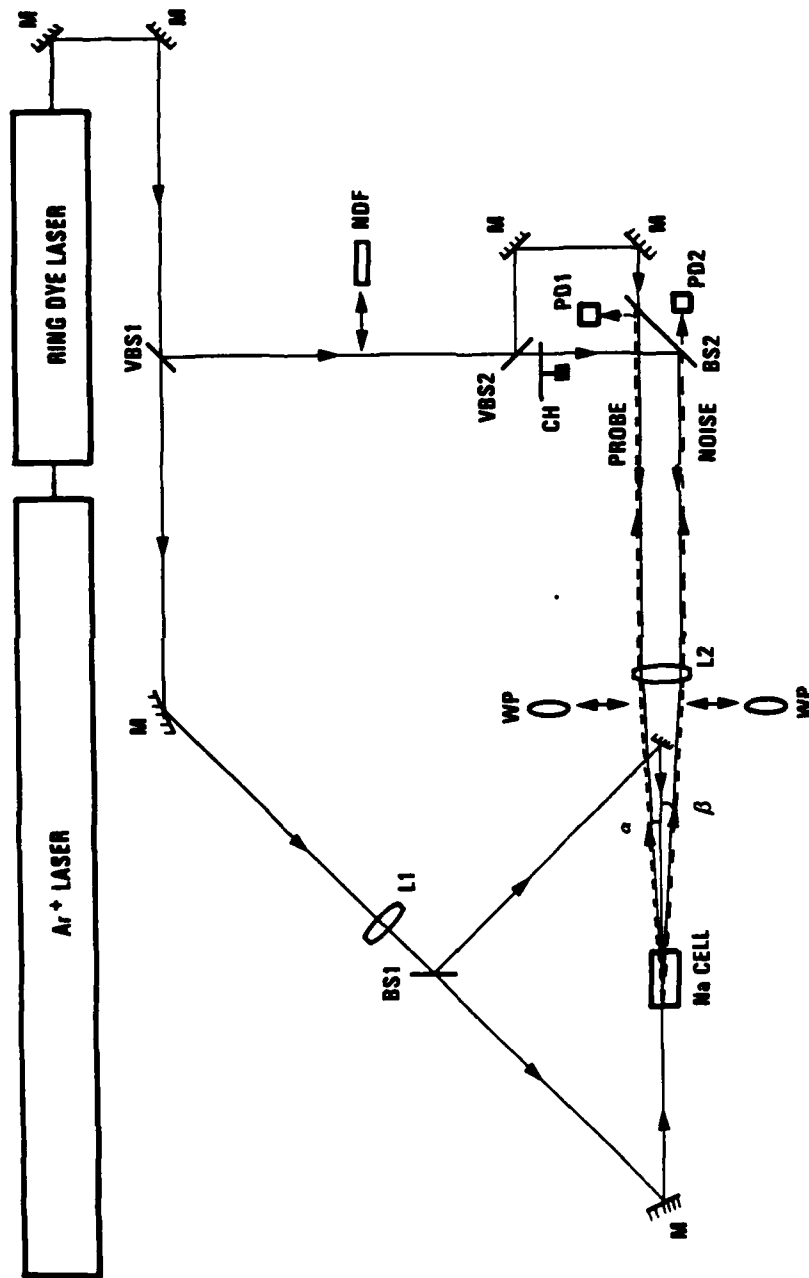
Figure 5-10. Intensity crosstalk experiment to measure polarization dependence.

was measured to be greater than 0.98 for all beams at the Na cell.
Relative probe and noise beam intensities were adjusted by variable
beamsplitter VBS2 and the total input intensity

$$I_{total} = I_{noise} + I_{probe}$$

was controlled by insertion of neutral density filters NDF into the beam
generated by variable beamsplitter VBS1. As before, both probe and noise
conjugates were monitored with matched photodiodes PD1 and PD2 and their
outputs displayed on an oscilloscope triggered by the noise beam chopper
CH.

5.6 POLARIZATION CROSSTALK RESULTS

Intensity crosstalk was measured in three distinct probe-pump-noise
polarization states. The copolarized state, where all planes of polariza-
tion were vertical and parallel, served as a reference state for intensity
crosstalk. The second state is referred to as the parallel state and is
established when the plane of polarization of the probe and noise beams
are parallel, but both are angled at 45° with respect to the pump polariza-
tion plane. The third state, where the probe and noise polarization
planes are orthogonal to each other but at 45° with respect to the pump
plane, is referred to as the perpendicular state. The results of two
independent experiments are presented in Figure 5-11 where the crosstalk
obtained in the parallel and perpendicular states is compared to that of
the reference copolarized state. Although the measured crosstalk for the
copolarized state differed slightly in the two experiments, in both cases
the parallel and perpendicular states yielded essentially the same
percentage crosstalk values as the reference state. Hence, intensity
crosstalk does not appear to depend on the orientations of the pump,
probe, and noise beam polarization planes.

Figure 5-11. Polarization Crosstalk Results

Case	Na Cell Temperature (°C)	Polarization State	Pump Power (mW)	Probe Power (mW)	Noise Power (mW)	Percent Crosstalk*
1	250	copolarized	400	9.9	8.4	31.8
		perpendicular				29.9
2	248	copolarized	380	8.5	7.6	26.9
		perpendicular				26.7

*Average of six measurements

5.7 CROSSTALK MODEL VERIFICATION

If pump depletion and susceptibility saturation are the principal causes of noise-induced crosstalk, then in a noise-free interaction they should manifest themselves as saturation of the probe-conjugate intensity at high probe intensities. The experimental approach used to test this assumption is outlined in Figure 5-12. Two counterpropagating pump beams of equal powers were formed by BS1 and focused to a 400 μm $1/e^2$ diameter at the Na cell. Pump intensities were typically 125-132 W/cm^2. A single probe beam was directed into the cell by BS2 and L2 to form a 200 μm $1/e^2$ diameter spot at the cell. The pump-probe angle was 8.5 mrad. Probe intensity was varied from 2-40 W/cm^2 by insertion of neutral density filters NDF into the probe beam path. Care was taken to precisely locate the neutral density filters to insure constant pump-probe overlap at the cell. At each probe input intensity, reflected power and gain were measured by PD1 and PD2 respectively. The results of two independent trials are listed in Figures 5-13 and 5-14 and displayed in Figure 5-15, where reflected power as a percentage of pump power is plotted against input probe intensity for both sets of data; the two trials are distinguished by circles or triangles around the plotted points. It is evident that the reflected power saturates as the probe intensity is increased; this will be shown to account for the observed intensity crosstalk.
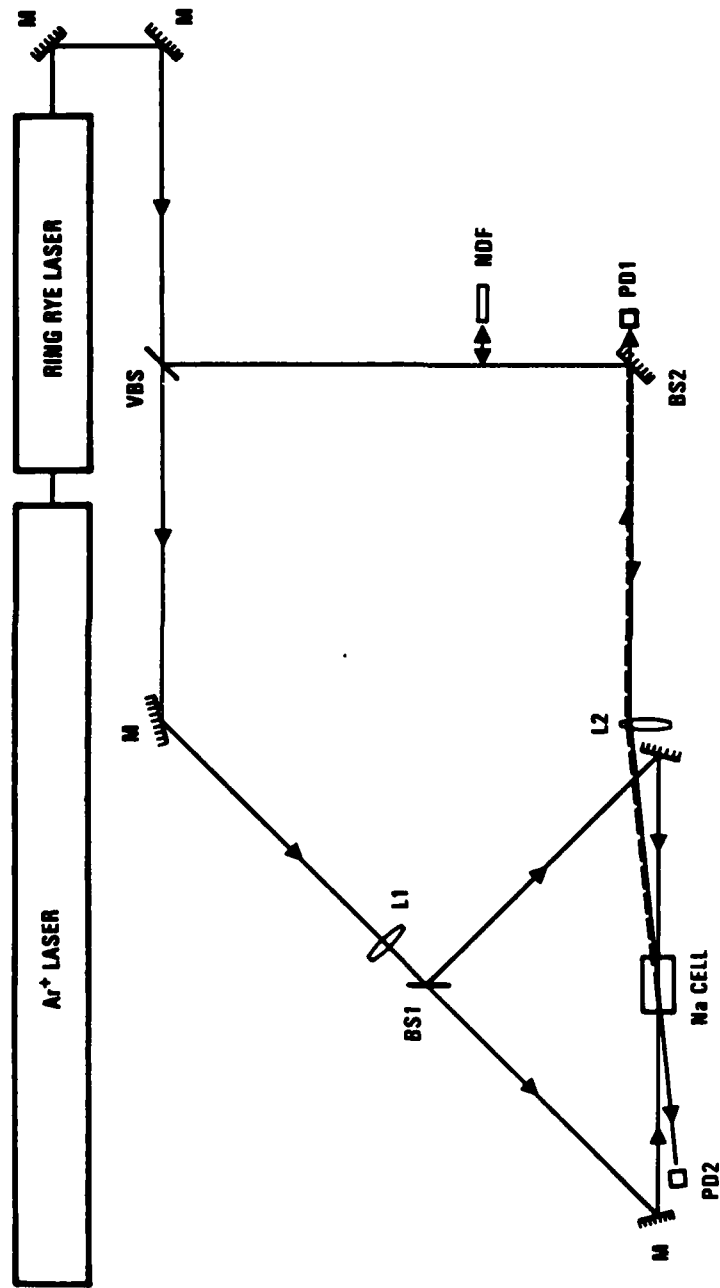
Figure 5-12. Reflected power saturation experiment layout.

ND	GAIN	REFLECTIVITY	R/G	GROSS mW ( ) = % OF PUMP POWER	NET mW	PROBE INPUT POWER (mW)	INPUT INTENSITY (W/cm²)	PROBE CONJUGATE	R	PROBE THROUGHPUT* (mW)
0	0.825	0.238	0.288	(1.70) 9.83 + 2.83 = 12.66	12.66 - 11.91 = 12.66	22.0	38.4	0.76 - 0.085	23.8	5.2
0.3	0.857	0.340	0.397	(1.35) 5.67 + 2.25 = 7.92	7.92 - 6.61 = 1.31	12.5	21.3	0.63 - 0.095	34.0	3.0
0.5	1.043	0.428	0.410	(1.21) 4.91 + 2.02 = 6.93	6.93 - 4.71 = 2.22	8.9	15.2	0.57 - 0.09	42.8	2.6
0.8	0.952	0.503	0.528	(0.72) 2.27 + 1.20 = 3.47	3.47 - 2.38 = 1.09	4.50	7.68	0.38 - 0.095	50.3	1.2
1.0	1.21	0.768	0.635	(0.52) 1.38 + 0.87 = 2.25	2.25 - 1.14 = 1.11	2.15	3.67	0.30 - 0.092	76.8	0.73
1.3	1.36	0.722	0.531	(0.28) 0.87 + 0.46 = 1.33	1.33 - 0.64 = 0.69	1.21	2.06	0.20 - 0.090	72.2	0.46

*Power meters identical in these ranges

Cell % T = 0.28

$$\text{gain} = \frac{\text{output}}{\sqrt{0.28}\ \text{probe}} = \frac{\text{output}}{\text{input}\ (\sqrt{0.28})}$$

$$\text{reflectivity} = \frac{\frac{\text{conjugate}_m}{(0.5)(0.9)}}{\text{input}\ (0.28)} = \frac{\text{output}}{\text{input}\ (0.28)}$$

(0.9) = lens % T
(0.5) = beamsplitter (50-50)

conjugate_m = measured conjugate power

conjugate_R = real (corrected) conjugate power

$$\text{gross mW} = \frac{\text{output}}{\sqrt{0.28}}$$

$$\text{net mW} = \text{gross mW} - \sqrt{0.28}\ \text{probe input} + \frac{\text{conjugate}_R}{\sqrt{0.28}}$$

$$\frac{\text{conj}_m}{(0.5)(0.9)} = \text{conj}_R$$

Figure 5-13. Energy Bookkeeping.

ND	GAIN	REFLECTIVITY	R/G	GROSS mW ( ) = % OF PUMP POWER	NET mW	PROBE INPUT POWER (mW)	INPUT INTENSITY (W/cm²)	PROBE CONJUGATE (mW)	R	PROBE THROUGHPUT
0	0.824	0.244	0.296	(1.81) 10.20 + 3.02 = 13.22	13.72 - 12.38 = 0.84	23.4	39.9	0.8 - 0.08	24.4	5.40
0.3	0.954	0.370	0.388	(1.45) 6.24 + 2.42 = 8.66	8.66 - 6.53 = 2.13	12.35	21.1	0.66 - 0.084	37.0	3.30
0.5	0.944	0.456	0.483	(1.26) 4.35 + 2.10 = 6.45	6.45 - 4.60 = 1.85	8.70	14.85	0.59 - 0.09	45.6	2.30
0.8	1.043	0.553	0.530	(0.78) 2.46 + 1.30 = 3.76	3.76 - 2.35 = 1.41	4.45	7.6	0.40 - 0.09	55.3	1.30
1.0	1.263	0.805	0.637	(0.54) 1.42 + 0.90 = 2.32	2.32 - 1.12 = 1.20	2.12	3.62	0.31 - 0.095	80.5	0.75
1.3	1.417	0.661	0.466	(0.26) 0.94 + 0.44 = 1.38	1.38 - 0.67 = 0.71	1.26	2.15	0.20 - 0.095	66.1	0.50

Cell % transmission at probe position = 28%

Cell % transmission at pump position = 28%

Figure 5-14. Energy Bookkeeping

The experimental points in Figure 5-15 can be fit very well with the expression,

$$\frac{I_{pc}}{I_{pump}} = \frac{AI_p}{1 + BI_p} \tag{5-3a}$$

where I_{pump} is the total pump intensity, I_p and I_{pc} are the probe and probe-conjugate intensities, all in W/cm^2, and A and B are

$$\left. \begin{array}{l} A = 1.71 \times 10^{-3} \ cm^2/W, \\[2mm] B = 7.27 \times 10^{-2} \ cm^2/W \end{array} \right\} \tag{5-3b}$$

The points inside the squares in Figure 5-15 are calculated from Eqn 5-3. It should be remembered that the values of A and B apply to a particular pump-probe angle (8.5 mrad) and pump intensity (125-132 W/cm^2), and presumably are dependent upon these variables.

It has been shown that numerical, theoretical predictions of probe-conjugate intensity in a Kerr-like medium can be fit quite accurately with an expression of the form (Ref 5-4),

$$\frac{I_{pc}}{I_{pump}} = \frac{aI_p}{1 + aI_p} .$$

Since $B/A \gg 1$ in Eqn. 5-3, it follows that the curve in Figure 5-15 saturates much more strongly than that predicted for a Kerr-like medium, although it must be remembered that Eqn. 5-3 has not been verified beyond a probe intensity of about 40 W/cm^2. Nevertheless, the comparison shows that in Na, if the theory is correct, there must be an additional saturating mechanism at least as significant as pump depletion. The most likely candidate is coupling saturation, as suggested by the experimental results on crosstalk vs. noise input angle, and crosstalk vs. probe:noise intensity ratio.

With the aid of two assumptions, Eqn. 5-3 can be used to predict the crosstalk for an experiment in which the noise and probe beams make the same angle with the pump beam as the probe beam did in the previous experiment, and for which the pump intensity is also the same as before. The first assumption is that the noise and probe together can be regarded as a single beam, and that the noise- and probe-conjugates can similarly be regarded as a single beam. That is,
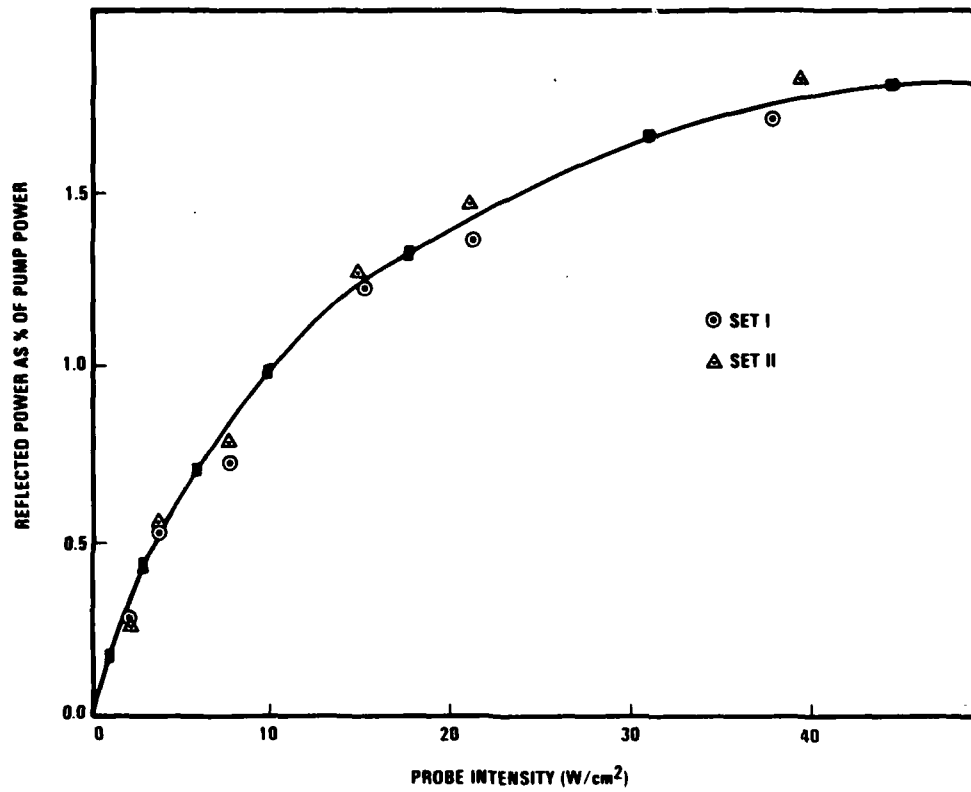
Fig. 5-15. Probe conjugate power as function of input intensity.
Reflected power as % of pump power saturates at higher power input intensities.

96

$$\frac{I_{pc} + I_{nc}}{I_{pump}} = \frac{A(I_p + I_n)}{1 + B(I_p + I_n)} = \frac{AI_p}{1 + B(I_p + I_n)} + \frac{AI_n}{1 + B(I_p + I_n)}.$$

The second assumption is that the ratio of probe-conjugate to noise-conjugate intensities is equal to the ratio of probe to noise intensities,

$$\frac{I_{pc}}{I_{pump}} = \frac{AI_p}{1 + B(I_p + I_n)}. \tag{5-4}$$

Defining the crosstalk C by

$$C = \frac{I_{pc}(\text{no noise}) - I_{pc}(\text{noise})}{I_{pc}(\text{no noise})},$$

and using Eqn. 5-4, we obtain

$$C = \frac{BI_n}{1 + B(I_p + I_n)} \tag{5-5}$$

Figure 5-16 is a graphical explanation of Eqn. 5-5. Probe and noise intensities are summed on the x-axis to determine the total conjugate power expected. This is divided into noise and probe components in the ratio of the noise and probe input intensities. For equal noise and probe intensities, the probe conjugate becomes $C_{p+n}/2$ as shown in the bottom portion of Figure 5-16, and that is less than the intensity C_p that would have been obtained in the absence of a noise beam.

A test of the predictive capability of Eqn. 5-5 was carried out with the experimental arrangement of Figure 5-10. A noise:probe intensity ratio of 1.16:1.00 was used with a pump-probe angle of 8.5 mrad and a pump-noise angle of 10.5 mrad; one can see from Figures 5-8 and 5-9 that there is a relatively small difference in noise beam reflectivity at these two angles, so that Eqn. 5-5 should be applicable. Total input intensity ($I_{pr} + I_n$) ranged from 1.5-28 W/cm^2 and was varied by the insertion of neutral density filters into the beam which generated both the probe and noise beams. The effect of the insertion of each neutral density filter on the spatial overlap of pump, noise, and probe beams was carefully checked in order to maintain a constant overlap in the Na cell. Experimental conditions were otherwise identical to those of Figure 5-15.

The results of this intensity crosstalk experiment are shown in Figure 5-17 together with the predicted crosstalk values derived from Eqn. 5-5. There is good agreement between predicted and measured values

97

REFLECTED POWER VERSUS INPUT INTENSITY
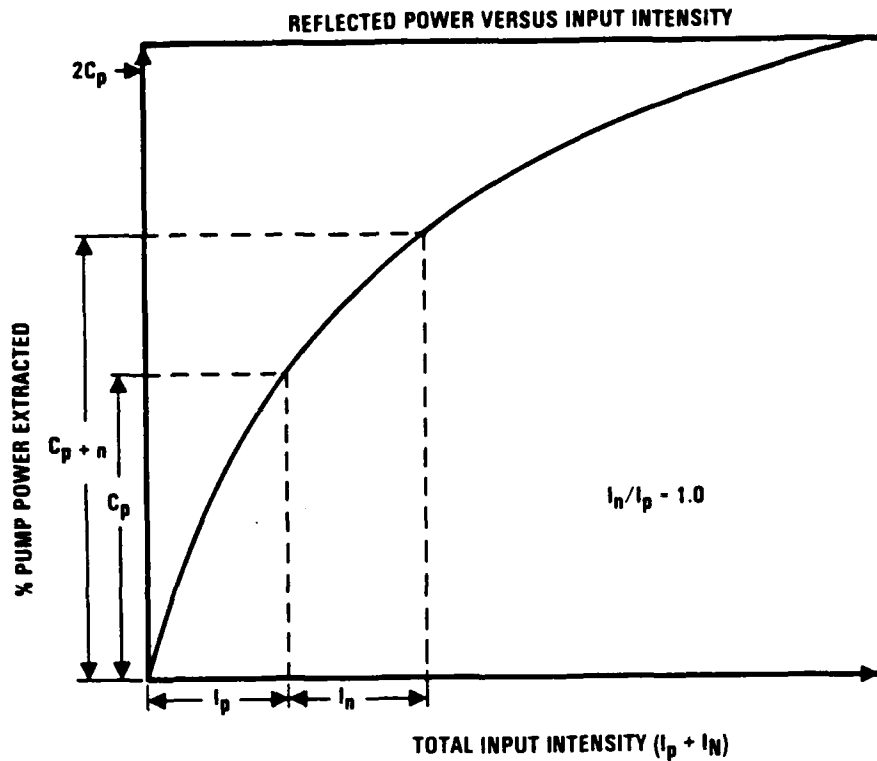
NOTE: C_{p+n} EQUALLY DISRIBUTED TO NOISE AND PROBE CONJUGATES

$$CROSSTALK - \frac{C_p - \frac{C_{p+n}}{2}}{C_p}$$
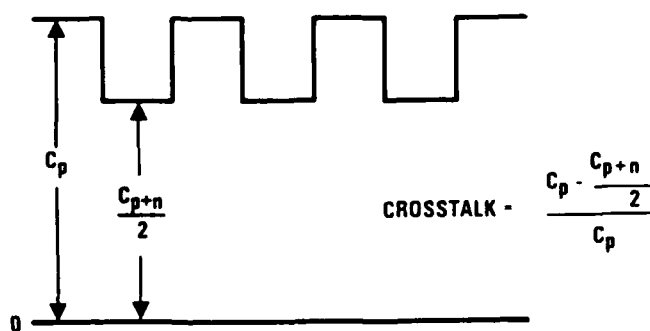
Figure 5-16.   Diagramatic representation of intensity crosstalk mechanism. It is the nonlinear dependence of conjugate reflectivity on input probe/noise intensity that leads to crosstalk.

98
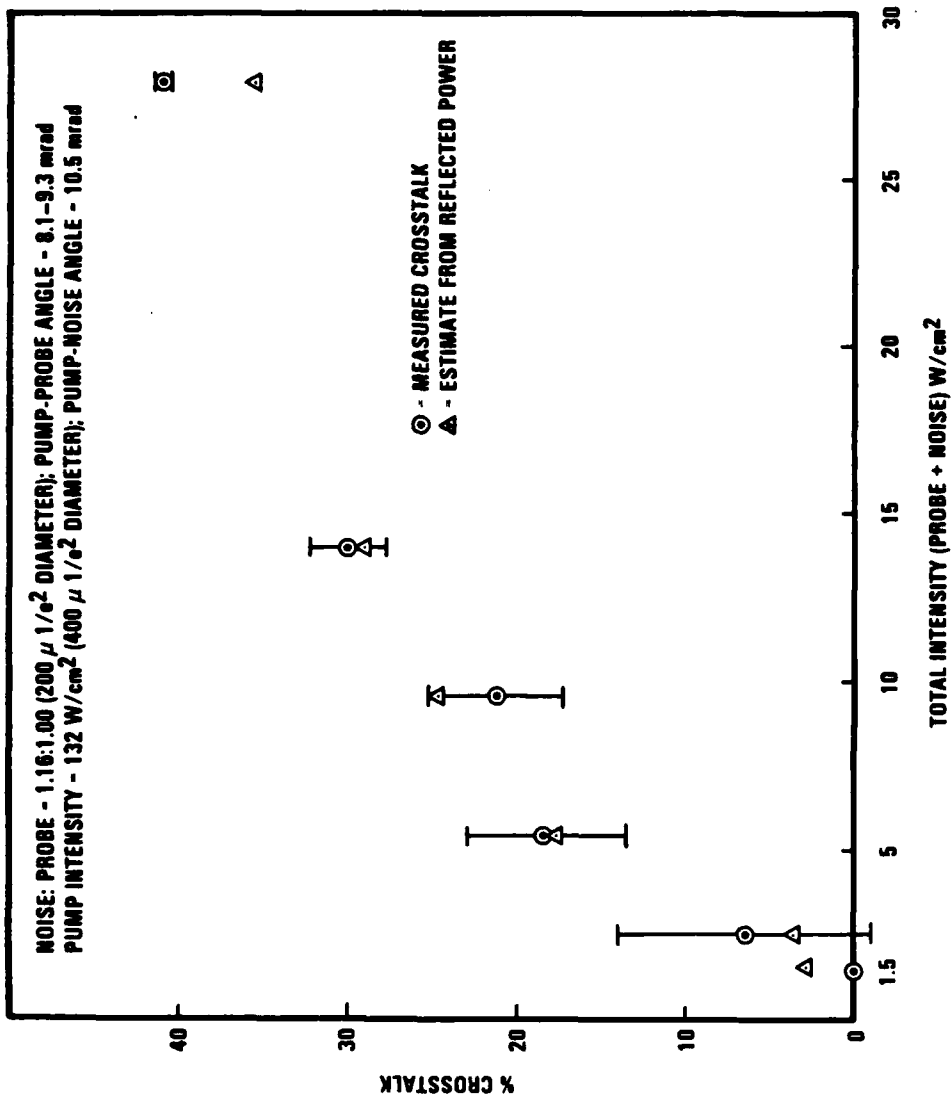
Figure 5-17. Predicted and observed intensity crosstalk measurements.

at all but the highest input intensity. The agreement at the lower intensities indicates that the same mechanisms that cause saturation of the probe-conjugate intensity in the noise-free experiment -pump depletion and coupling saturation being the prime candidates- are principally responsible for crosstalk. Therefore, at the smaller input intensities, those mechanisms discussed in Section 5.2 that are operative only in the presence of noise are not significant in causing crosstalk. In particular, this excludes direct probe and probe-conjugate depletion as important sources of crosstalk at the lower noise-plus-probe intensities.

At the high probe-plus-noise intensity of 28 W/cm^2, however, the situation is somewhat different. Here the measured crosstalk is significantly greater than that predicted, and the latter is well outside the experimental error bars. A possible explanation is that, at sufficiently high probe and noise intensities, additional coupling mechanisms such as that described by the triplet $E_b E_p E_n^*$ come into play.

An indication of the effect of increased probe intensity on extractable pump power can be seen when the net extracted power (NEP) defined as:

NEP — (transmitted power + reflected power) - input power

is plotted against input intensity as in Figure 5-18. For probe intensities up to approximately 15 W/cm^2, a steady increase in extracted pump power is recorded. However, with greater intensities the extracted pump power decreases until at 40 W/cm^2 the NEP is approximately the value obtained at 2 W/cm^2. One explanation for the observed roll-over is that at probe intensities > 15 W/cm^2, the probe is strong enough to act as a "pump" beam and scatter power back into the true pump beams, thus decreasing its intensity and its ability to extract power from the true pumps.

5.8   TOLERABLE NOISE INTENSITY: An Example

To illustrate the potential practicability of our crosstalk results, we use them to estimate the tolerable noise intensity in an intensity modulated communication system. We assume that a constant intensity probe beam is sent through an aberrating medium to a FWM, where a time-varying intensity signal is imposed on the probe-conjugate beam; the latter than returns through the aberrating medium to a detector. The information is encoded in binary form; the probe-conjugate intensity I_{pc} is either greater than or equal to a preset switch intensity I_{sw} (I_{pc} on, binary
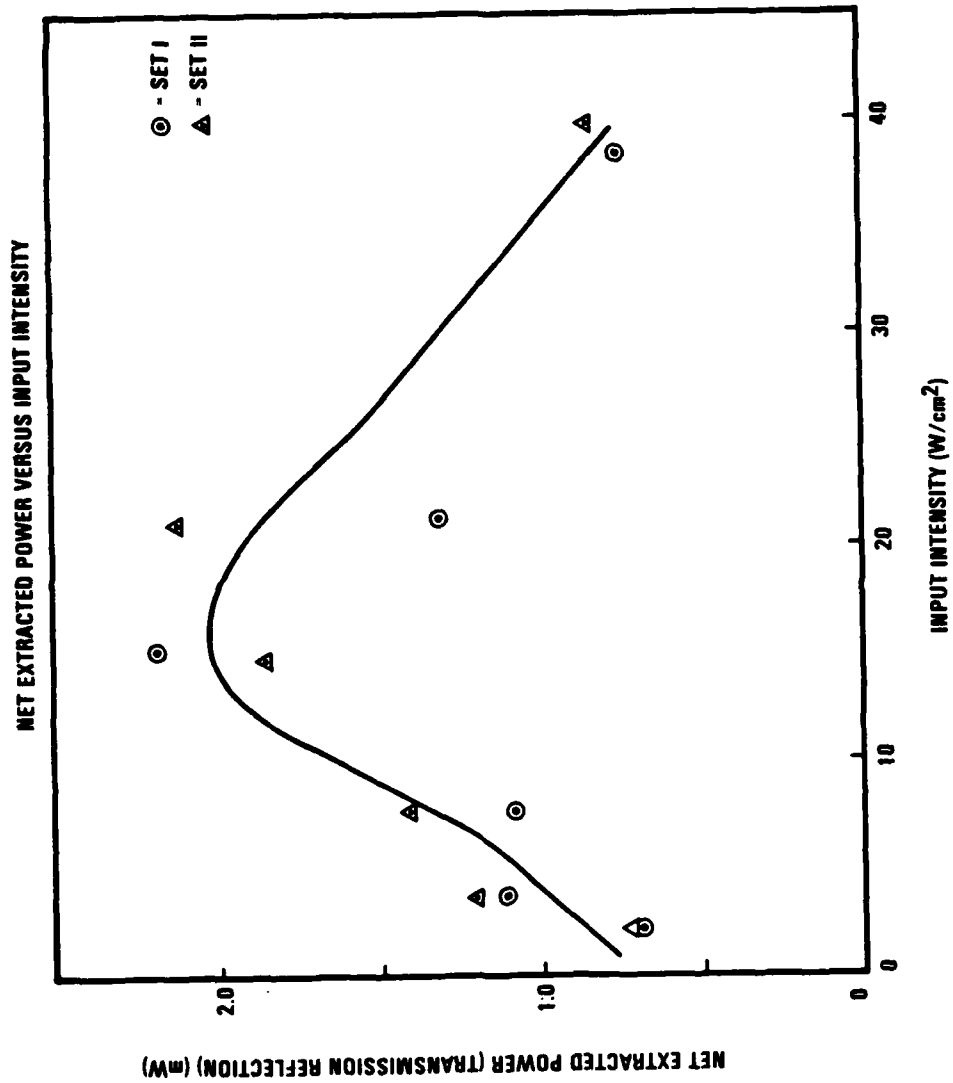
Figure 5-18. Net extracted power as a function of probe input intensity, indicating the possible contributions of other FWM processes when the probe input field is strong.

101

one), or less than I_{sw} (I_{pc} off, binary zero). For a valid "on" signal to be received, crosstalk noise in the FWM must not reduce I_{pc} below I_{sw}. To examine the noise problem, we start with Eqn. 5-4. Remember that this equation applies to a specific situation where the total pump intensity is 132 W/cm^2, the noise beam angle with the pump beam is 8.5 mrad, and the noise frequency is degenerate with the pump frequency. This estimate, therefore, is not general but, because of the small angle and frequency range retrictions, it may be regarded as a worst case calculation.

It is convenient to rewrite Eqn. 5-4 in the form,

$$I_{pc} - I_a \frac{I_p/I_b}{1 + (I_p + I_n)/I_b},$$

where

$$I_a - (A/B) I_{pump} - 31.0 \text{ W/cm}^2, \text{ and}$$
$$I_b - 1/B - 13.8 \text{ W/cm}^2.$$

From this expression, we solve for I_p:

$$I_p - \frac{I_{pc}(I_n + I_b)}{I_a - I_{pc}}, \tag{5-6}$$

We now ask how much the probe intensity must be increased to maintain an "on" signal in the presence of crosstalk noise. Without noise, the minimum probe intensity for an "on" signal is, from Eqn. 5-6,

$$I_p(0) - \frac{I_{sw} I_b}{I_a - I_{sw}};$$

and in the presence of noise it is

$$I_p(I_n) - \frac{I_{sw}(I_n + I_b)}{I_a - I_{sw}}.$$

The ratio is then

$$\frac{I_p(I_n)}{I_p(0)} - 1 + \frac{I_n}{I_b},$$

or

$$\frac{I_p(I_n)}{I_p(0)} - 1 + \frac{I_n(\text{W/cm}^2)}{13.8}.$$

We see that a noise intensity as large as 1.38 W/cm^2 would require a relatively insignificant 10% increase in the probe intensity to overcome

102

the intensity crosstalk. In addition, I_n is tightly restricted to be within about 8.5 mrad of the pump beam and degenerate with the FWM pump frequency, so the overall result is that intensity crosstalk will have little impact on field applications.

5.9 INTENSITY CROSSTALK SUMMARY

Simultaneous measurements of intensity crosstalk and noise-conjugate intensity versus the noise-pump angle indicate two principal crosstalk mechanisms, one having a sharp angular dependence and vanishing for noise-pump angles greater than about 10 mrad, the other being independent of angle. A strong correlation between the sharp, small-angle fall-offs of the crosstalk and the noise-conjugate intensity indicates that the angle-dependent crosstalk source is depletion of the pump beams to provide power for the generation of the noise-conjugate beam. The angle-independent source appears to be intensity saturation of the nonlinear susceptibility, that is, of the coupling between the pumps and the probe and probe-conjugate beams.

Experiments to determine the sensitivity of intensity crosstalk to the relative polarization directions of the pump, probe, and noise waves showed no discernable effect.

The probe-conjugate intensity was measured as a function of input probe intensity for fixed pump intensity. The curve was found to increase linearly for small probe intensity, and then to saturate for larger probe intensity. This behavior can also be explained as being due to a combination of pump depletion and intensity saturation of the nonlinear coupling. With two assumptions, this data was used to predict the results of a measurement of crosstalk vs. combined probe and noise intensities. The first assumption was that the probe and noise beams can be treated as parts of the same beam, i.e., that in the presence of noise, the probe-conjugate intensity bears the same relationship to the total (probe plus noise) input intensity that it does, in the absence of noise, to the input probe intensity alone. The second assumption was that the probe- and noise-conjugate beams can also be treated as parts of the same beam, i.e., that the ratio of probe-conjugate to noise-conjugate intensities is equal to the ratio of input probe to input noise intensities. The prediction and the experimental results agreed well, demonstrating that the same

mechanisms responsible for saturation of the probe-conjugate intensity vs. probe intensity curve are also responsible for intensity crosstalk. This agreement lends strong support to the hypothesis that crosstalk results principally from pump depletion and intensity saturation of the nonlinear coupling.

5.10 REFERENCES

5-1. A. Yariv, "Quantum Electronics, 2nd Edition," (John Wiley & Sons, New York, 1975), Chapter 8.

5-2. R.L. Abrams and R.C. Lind, "Degenerate Four-Wave Mixing in Absorbing Media," Optics Letters 2, 94-96 (1978).

5-3. W.P. Brown, "Absorption and Depletion Effects on Degenerate Four-Wave Mixing in Homogeneously Broadened Absorbers," J. Opt. Soc. Am. 73, 629-634 (1983).

6.0 SPATIAL CROSSTALK AND IMAGE FIDELITY

Decribed in this section are experiments to establish the importance
of another type of crosstalk involving transfer of spatial information
from one beam to another. Such crosstalk would be deleterious in
applications where image fidelity was important. The results presented
here indicate that spatial crosstalk arises only through the intensity
crosstalk mechanism described in Section 5, i.e., as predicted there is no
transfer of phase information from a noise beam to a signal beam if their
intensities are both small compared to the pump beams. The imaging FWM
experiments reported here also demonstrate excellent image fidelity. We
report a resolution of better than 14.3 line pairs per millimeter, the
highest line pair resolution obtained in Na vapor, and have demonstrated
faithful correction of a severe optical aberration.

6.1 Experimental Description

To establish the effects of spatial crosstalk on the contrast and
resolution of the probe conjugate image, initial imaging efforts
concentrated on phase conjugation of high frequency spatial images. The
arrangement in Figure 6-1 produced conjugate images with up to 14.3 line
pairs per millimeter resolution, limited to this figure by camera pixel
resolution and the available cw laser power. A 90.0 cm focal length
achromat (L1) was placed in the pump beam path to produce an 1100 μm
$1/e^2$ diameter pump cross section at the Na cell. Spatial information
was imprinted on the probe beam by introducing a standard USAF resolution
target (RT) into the probe beam path upstream of BS2. The spatially
imprinted probe beam was then focused into the Na cell at a pump-probe
angle of 25.3 mrad by a 20.0 cm focal length achromat (L2). The conjugate
image retraced the probe beam path (dotted line) and was reflected from
BS2 into the camera (C). Care was taken to optimize the positions of L2,
RT, and C to produce the highest resolution images.

6.2 Image Fidelity Results

Figure 6-2a is a photograph of a video monitor which displayed a
portion of the resolution target used in the image resolution experiment.
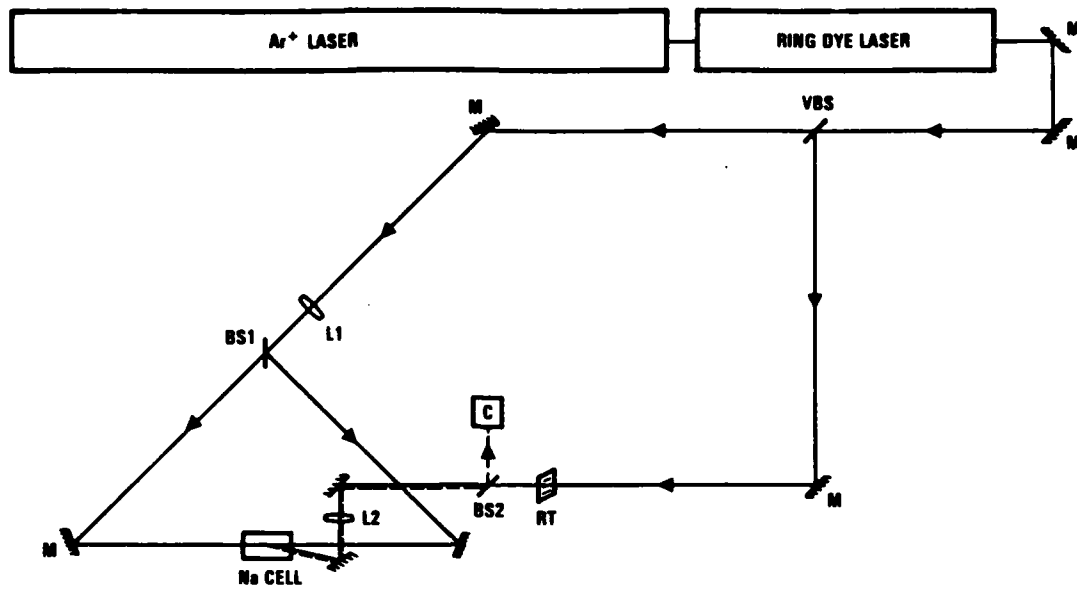
Figure 6-1. Image resolution experiment.

b.

a.
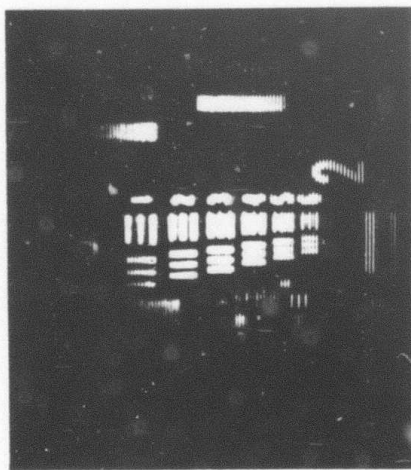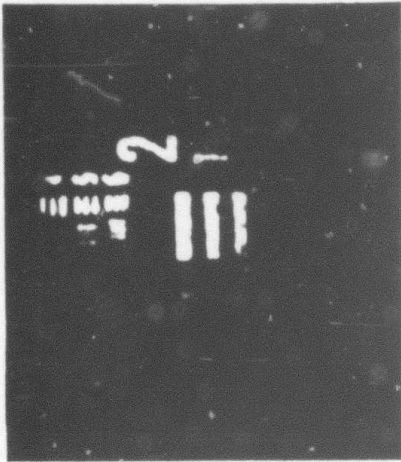
Figure 6-2. Camera resolution test, (a). Best resolution conjugate image, (b). Both images show resolution greater than 14.3 line pairs/mm.

The image for Figure 6-2a was transferred from the resolution target to the camera detector plane by 1:1 imaging optics to test the spatial frequency resolution limit imposed by the camera pixel spacing. The resolution portrayed in the photograph is unavoidably degraded compared to the actual resolution obtained due to the display resolution of the video monitor. However, video recording (as opposed to direct photographic recording) proved to be the most efficient and convenient means of characterizing the imaging results because of its real time processing capabilities in the determination of focal plane location, intensity levels, and intensity uniformity. Figure 6-2b is a photograph of the same video monitor displaying the highest resolution conjugate image that was recorded. The resolution of the two photographs is seen to be comparable indicating that pixel separation in the camera detector plane probably was a limiting factor in the recording of images with higher spatial frequencies.

A second factor which affected spatial frequency resolution was the effective aperture of the phase-conjugate mirror determined by the pump beam cross section at the Na cell. This diameter in turn was determined by the available laser power from the CW dye laser, with a compromise between pump intensity for reflectivity and pump diameter for image fidelity being necessary. Employing the shortest focal length achromat practical for L2 (focal length = 20.0 cm), L1 was translated along the common pump beam path to produce the highest resolution images possible while maintaining acceptable contrast levels. The corresponding pump beam $1/e^2$ diameter was 1100 μm. The effect of this aperture size was assessed by focussing the image bearing probe beam through a 1100 μm hard aperture, and comparing the transmitted image with the conjugate image reflected off of the sodium phase conjugate mirror. The phase-conjugate image reflected off of the 1100 μm "mirror" formed by the pump beams was noticeably better in fidelity than the image transmitted through the hard aperture. This suggests that there is enough intensity in the wings of the pump beams to conjugate the image beam efficiently, i.e., the phase-conjugate aperture is a soft one and larger than the $1/e^2$ pump beam diameter at the pump powers used in these experiments.

Typical reflectivities obtained with 1100 μm pump beams in the

imaging experiments were 12-18%, with excellent conjugate fidelity evidenced by the necessity of placing the resolution target (RT) and camera (C) equidistant from BS2 (Fig. 6-1). If these distances were not the case, the camera was not at the conjugate image plane, resulting in the conjugate return image being detected out of focus. The excellent fidelity was also established by testing image quality with an optical aberrator in the probe path.

The aberration correction capability of the four wave mixing cell was demonstrated with the apparatus in Fig. 6-3. Initially, a standard USAF target image (in this case, the numeral 4) was imprinted on the probe beam by the image plate (IP) and focused into the Na cell by L2. The conjugate image-bearing beam (dotted line) retraced the input probe path and was reflected off the beamsplitter to the camera (C). A second camera was employed to monitor the quality of the transmitted image which was reflected from two $\lambda/20$ turning mirrors and focused onto the detector plane of the transmission camera by achromat L3.

Photographs of the unaberrated phase conjugate image and transmitted image are shown in Figures 6-4a and 6-4b, respectively. Although the transmissive aperture of the four wave mixing cell is significantly larger than the phase conjugating aperture (note the edges of the bars are absent in the conjugate image photograph), the central portion of the transmitted image served as a good input image standard. After recording the unaberrated images, a 65 λ aberrator plate (A) was inserted into the input probe image path so that the distorted phase conjugated image returned through the aberrator plate before reaching the camera. The resulting photographs of the aberrated conjugate image (Fig. 6-4c) and corresponding transmitted image (Fig. 6-4d) are displayed below their unaberrated counterparts. The ability of the four wave mixing cell to correct for significant image distortion is then made apparent by comparison of Fig. 6-4a, 6-4c, and 6-4d. The open gap at the top of the target "4" is conservatively estimated to represent a 10 line pair per millimeter spacing; therefore, the present system is, at a minimum, capable of this degree of resolution through a 65 wave aberration.

6.3 Spatial Crosstalk Results

After good image resolution was achieved with fairly high spatial
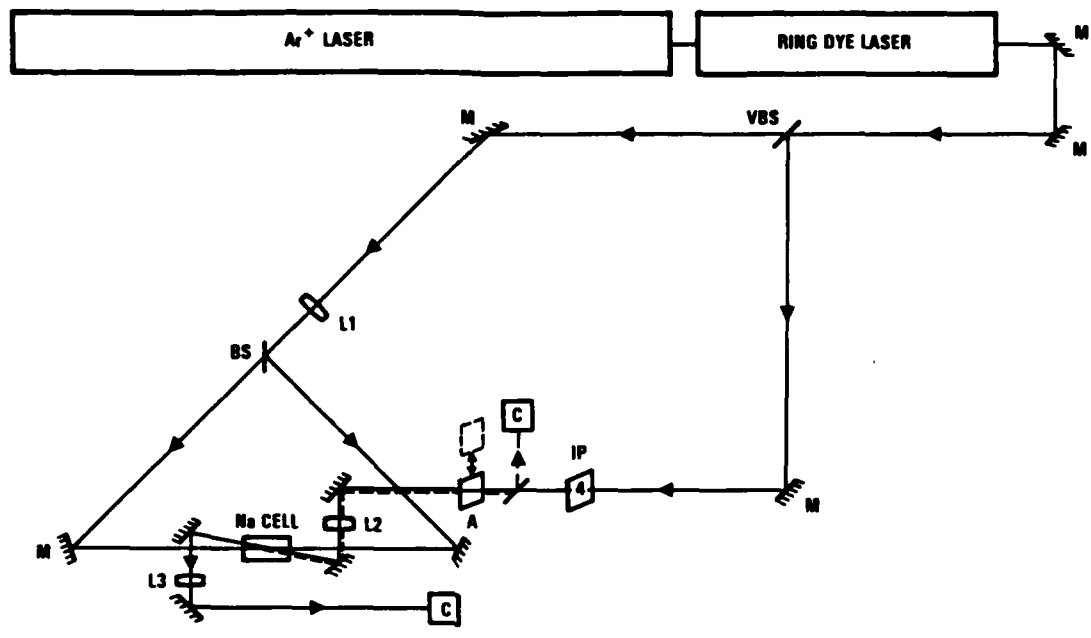
Figure 6-3.   Aberration Correction Experiment

110

Transmitted probe image

Phase conjugate image

No Aberrator

Severe Aberrator

a.
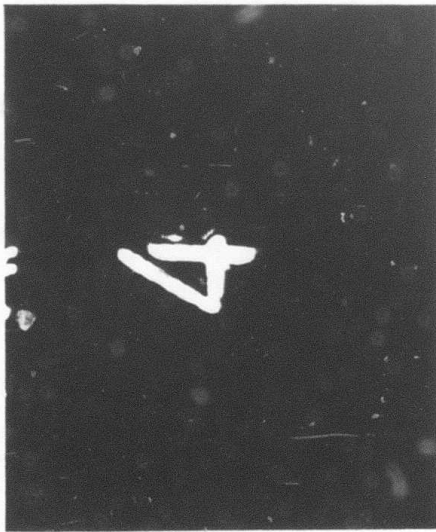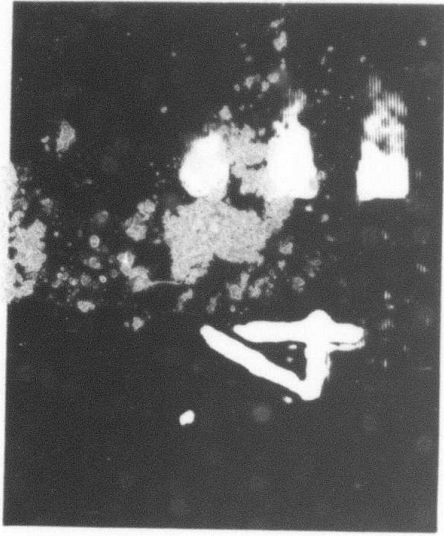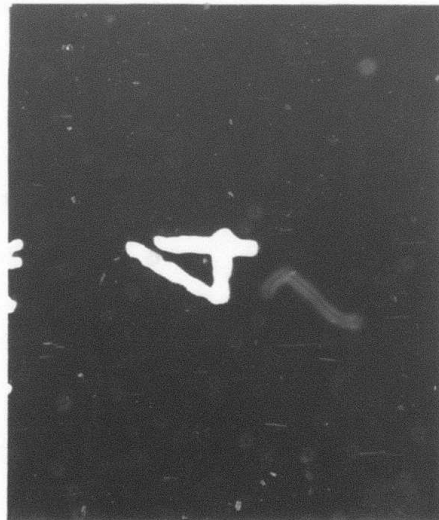
b.
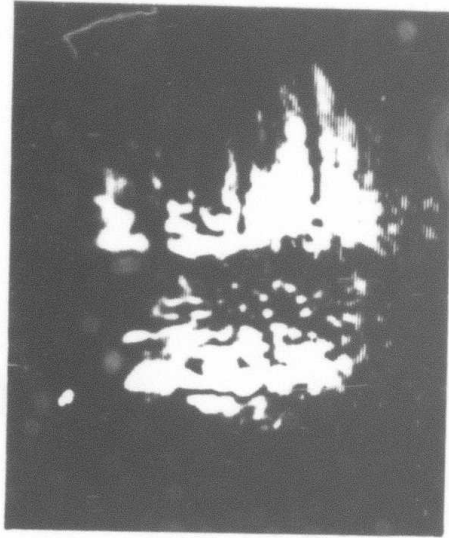
c.

d.

Figure 6-4. Aberration correction experimental results. a) phase conjugate image with no aberrator in propagation path, b) transmitted probe image with no aberrator, c) phase conjugate image with 65 λ aberrator in place, d) transmitted probe image with aberrator in place.

111

frequency targets, spatial crosstalk experiments were undertaken to quantify reductions in image contrast and edge definition in the presence of noise beams that have spatial intensity distributions that are Gaussian or image-bearing . For a Gaussian noise source, modifications to the basic imaging arrangement of Fig. 6-1 included the addition of a variable beamsplitter (VBS2, Fig. 6-5) and a 50% beamsplitter (BS3) to produce a variable intensity noise beam which was separately focused into the Na cell at a pump-noise angle of 8.1 mrad by achromat L3. The noise beam conjugate (dotted line) retraced the noise beam path and was detected by a silicon photodiode (PD) through BS3. Maximization of the noise conjugate by adjustment of elements L3 and BS3 insured optimum probe-noise overlap at the Na cell and was essential for consistent spatial crosstalk results. The total power allocated to the probe and noise beams by VBS1 could not exceed 6-10 mW without sacrificing pump beam power.

Quantification of the changes in probe conjugate image quality due to the presence of Gaussian or image-bearing noise fields was accomplished through the use of video digitization of the recorded conjugate images.Fig. 6-6a and 6-6b are representative of the digital output from two cross section samples of a 2.83 line pair per millimeter three bar image recorded in the absence of the noise beam. Due to the comparable dimensions of the test target and probe beam diameter, the center bar of the three bar conjugate image was somewhat more intense than the outer two bars. However, good contrast and distinct boundries are apparent from the light-to-dark values and well-defined light and dark regions are obtained with a 4 mW input probe image. In the presence of a 2 mW Gaussian noise source at approximately one-third the probe beam input angle (8.1 mrad for the Gaussian noise beam versus 25.3 mrad for the image-bearing probe beam), the same cross section samples (Fig. 6-7a and 6-7b) show only a 15% average decrease in peak intensity with no detectable degradation in edge sharpness.

Since even at small input angles, a Gaussian cross section noise beam had little effect on probe conjugate image quality, the effects of an image-bearing noise beam were studied with the experimental layout in Fig. 6-8. A three bar test target of identical spatial frequency but orthogonal orientation with respect to the probe target (see Fig. 6-8) was then inserted into the noise beam path and focused into the Na cell with

Ar⁺ LASER

RING DYE LASER

M

M

VBS1

M

BS1 L1

C

RT

PROBE VBS2

BS2

L2

NOISE BS3 PD

M

Na CELL L3
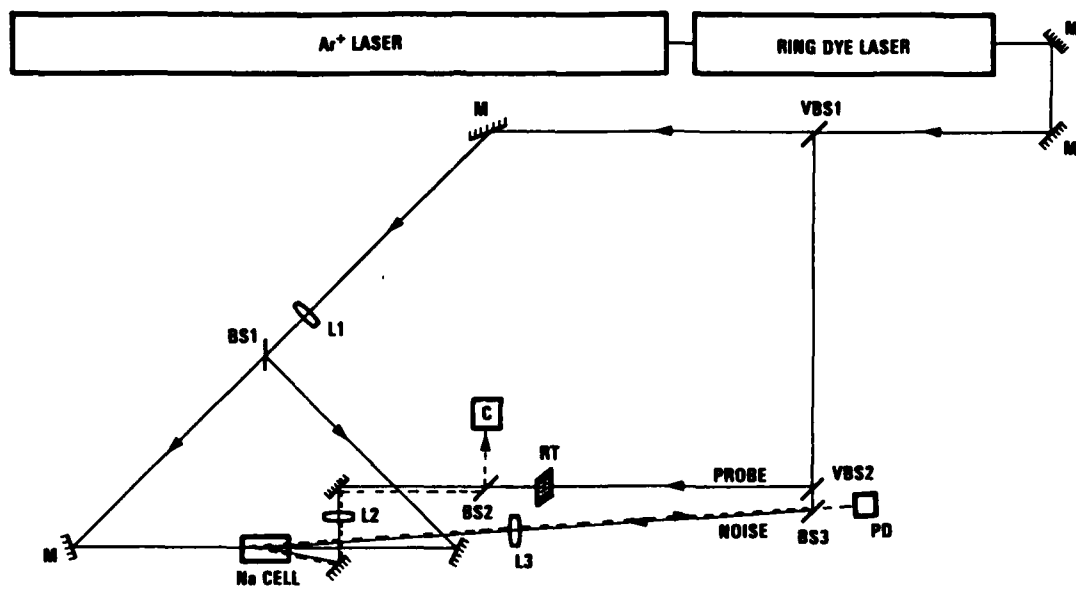
Figure 6-5. Spatial crosstalk experiment –
Noise beam without image.

COLUMN SLICE

INTEGER
COUNTS

240
200
160
120
80
40
0

0   PIXEL # 50   100   150   200   250

(a)

COLUMN SLICE

INTEGER
COUNTS

240
200
160
120
80
40
0

0   PIXEL # 50   100   150   200   250
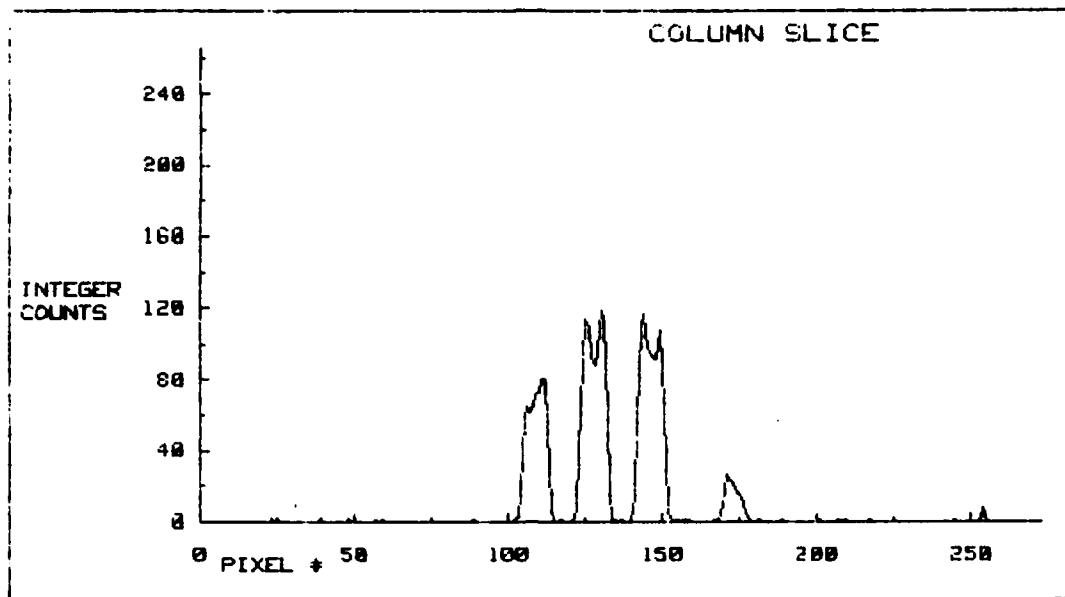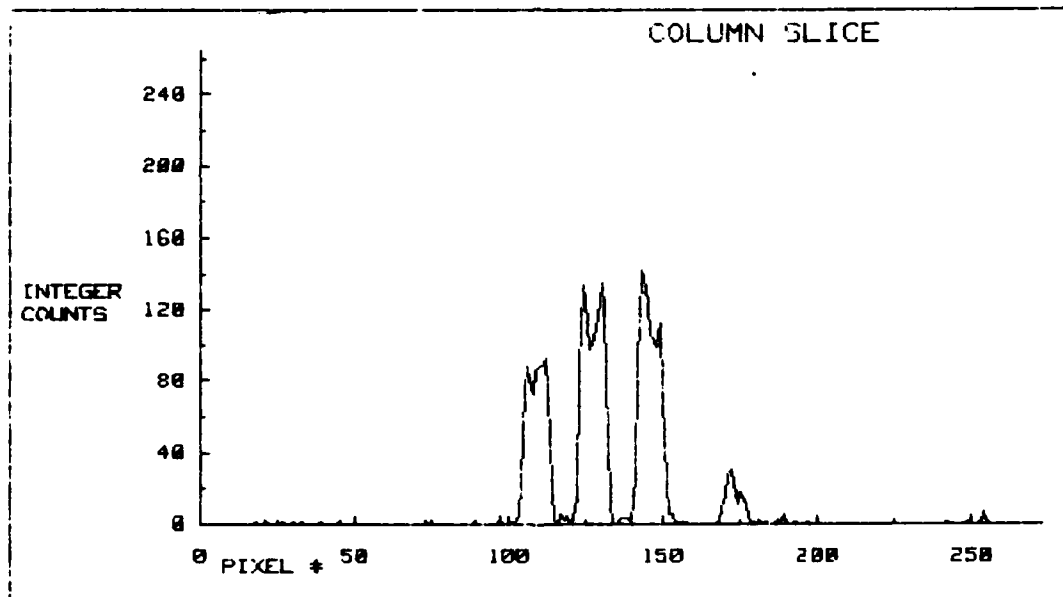
(b)

NOISE = 2 mW

PROBE = 4 mW

Figure 6-6.   Digitized cross sections of a three bar image
without Gaussian noise beam.

114

COLUMN SLICE

(a)

COLUMN SLICE
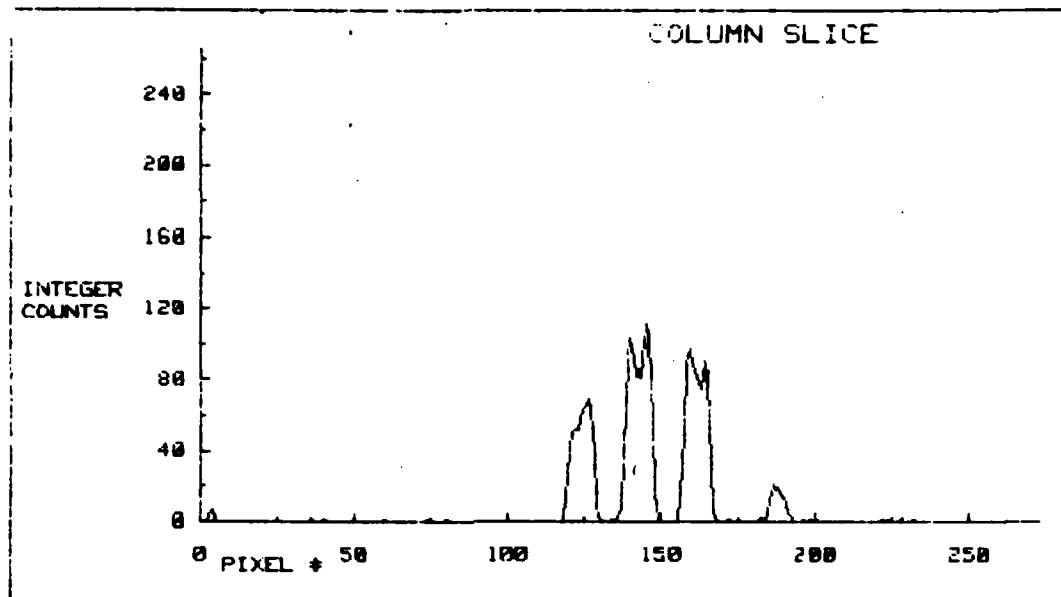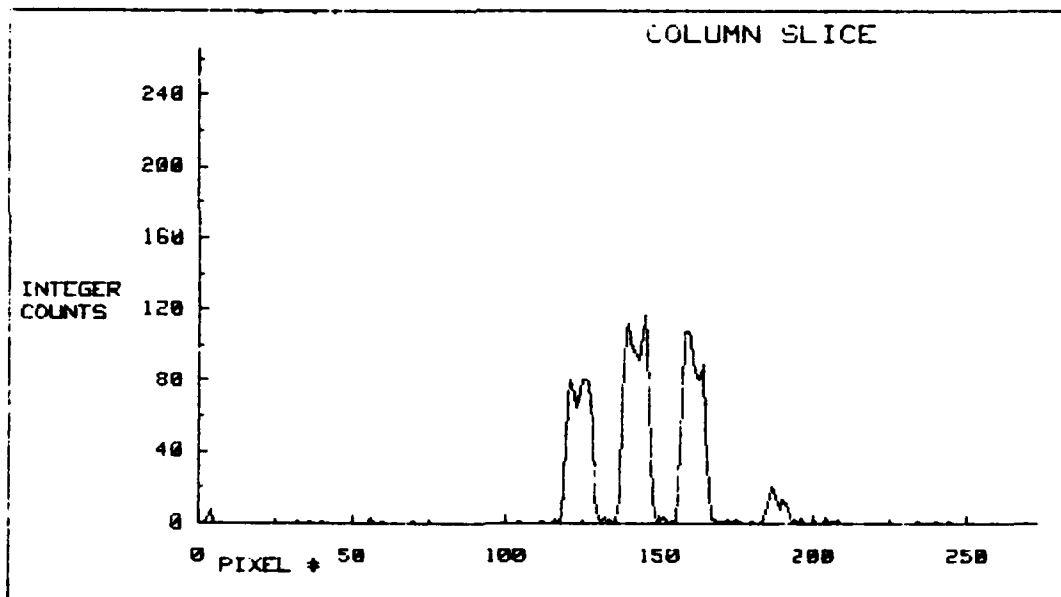
(b)

Figure 6-7 Digitized cross sections of a three bar image in
the presence of a Gaussian noise beam.

115
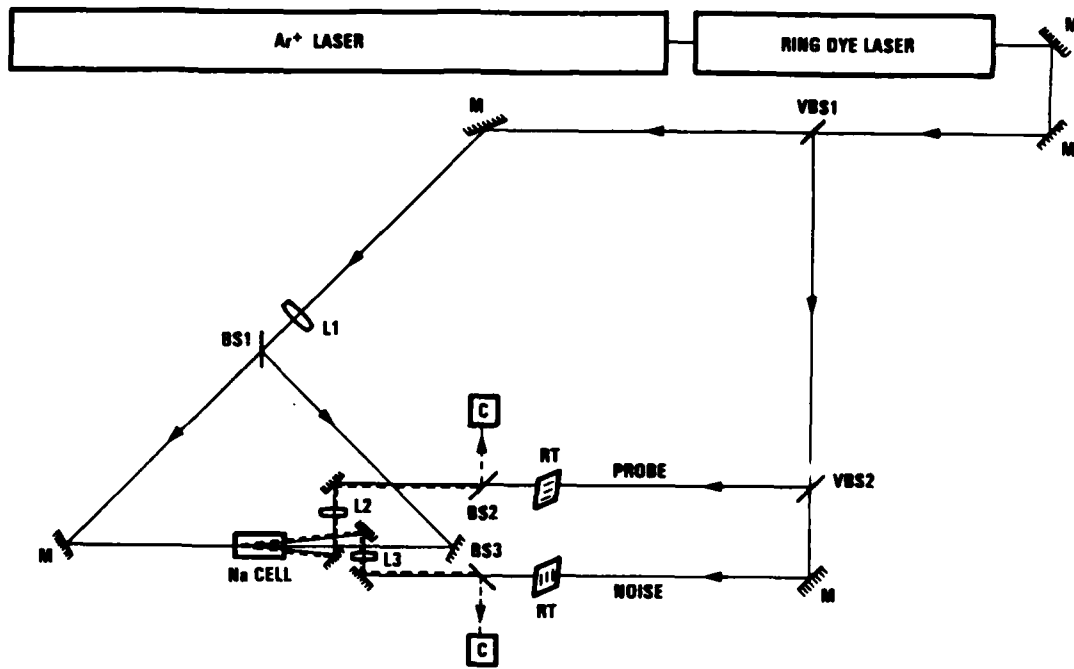
Figure 6-8. Spatial crosstalk experiment –
Noise beam with image.

achromat L3. All optical elements in the probe and noise beam paths were identical so that the variable beamsplitter (VBS2) directly controlled the probe:noise intensity ratio at the cell. In addition, a second camera was positioned to record the quality and intensity of the noise beam conjugate image in order to insure that both probe and noise beams were conjugated from the same region in the conjugate reflecting aperture. Each of the input beams was focused separately into the cell to produce the most homogeneously illuminated conjugate image at their respective cameras and the images were recorded. Both beams were then unblocked and the probe conjugate image recorded. The result of this sequence where the probe:noise intensity ratio was approximately 1:6 is displayed in the photographs of Fig. 6-9a-c and in the digitized cross sections of Fig. 6-10a and 6-10b. The average peak intensity is reduced approximately 46% as a result of the presence of the noise image; however, as in the case of a Gaussian noise field, edge definition is not compromised even by a six-fold intense noise image.

The spatial crosstalk data can be understood in terms of the intensity crosstalk mechanism described in Section 5 if one considers the spatial frequency content of the Fourier transform of the probe and noise images. Since the interaction occurs at or near the focal planes of the lenses that focus the probe and noise beams into the sodium cell, the interfering spatial images are the Fourier transforms of the images originally imprinted on the beams. Fig. 6-11a and 6-11b are photographs of the Fourier transforms of the probe and noise images with an 1100 μm diameter aperture for comparison which simulates the $1/e^2$ pump beam diameter at the Na cell. Intensity crosstalk can occur in regions of the Fourier plane where there is significant noise beam intensity, which because of its localized distribution, results in spatially varying crosstalk effect.

This localized spatial crosstalk is strongest precisely where the low spatial frequency (e.g. contrast) components of the probe image are located in the sodium FWM cell. Most of the power in both the probe and noise beams is concentrated inside the first Airey disk, which in transform space contains the low spatial frequency components of the original patterns. As a result, the intensity of these components is reduced, leading to a loss of image contrast. Higher frequency Fourier

117

Figure 6-9. Spatial crosstalk results with an image-bearing noise beam.
(a) Probe conjugate image without noise.
(b) Noise conjugate image without probe.
(c) Probe conjugate image with noise.

118
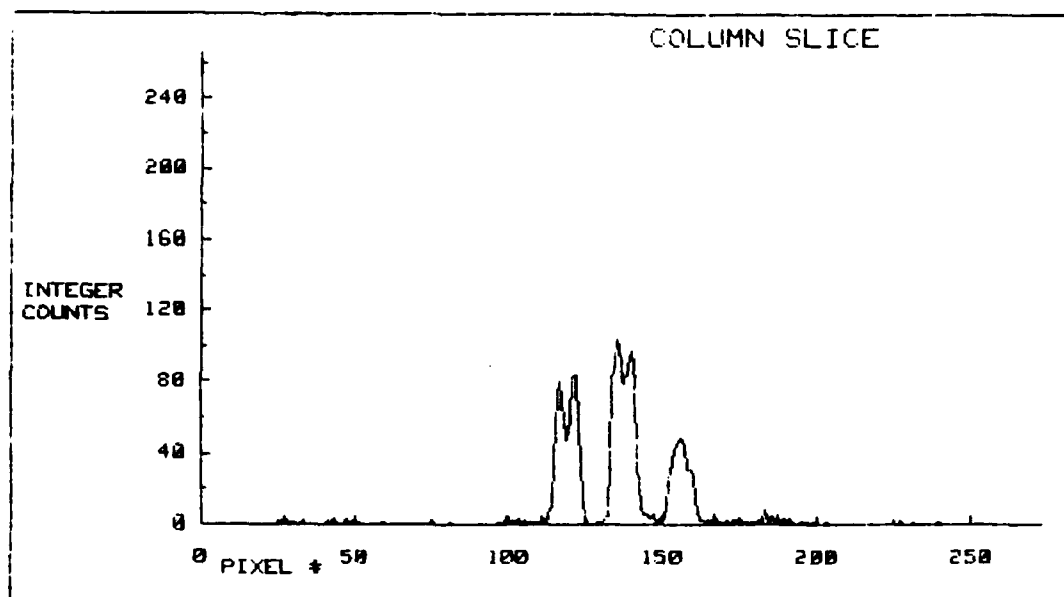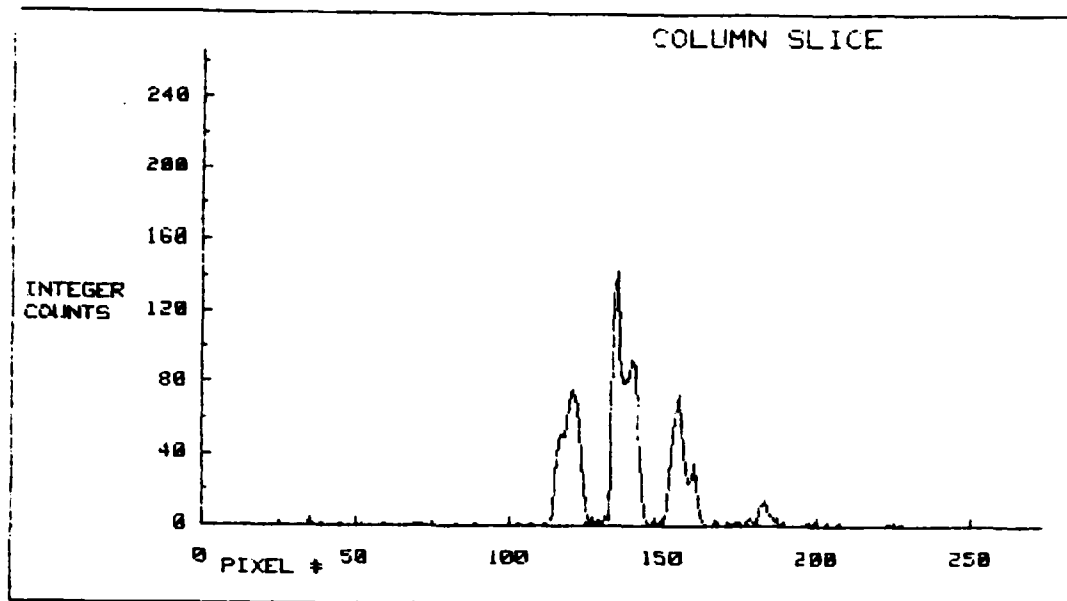
NOISE = 6 mW

PROBE = 1 mW

Figure 6-10(a). Digitized cross sections of probe conjugate
image without noise image.

COLUMN SLICE

INTEGER
COUNTS

0 PIXEL # 50   100   150   200   250

COLUMN SLICE

INTEGER
COUNTS

0 PIXEL # 50   100   150   200   250
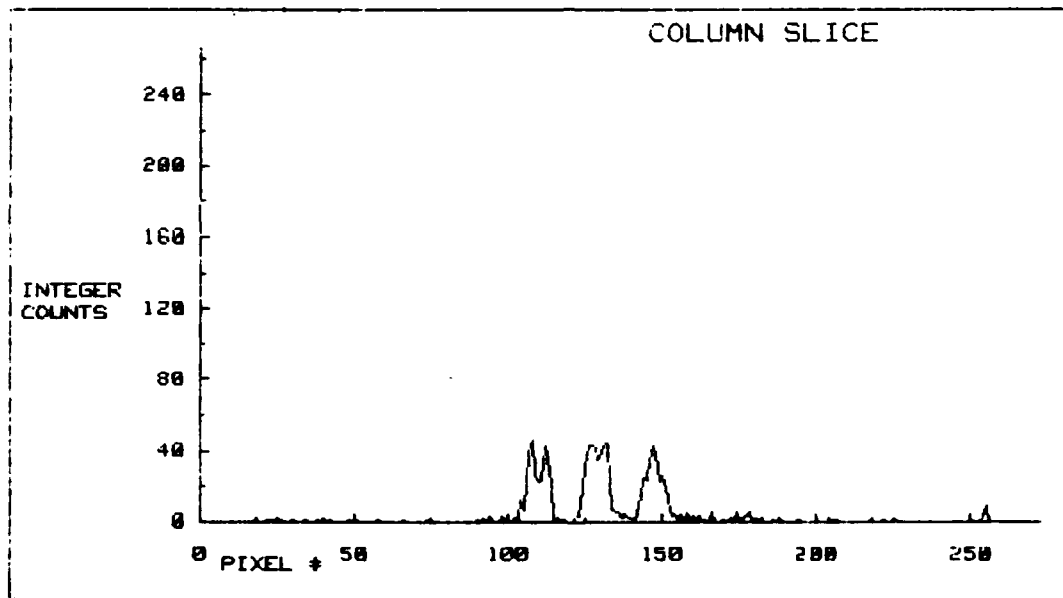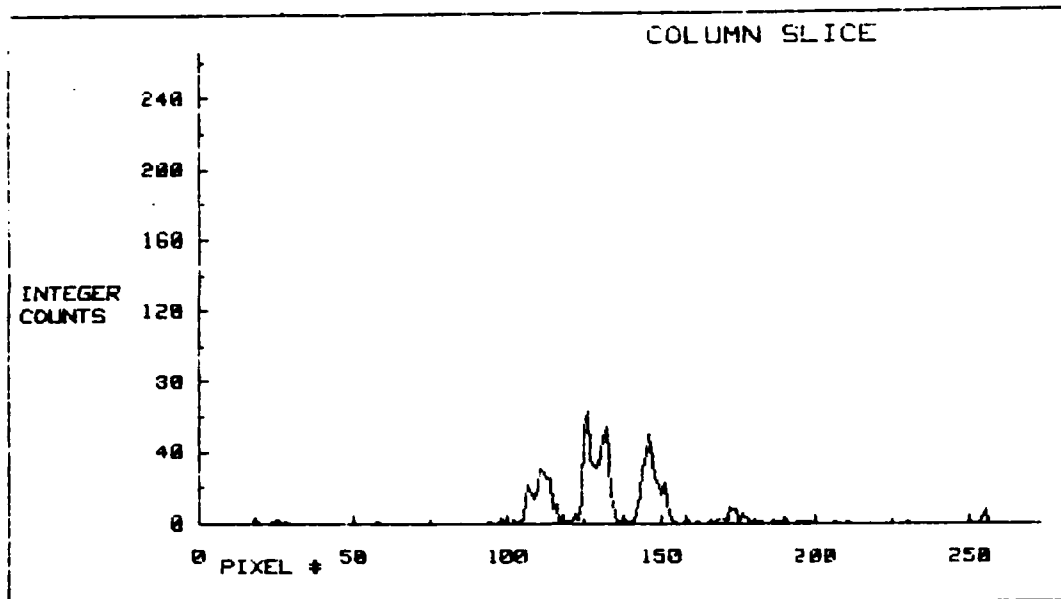
Figure 6-10(b). Digitized cross sections of probe conjugate
image with noise image.
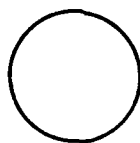
Figure 6-11. Fourier transform of probe (a) and noise (b) images recorded at the Na cell. Shown for reference is the relative size of pump beam $1/e^2$ diameter, which acted as a soft aperture in the FWM imaging experiments.

1100 μm
aperture

a.

b.

components, which define the edge boundaries, occur in the outer wings of the patterns in Fig. 6-11 and carry only a small fraction of the intensity of the original image. Therefore, the higher order components for both the probe and noise images are much less likely to be involved with pump beam depletion and coupling saturation, and are conjugated independently of one another. Thus edge definition in the conjugate image is not expected to be impacted, a result consistent with the observed "dimming" without loss of edge definition of the conjugate image in the far field. The preservation or effective enhancement of edges is important for target image recognition.

6.4 Summary

Experimental results have shown that excellent image quality can be achieved using a Na vapor FWM, even when significant optical aberrations are present in the propagation path. The resolution obtained was essentially instrument-limited; in practice, the resolution will be determined by the soft aperture defined by the pump beam diameter. In our experiments, this diameter was chosen as a compromise between pump intensity and effective aperture size, with resulting reflectivities in the range of 10-25 %. Under these conditions, the impact of self-action effects mentioned in Section 4 were negligible; such effects may adversely affect image quality under high reflectivity conditions.

Spatial crosstalk between a noise and probe beam was measured when images were imprinted on the probe beam only, and when both beams were image-bearing. In both cases, the result was a relatively uniform reduction in intensity of the probe conjugate image, i.e., a decrease in image contrast, but there was no measurable loss of resolution. The spatial crosstalk effect may be explained as localized intensity crosstalk due to saturation of the FWM reflectivity in regions where noise beam intensity in the FWM cell is largest. This tends to be in regions where low spatial frequency components of the probe image Fourier transform are located, so the effect is primarily a loss of image contrast with little loss of edge definition.

7.0 FWM CODE DEVELOPMENT

The strategy for FWM code development was to start with a simple one-dimensional model of FWM in a Kerr medium, which could be checked against simple analytical expressions for reflectivity, and then to extend this model to resonantly enhanced media and to a two-dimensional wave optics model. The choice of models developed was driven by the issues important for the missions being considered. At the beginning of the program, we were considering use of pulsed lasers for FWM; this indicated the desirability of time-dependent models. The use of pulsed lasers was abandoned when the difficulty of meeting timing requirements over unknown mission distances became obvious. However, the use of "time-dependent" numerical models was retained for their computational advantages in two-dimensional problems. Although the equations for the one-dimensional model can be solved by a variety of numerical techniques, such as Runge Kutta or Adams Predictor corrector methods, these techniques are not applicable to a two-dimensional model that includes transverse derivatives. The two major approaches for solving the 2D steady-state problem are iterating from an initial guess or approximation, or solving the time dependent problem until steady-state is reached. Previous experience in solving 2D coupled, nonlinear equations by iteration has shown this technique to be exceedingly troublesome and susceptible to chaotic behavior (induced by the numerical procedure, not by the physics). For this reason, the 2D FWM code uses a "time-dependent" algorithm. A 1D precursor to the 2D code was also written, using the same "time dependent" algorithm. This 1D code allows us to define the region of validity of the 2D code and to determine the input parameters needed to produce accurate predictions of FWM reflectivity. It was also found useful to have a non-time-dependent version of the 1D code. This code used standard numerical techniques to solve for the steady-state reflectivity, and in general, ran faster than the time-dependent code.

7.1 ONE-DIMENSIONAL DFWM MODELS

Early theoretical treatments of DFWM in resonant media had a very limited range of validity because the effects of pump beam absorption and depletion were neglected (Ref. 7-1). However, in cases where the largest DFWM signals are obtained there is a significant amount of pump absorption (~50% in our experiments). The inclusion of pump absorption into the

123

differential equations which describe the evolution of the four complex field amplitudes results in a set of equations which must be solved numerically. This problem has been solved previously and the numerical results of certain sample cases displayed (Ref. 7-2, 7-3). As TRW is interested in examining DFWM over a large parameter space, a similar computer code has been developed to solve these coupled field equations numerically.

7.1.1. CW Degenerate FWM in Resonant Media

Two different 1D models of DFWM have been developed at TRW. The version to be discussed first, known as 1DCW, is applicable to DFWM in homogeneously-broadened resonant media using a CW narrowband laser. The coupled field equations are solved in steady state. The relevant coupled field equations are shown and discussed in Appendix A. Briefly, in the small signal limit where the forward pump beam (I_f) and the backward pump beam (I_b) are much larger than both the amplified signal beam (I_s) and the phase conjugate intensity (I_c) throughout the entire sample, the four pump equations (two amplitude equations, two phase equations) become decoupled from the four signal equations. An analytical transcendental expression for the intensity distribution of the two counterpropagating pump beams can then be obtained and used to solve the pump phase and amplitude equations (Ref. 7-3). Finally, these solutions for the spatial dependence of the pump waves are used to determine the spatial dependence of the nonconstant coefficients appearing in the four coupled signal and conjugate equations. These four equations have been solved simultaneously using three different numerical methods. All three methods give the same results to many significant figures. Two of the methods are noniterative in nature, and rely upon the fact that in the low signal limit the DFWM reflectivity is independent of the incident signal beam intensity. In these two methods, an arbitrary value is assigned to the amplified transmitted signal beam intensity I_s at z-L (L is the length of the nonlinear medium, see Figure A-1 in Appendix A). The problem simplifies to an initial value problem since all eight variables are now known at the same location (z-L). The equations are then integrated from z-L to z-0. In this way the final conjugate intensity and the value of the initial signal necessary to produce such a conjugate intensity are obtained. The ratio of these two quantities is the

124

reflectivity. The two noniterative methods used to integrate the equations were a Runge Kutta-Verner fifth and sixth order method and a variable order Adams predictor corrector method (Ref. 7-4). Identical results were obtained with both methods to many significant figures.

As a further check on the validity of the numerical calculations, a subroutine capable of solving a system of differential equations with boundary conditions specified at two different points was employed. The routine uses a variable order, variable step size finite difference method with deferred corrections (Ref. 7-5). As mentioned above, all three methods gave identical results.

The plots of the DFWM reflectivity versus the line center absorption coefficient (α_o) shown in Figure 7-1 are numerical solutions obtained in Ref. 7-3. The symbols plotted on the figure are the numerical results obtained by each of the three methods described above. In most regions of the figure the two results agree very well. However, discrepancies exist in some regions, particularly when the reflectivity becomes large. We believe these differences are due to the fact that the numerical integration used in Ref. 7-3 was not sufficiently accurate in this region (Ref. 7-6).

7.1.2 1-D Pulsed Degenerate FWM Mixing in Resonant or Kerr-like Media

The other 1D DFWM code which we have developed was designed to be a precursor of the two dimensional (2D) code so that all of the formalism developed for the 1D code could be easily transferred to the 2D code. This 1D code, known as 1DP, has a time dependent formalism which enables it to do both pulsed and CW calculations. Eight coupled equations for the amplitude and phase of each of the four fields are solved and include the effects of pump depletion and absorption. The 1DP code has models for two types of FWM media: Kerr-like and resonantly enhanced. The equations for the resonantly enhanced version are given in Appendix A: the Kerr-like equations are similar and are given in Ref. 7-7. The model of Kerr-like media includes nonsaturable background losses (e.g. scattering) and is valid for strong signal intensities. The model of resonantly enhanced FWM is based on the two-level model of Brown (Ref. 7-2) and includes saturable absorption and dispersion. For the resonant FWM media, the eight equations solved here are similar to those discussed above in Section 7.1.1., but a different method of solution is used. Only five of the

125
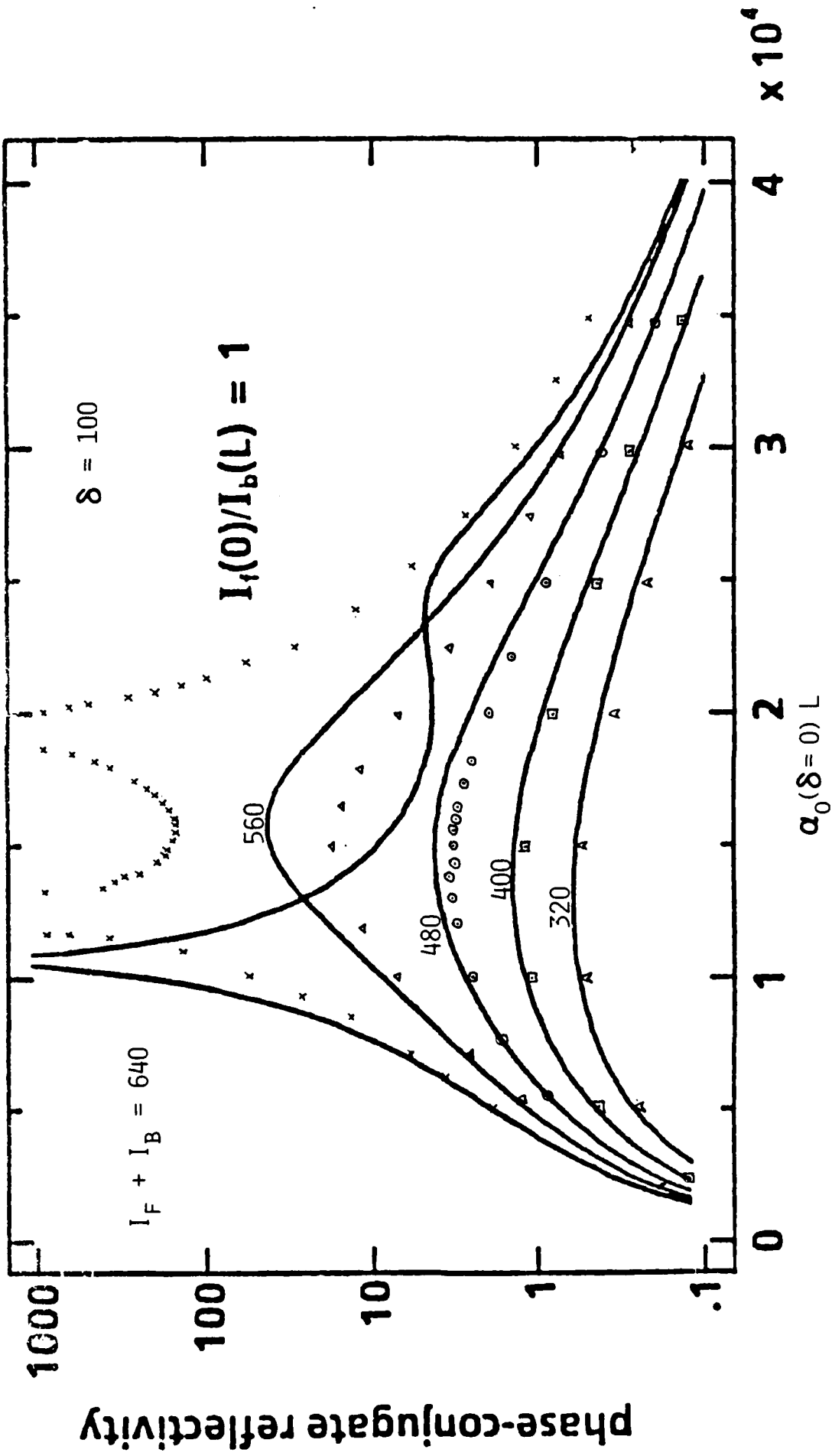
Figure 7-1. Comparison of the 1DCW code (symbols) with that of Ref. 7-3 (solid lines).

eight equations need to be solved simultaneously in order to obtain the magnitude of the phase conjugate reflectivity. However, in the 2D DFWM model (Section 7.2) which was developed at TRW in order to examine the influence of various FWM parameters on the fidelity of the phase conjugation, it is necessary to solve all eight equations. In order to enable the results of the 1DP model to be directly transferable to the 2D model all eight equations are solved in this 1D case. Similar statements apply to the Optical Kerr version of this 1DP code except that the equations, taken from Ref. 7-7, rigorously include the effects of pump depletion. In contrast, in the resonant 1DP model pump and signal absorption are quantitatively accounted for, whereas the treatment of pump depletion is only qualitative since analytical expressions for the coupling coefficients at high signal intensity have not been formulated and numerical evaluation requires prohibitive computer capacity. The coupling coefficients for high signal intensity have been approximately formulated for the case of cross polarized pumps, enabling the resonant 1DP code to give qualitative results for pump depletion.

Figure 7-2 shows some sample results for an optical Kerr-like medium. In Part A of the figure the DFWM is performed with a CW laser with a pump intensity of 100 MW/cm^2 and a medium length of 10 cm. The curves in the figure plot the intensities of the four light beams as a function of position in the FWM medium. Under these intense pumping conditions the gain experienced by the signal and the conjugate signal is so large that these signals become comparable in magnitude to the pump beams. Due to conservation of energy the pump beams are largely depleted. In part B of the figure a pulsed laser of 1 nsec duration (30 cm in length) is used to perform the FWM. A square pulse shape has been used. Once gain, large signals are obtained and pump depletion occurs. The length of the FWM medium is shorter than the laser pulse lengths. As a result, the front part of the counterpropagating pump pulses are depleted while the rear parts are not because they experience less gain since they do not overlap throughout the entire medium. This effect gives rise to the odd intensity distribution shown in the figure.

7.2 2D CODE FOR CW OR PULSED DFWM IN RESONANT OR KERR-LIKE MEDIA

Many analytical and numerical techniques have been developed in recent years to study optical phase conjugation via backward four-wave

127
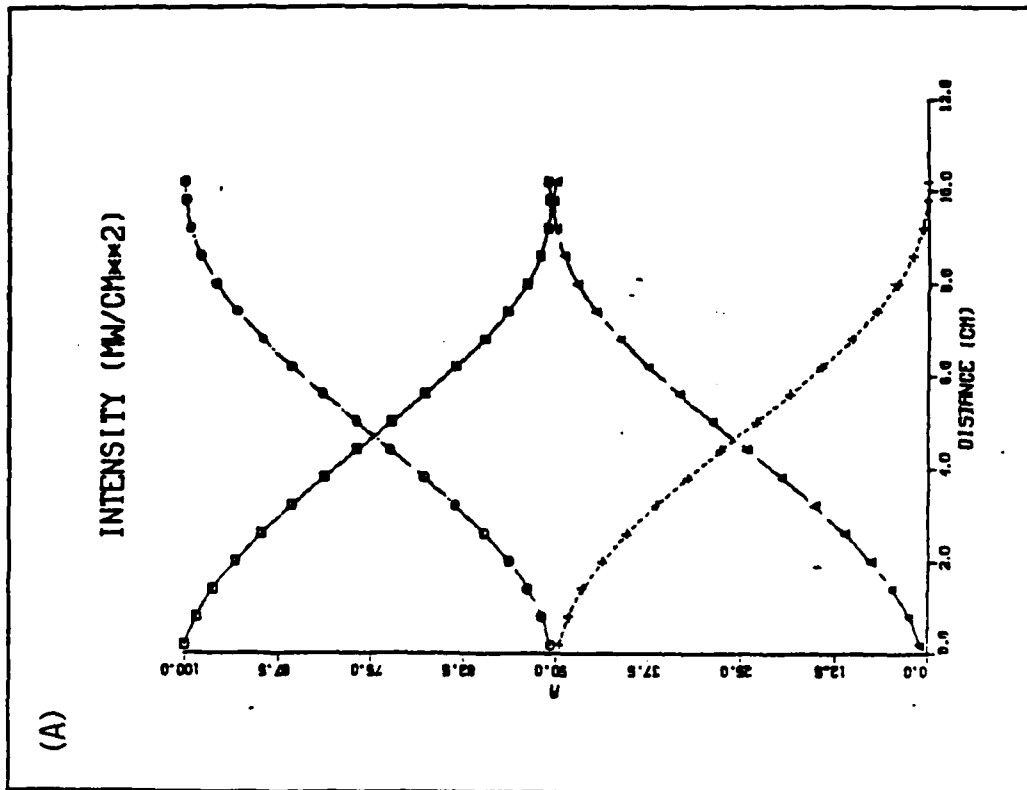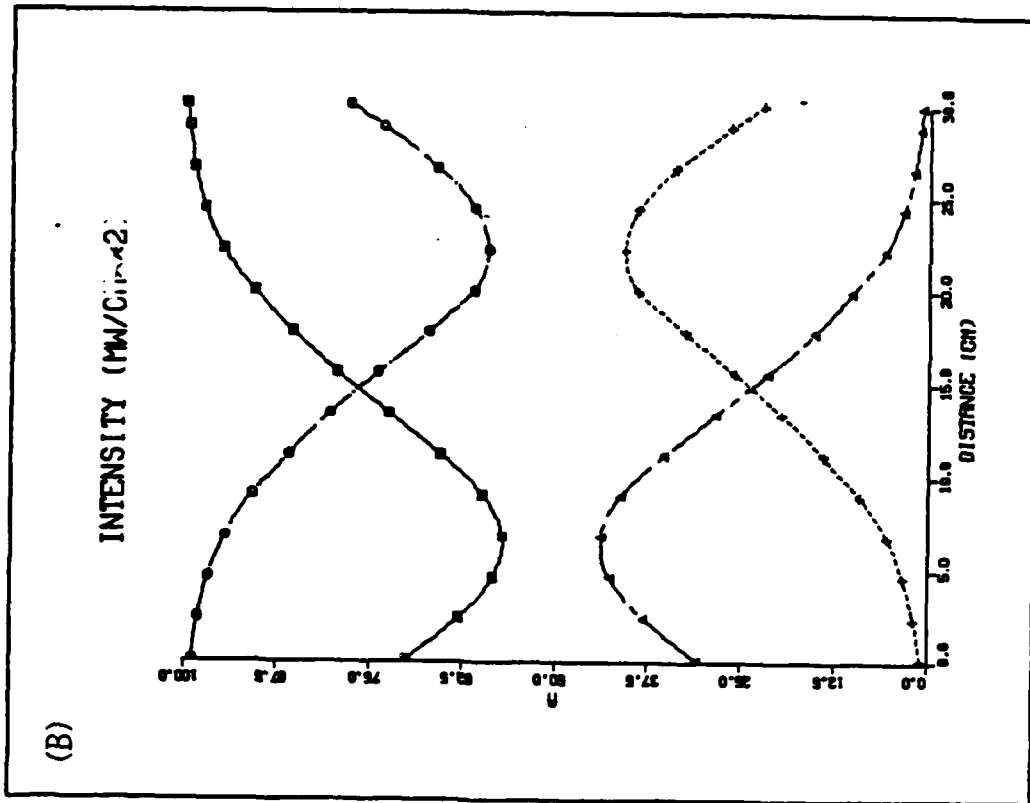
Figure 7-2. Results of the 1DP code for an optical Kerr-like medium.

128

mixing. So far, the numerical studies are limited only to one-dimensional analysis of the effect in steady state (Ref. 7-2, 7-3, 7-7). Reflectivity is the only resulting quantity. Other important features such as beam misalignment, self-focusing and phase conjugation fidelity have remained unexplored. These features can only be studied by including at least one additional transverse dimension to account for the intensity and phase variation of the fields. For this purpose, a two-dimensional code simulating four-wave mixing has been developed at TRW. The original version of the code, which modeled FWM in a Kerr medium, was developed on the Free Electron Laser Resonator Development Program (Ref. 7-8). The extension to resonantly enhanced media was performed on NLOT. The code follows the actual time history of wave interaction in the nonlinear medium and is capable of simulating the mixing process with both finite-length pulses and CW conditions.

The notation used here for the backward four-wave mixing configuration is as follows. Beam 1 and 2 are the colinear pump beams propagating in opposite directions. Beam 3 is the signal beam incident at a very small angle with respect to beam 1. The plane defined by these three beams is the two-dimensional working space for the system, and it is assumed that there is no variation of physical parameters in the direction normal to this plane. Usually, direction z is defined as the line bisecting the angle between beam 1 and 3 (Figure 7-3), although the
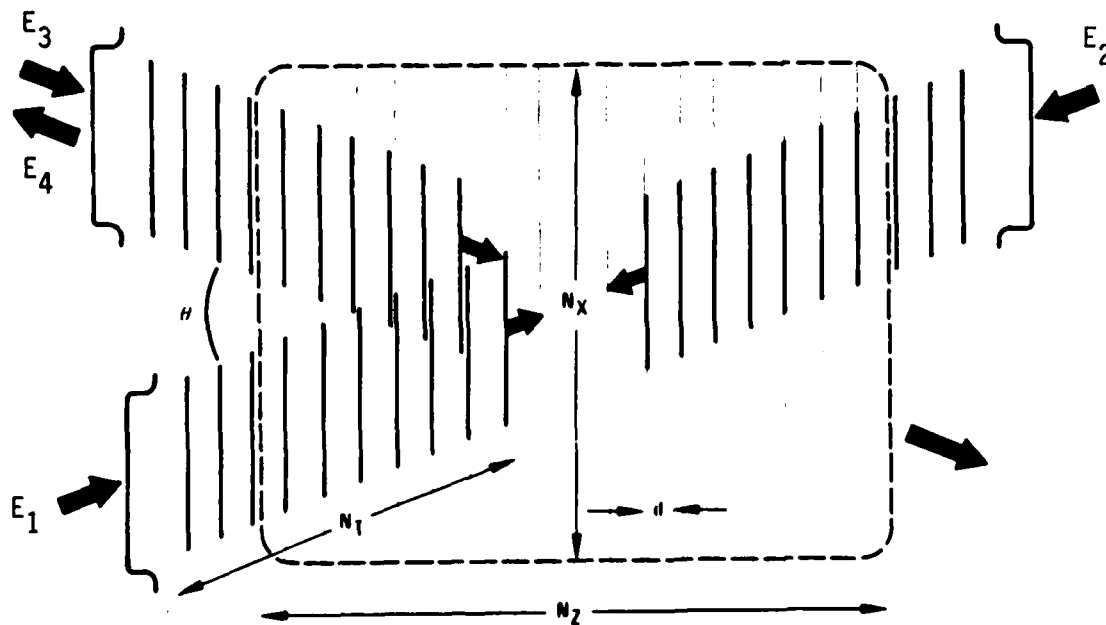

Figure 7-3. A two-dimensional schematic system of four wave mixing.

incidence angle of each beam can be input independently. The conjugate signal (beam 4) is expected to propagate on the same plane and in nearly the opposite direction of beam 3.

The region of the nonlinear medium extends from 0 to L in the z direction and has an aperture large enough to cover the four beams. At the beginning (t = 0), the pulse front advance of each beam into the medium can be adjusted to account for pulse delay in any of the beams. For longitudinal sampling the pulses are sliced into equally spaced sheets perpendicular to the z-axis. The slice distance is twice that of the propagation distance in each time step, so that the field on each sheet will interact with every field sheet in the oppositely directed pulse.

Transversely, the fields are sampled in equally spaced grid points across the whole aperture. The beam area is defined by either a Gaussian profile or an apodized (hypergaussian) square function. The apodized edges reduce the Fresnel ripple in propagating through the cell. Because the field sheets are not perpendicular to the actual direction of beam propagation for non-zero incidence angle, a linear phase variation is applied to the field across the beam. For pulse applications, such as those calculations performed for TRW's Free Electron Laser Resonator Development Program (FELRDP, Ref. 7-8), several different longitudinal pulse profiles can be used (Figure 7-4). These pulsed calculations are discussed here in order to illustrate the capabilities of the 2D code.

Before the pulses enter the interaction region, a phase screen representing the phase aberration can be applied to the complex field. The phase screen consists of up to five sinusoidally varying functions. With different variation amplitudes and periods, various phase screens can be created independently for each beam. The phase screen of beam 3 should be applied to the exiting beam 4 to check how well the aberration is corrected. In each case, the beam quality is calculated in terms of the Strehl ratio calculated from the rms phase variation.

The pulses advance in the medium using the near-field propagation scheme. In each propagation step, the one-dimensional field array is Fourier-transformed, multiplied by a transfer phase function and then inverse Fourier transformed. For CW cases, the propagation continues until a steady state is reached. For pulse interaction, the propagation stops when the rear end of every pulse leaves the medium completely. At the end of the run, the reflectivity and Strehl ratio are calculated. The

130
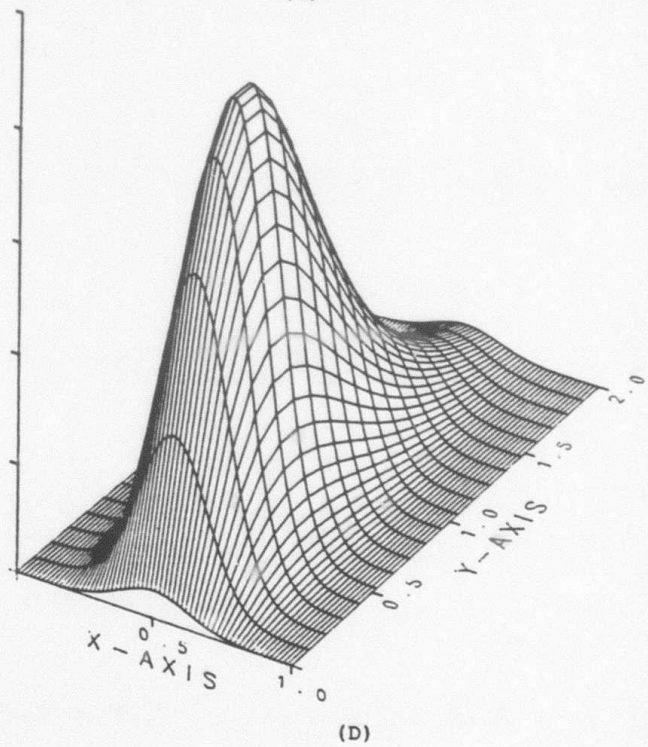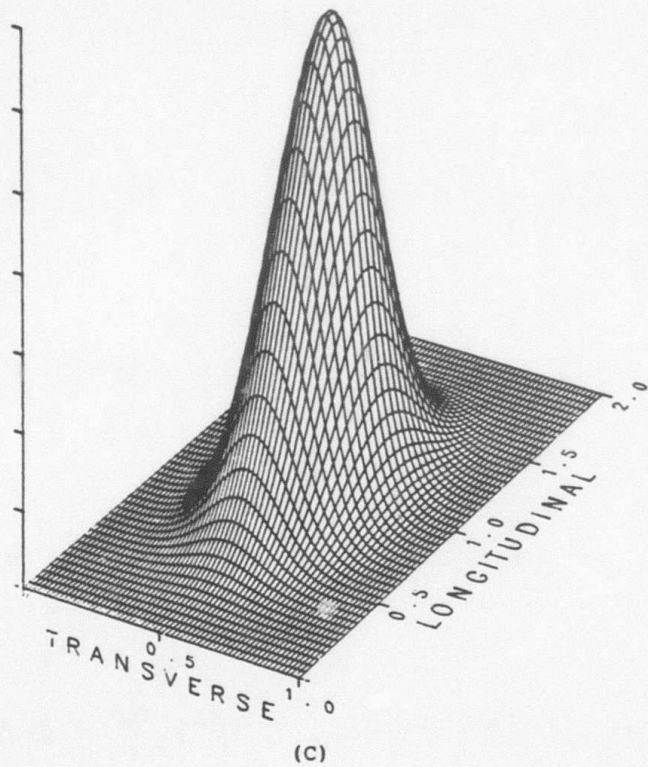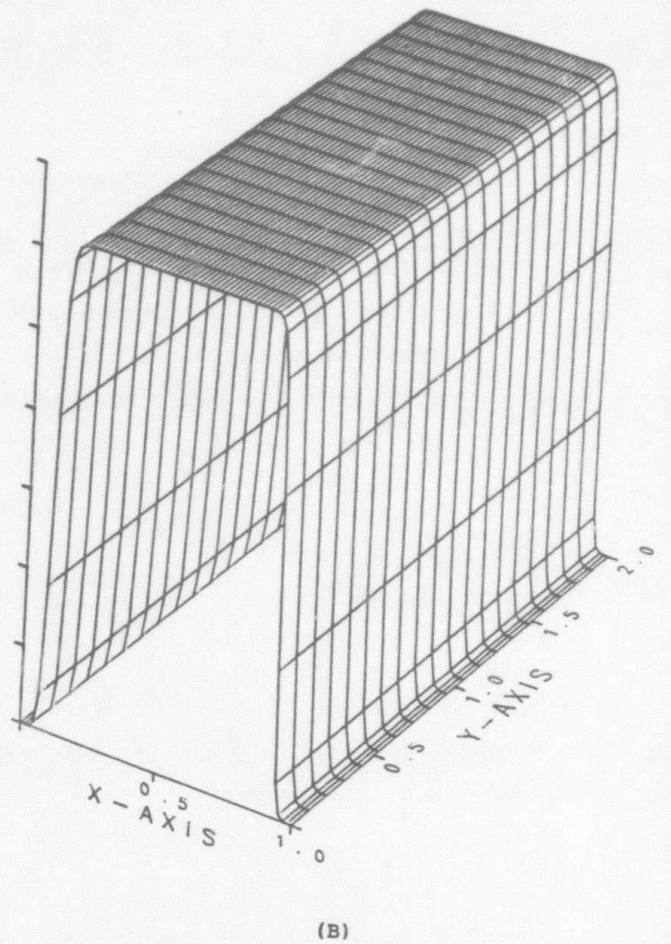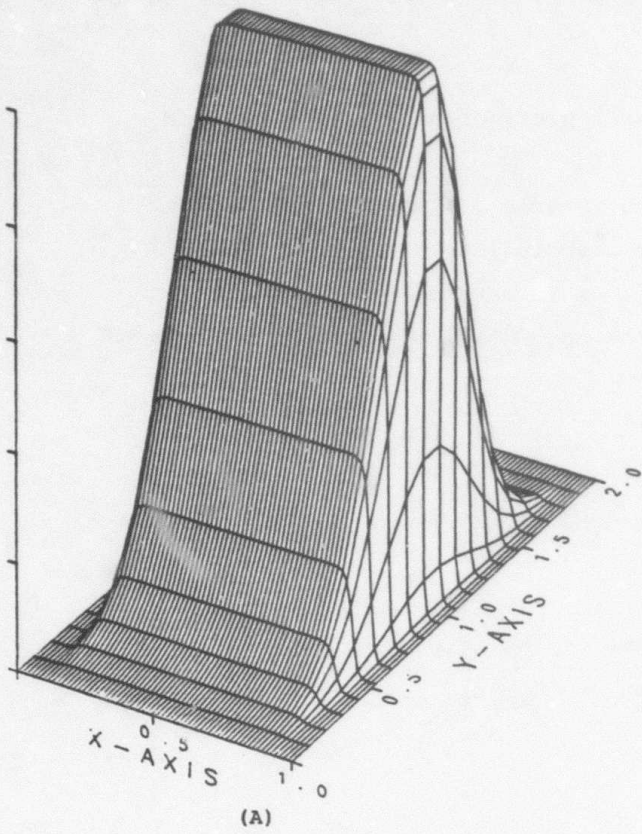
Figure 7-4.   Different pulse shapes acceptable to the two-dimensional code.

131

field arrays are stored for three-dimensional plots of pulse intensity and phase profiles.

In the nonlinear medium, every field interacts with itself and with each other through the nonlinear optical susceptibility. The code models such interaction in Kerr-like media as well as in saturable absorbing (or gain) materials. In a Kerr-like medium, the nonlinearity can be described by an effective index of refraction n:

$$n = n_0 + n_2 <E^2>. \qquad (7\text{-}1)$$

where $<E^2>$ is the time average of the square of the total field. Before each propagation, the complex field arrays, A_j (n_x, n_z), are updated according to the formula

$$\Delta A_j = -i \left[(2I_0 - I_j)A_j + 2A_k^* A_m A_n \right] \frac{2n_2 k_0 \Delta Z}{\cos\theta_j} \qquad (7\text{-}2)$$

where the indices are

j	k	m	n	(7-3)
1	2	3	4
2	1	3	4
3	4	1	2
4	3	1	2,

and

$$I_{jk} = |A_j|^2, \qquad (7\text{-}4)$$

132

$$I_o = I_1 + I_2 + I_3 + I_4 \qquad\qquad (7\text{-}5)$$

$$i = \sqrt{-1}$$

k_o is the vacuum wave number, θ_j is the incident angle of beam j and Δz is the propagation distance.

Equation 7-2 can also be tranformed from complex field amplitudes into coupled intensity and phase equations. Both methods are available in the code. Although using coupled intensity equations guarantees energy conservation, one has to be very careful in the region where the intensity is zero because the intensity variable appears in the denominator of the accompanying phase equations. In general, the first term in Equation 7-2 represents the self phase modulation which would result in self-focusing for a nonuniform beam. The second term represents the four wave interaction which would generate the conjugated return signal.

For the saturable absorbers, the model follows the equations given in Appendix A. Although the coupled equations were derived in the weak signal limit, we have added depletion terms in the equations for the pump beams. In this way, the pump depletion effect for the four wave mixing in saturable absorbers is qualitatively observed.

In practically all FWM experiments Gaussian laser beams are used, whereas most theoretical treatments of FWM assume that plane waves are employed. In these FWM experiments with Gaussian beams different results are often obtained than those predicted by the plane-wave FWM theories. These effects will be particularly important in saturable FWM media, where the magnitude of saturation will vary transversely across the Gaussian pump beams. The 2D FWM code is very useful in examining such effects. Using the 2D computer code, the following example calculations were performed. In the first calculation, the pump intensities are I/I°_{sat} = 2, the detuning is zero, the absorbance is three, and the spot size of all three input beams is 200 μm (radius of the 1/e point of the E-field). For these conditions the DFWM reflectivity is equal to 1.8%. In a second calculation where all the parameters are identical except the signal beam is made smaller with a spot size equal to 50 μm, the reflectivity decreases by ~25% to 1.4%. For plane waves, the DFWM reflectivity is independent of the signal beam spot size. The decrease in reflectivity observed when the signal beam spot size is made substantially

133

smaller than those of the pump beams is due to a reduced DFWM reflectivity in the highly saturated central position of the pump beams. The average I/I_{sat} is 4.3 times larger in the central 25% of the pump beams where the 50 μm signal beam overlaps, than it is in the outer 25% of the Gaussian pump beam. Thus, the probe beam with a spot size matched to those of the pump beams can sample regions of the pumped FWM medium which are not as severely saturated and can extract additional conjugate intensity from these regions.

Another consequence of the relative signal beam spot size compared to those of the pump beams can be seen in Figure 7-5 where the transverse intensity profile of the phase conjugate is plotted for the two cases just discussed. When the signal beam is much smaller than the pump beams (Figure 7-5A), the pump intensity varies little across the signal beam and the situation approximates that of plane-wave pump beams. In this case since the reflectivity is independent of the input signal intensity (no pump depletion), the signal conjugate is seen to be a Gaussian with the same spot size as the incident signal beam. In contrast, when the signal beam is identical in size to the pump beams, the phase conjugate transverse intensity profile is highly non-Gaussian (Figure 7-5B). The latter effect has been predicted theoretically (Ref. 7-9).

The particular Gaussian beam results discussed here apply only to the specific conditions listed above. When $I \ll I_{sat}$ or in regions where the change in reflectivity with pump intensity is relatively flat the variation in the signal spot size will not have an effect on the phase conjugate reflectivity. However, as TRW is primarily interested in phase conjugation in the high reflectivity regime, the Gaussian beam effects predicted here by the 2D model can have important consequences on the results of the FWM experiments.

The most advantageous property of a two-dimensional code over a one-dimensional code is its ability to demonstrate the fidelity of the phase conjugation process in the four wave mixing process. In the following example, calculated for FELRDP (Ref. 8), 2 mm long uniform pulses are used for all three input beams (Figure 7-6A). A phase screen prepared with five-term sinusoidal functions is applied to the signal beam before entering the medium. The aberrated beam is calculated to have a Strehl ratio of 0.77 (Figure 7-6B).

The intensity profile of the return pulse has a higher trailing end

134

(B)

Intensity (Arbitrary Units)

Transverse Beam Distance

(A)

Intensity (Arbitrary Units)
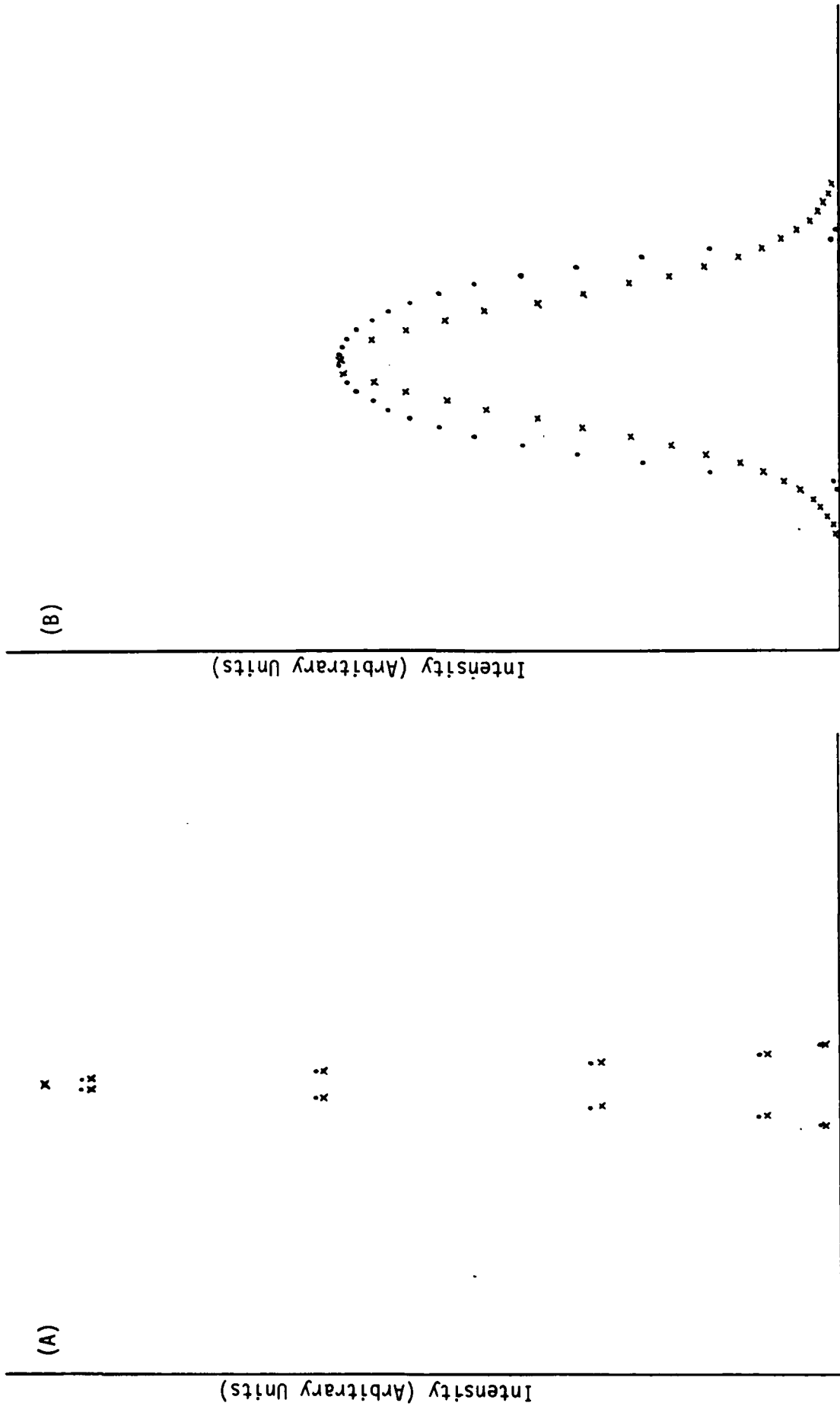
Transverse Beam Distance

Figure 7-5. (A) Probe beam is much smaller than the pump beams.
(B) Probe beam is same size as the pump beams.

• - 2D code points
x - Gaussian profile points

135
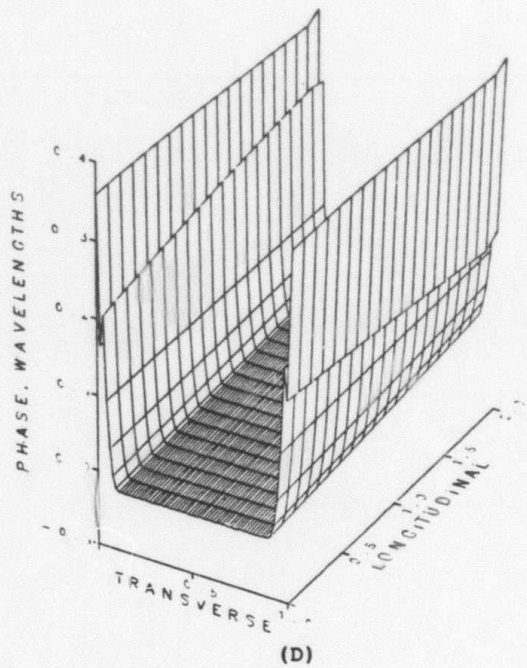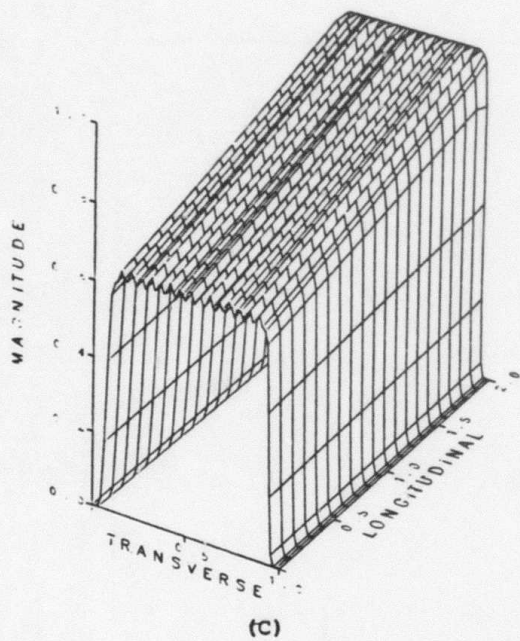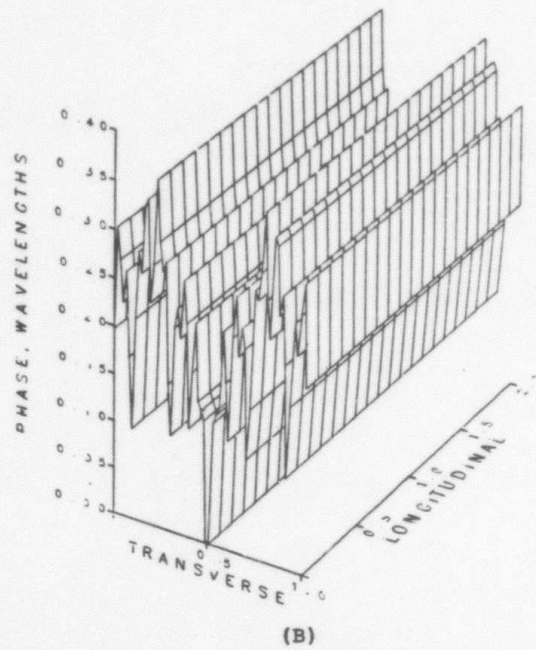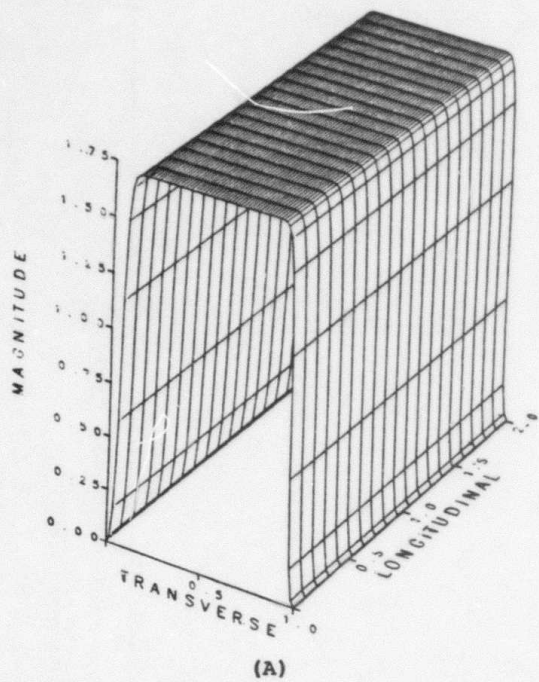
Figure 7-6. Demonstration of phase conjugation in four wave mixing.
(A) Input signal pulse profile, (B) Phase of aberrated
signal beam, (C) Return signal profile, (D) Corrected
phase distribution in the return signal.

(Figure 7-6C). This can be understood because the energy transfer
efficiency is proportional to the square root of the intensity product

$$\Delta I \sim (I_1 I_2 I_3 I_4)^{1/2}.$$

Since $(I_1 + I_3)$ and $(I_2 + I_4)$ are constants of the interaction,
the intensity product will be higher when I_3 and I_4 increase.
Therefore, the energy transfer is more efficient near the end of the
pulses. The ripples on the top of the intensity profile are due to the
applied phase screen.

The phase screen is applied to the conjugated return beam 4 after
exiting from the medium. The phase of the field becomes uniform in most
of the pulse area (Figure 7-6D). The phase increase near both sides of
the pulse is the result of wave propagation and is in a very low
intensity area. The correction of the beam aberration is nearly complete,
the Strehl ratio is calculated to be 0.997.

7.3 REFERENCES

7-1 R. L. Abrams and R. C. Lind, Opt. Lett. 2, 94 (1978); 3, 203 (1978).

7-2 W. P. Brown, J. Opt. Soc. Am. 73, 629 (1983).

7-3 M. T. Gruneisen, A. L. Gaeta, R. W. Boyd, J. Opt. Soc. Am. B 2,
1117 (1985); A. L. Gaeta, M. T. Gruneisen, R. W. Boyd, IEEE J.
Quantum Electron., QE-18. 1095 (1986).

7-4 The equations were integrated noniteratively using the IMSL Library
Fortran Subroutines DVERK and DGEAR.

7-5 In this case the IMSL Library subroutine DVCPR was employed.

7-6 A. L. Gaeta, personal communication.

7-7 A. Hardy and Y. Silberberg, J. Opt. Soc. Am. 73, 594 (1983).

7-8 Application of Nonlinear Optics to Free Electron Laser Systems, Final
Report, C. C. Shih, G. R. Neil, J. H. Menders, T. P. Yang, May 1986,
Contract No. N00014-84-C-0668, Free Electron Laser Resonator
Development Program.

7-9 G. Grynberg, B. Kleinmann, M. Pinand, Opt. Comm. 47, 291 (1983).

APPENDIX A. THEORY FOR DFWM CODES

The four-wave mixing system is shown in Figure A-1. The two pump beams are the forward ("f") and backward ("b") beams, which propagate along the z_0 direction. The signal beam ("s") and its conjugate ("c") are counterpropagating along the z' direction. The field equations use the z coordinate through the transformations $z_0 = z \cos(\theta/2)$ and $z' = z \cos(\theta/2)$.

Our starting point for the intensity and phase equations for each beam used in the code are the four coupled non-linear differential equations for each field derived in Boyd et al. (Ref. A-1). They start from the Maxwell equations satisfied by the total field as the source. (Polarization is solved as a steady state solution in the Bloch equation of the two-level system medium.) With the assumptions of a strong pump, weak signal, and the slowly-varying-envelope approximation for the field amplitude, they arrived at the following field equations:

$$\frac{\partial}{\partial z} \varepsilon_f = -\alpha_f \varepsilon_f \tag{A-1}$$

$$\frac{\partial}{\partial z} \varepsilon_b = +\alpha_b \varepsilon_b \tag{A-2}$$

$$\frac{\partial}{\partial z} \varepsilon_s = +\alpha \varepsilon_s - \kappa \varepsilon_c^* \tag{A-3}$$

$$\frac{\partial}{\partial z} \varepsilon_c = +\alpha \varepsilon_c + \kappa \varepsilon_s^* \tag{A-4}$$

where

$$\alpha_{f,b} = \overline{\alpha}_0 \left(1 + i\delta\omega T_2\right) \left[\frac{1}{C}\left(1 + \frac{C - B}{2I_{f,b}}\right)\right]$$

$$\alpha = \overline{\alpha}_0 \left(1 + i\delta\omega T_2\right) \left(B/C^3\right)$$

138

$$Z \cos (\theta/2) = Z_0$$
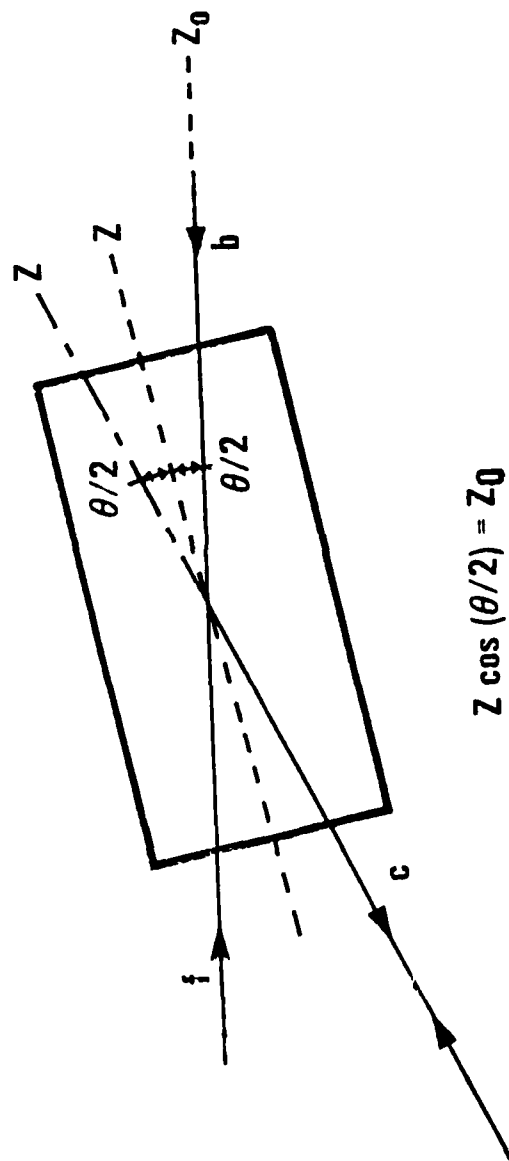
Figure A-1. Four-wave mixing system in the 2D code.

$$\kappa = \overline{2\alpha_0} \frac{(1 + i\delta\omega T_2)}{c^3} \frac{\epsilon_f \epsilon_b}{E_s^2}$$

with

$$\alpha_0 = \alpha_0/(1 + \delta\omega T_2) \equiv \alpha_0/(1 + \delta^2)$$

α_0 being the line-center field absorption coefficient, which becomes the gain coefficient if it is less than 0, and

$$I_{f,b} = \epsilon_{f,b}^{2}/E_s^{2}$$

$$B = 1 + I_b + I_f$$

$$C = \{B^2 - 4I_b I_f\}^{1/2}$$

$$= \{1 + (I_f + I_b) + (I_f - I_b)^2\}^{1/2}$$

where E_s is the medium saturation field amplitude.

From the equations A.1 through A.4, we have eight coupled equations of intensity and phase for all four beams. The intensities and phases are defined by:

$$\epsilon_{f,b} = \epsilon_{f,b} \, e^{(i\phi_{f,b})}$$

$$\epsilon_{s,c} = \epsilon_{s,c} \, e^{(i\phi_{s,c})}$$

$$I_{f,b} = \epsilon_{f,b}^{2}/E_S^{2} \equiv I_{f,b}^{0}/I_{sat}$$

$$I_{s,c} = \epsilon_{s,c}^{2}/E_S^{2} \equiv I_{s,c}^{0}/I_{sat}$$

where, for $\alpha = f, b$ or s, c,

$$I_\alpha^0 = \frac{cn}{6\pi} \, \epsilon_\alpha^{\,2}$$

and

$$I_{sat} = I_{sat}^0 \, (1 + \delta^2)$$

The eight coupled equations are:

$$\frac{d}{dz} I_f = -U_1 I_f + V \, (\cos\phi - \delta \sin\phi) \, \sqrt{I_f I_b I_s I_c} \tag{A-5}$$

$$\frac{d}{dz} \phi_f = -\frac{U_1}{2} \delta - \frac{V}{2} \, (\sin\phi + \delta \cos\phi) \, \sqrt{I_f I_b I_s I_c}/I_f \tag{A-6}$$

$$\frac{d}{dz} I_b = +U_2 I_b - V \, (\cos\phi - \delta\sin\phi) \, \sqrt{I_f I_b I_s I_c} \tag{A-7}$$

$$\frac{d}{dz} \phi_b = \frac{U_2}{2} \delta + \frac{V}{2} \, (\sin\phi + \delta\cos\phi) \, \sqrt{I_f I_b I_s I_c}/I_b \tag{A-8}$$

$$\frac{d}{dz} I_s = -U_3 I_s + V \, (\cos\phi + \delta\sin\phi) \, \sqrt{I_f I_b I_s I_c} \tag{A-9}$$

$$\frac{d}{dz} \phi_s = -\frac{U_3}{2} \delta - \frac{V}{2} \, (\sin\phi - \delta\cos\phi) \, \sqrt{I_f I_b I_s I_c}/I_s \tag{A-10}$$

$$\frac{d}{dz} I_c = U_4 I_b - V \, (\cos\phi + \delta\sin\phi) \, \sqrt{I_f I_b I_s I_c} \tag{A-11}$$

$$\frac{d}{dz} \phi_c = \frac{U_4}{2} \delta + \frac{1}{2} V \, (\sin\phi - \delta\cos\phi) \, \sqrt{I_f I_b I_s I_c}/I_c \tag{A-12}$$

where

$$U_1 = 2\overline{\alpha}_0 \frac{1}{C} \left(1 - \frac{C - B}{I_f}\right)$$

$$U_2 = 2\overline{\alpha}_0 \frac{1}{C} \left(1 - \frac{C - B}{I_b}\right)$$

$$V = 4\overline{\alpha}_0/C^3$$

$$\phi = \phi_s + \phi_c - \phi_f - \phi_b$$

$$U = 2\overline{\alpha}_0 B/C^3 = U_4$$

with

$$\overline{\alpha}_0, \delta, B, \text{ and } C \text{ defined above.}$$

Equations A-5 through A-12 are truely equivalent to A-1 through A-4 if one omits the underlined terms in equations A-5 through A-8. These terms are added rather than derived from the field equations. This is an approximate way to account for the pump depletion following the derivation of similar equation for Kerr-like media by Hardy and Silberberg. (Ref. A-2).

For application to two-level systems, inputs needed are resonant wave length, pump laser wave length, line center field absorption (gain) coefficient α_0 (g_0), gain medium saturation intensity I_{sat}, and normalized detuning parameter δ. At resonance $\delta = 0$, hence our results are not affected by a change of sign in δ. This code also applies to Kerr-like media if one inputs the susceptibility.

Since the derivation is based on the assumption of a weak signal, a more rigorous treatment is needed for exploring the strong signal regime.

Appendix A References

A-1   M.T. Gruneisen, A. L Gaeta, R. W. Boyd, J. Opt. Soc. Am. B $\underline{2}$, 1117
       (1985); A. L. Gaeta, M. T. Gruneisen, R. W. Boyd, IEEE J. Quantum
       Electron., $\underline{QE-18}$, 1095 (1986).

A-2   A. Hardy and Y. Silberberg, J. Opt. Soc. Am. $\underline{73}$, 594 (1983).